IN-43
189105
P-75

NASA Contractor Report 189728

Investigation of Antenna Pattern Constraints for Passive Geosynchronous Microwave Imaging Radiometers

A. J. Gasiewski and G. M. Skofronick
Georgia Institute of Technology
Atlanta, Georgia

Research Triangle Institute
Research Triangle Park, North Carolina

Contract NAS1-18925
December 1992

National Aeronautics and
Space Administration

Langley Research Center
Hampton, Virginia 23665-5225

TABLE OF CONTENTS

SUMMARY OF ACTIVITIES

During the period of this grant, the authors succeeded in implementing four out of the required six components necessary to define the spatial resolution requirements of candidate spaceborne microwave imaging systems. A brief discussion of these components follows; more complete discussions are contained in the conference publication in Appendix A and the draft technical publication in Appendix B. It is noted that precipitation measurements (e.g., surface rain rates and water density and phase profiles) place the most severe demands of any geophysical observable on the spatial resolution, accuracy, and spectral coverage of a microwave imaging system [Stutzman and Brown, 1991]. Thus, we have targeted accurate and timely precipitation measurements as constituting the driving requirements of such sensors. Our choice of maritime (as opposed to continental) precipitation is based on the greater utility of a spaceborne precipitation measurement system in observing the Earth over relatively inaccessible oceanic regions rather than land.

(1) Spatial microphysical cloud and rain data. In order to derive realistic assessments of the performance of candidate sensors, statistically meaningful cloud and raincell data has been obtained. Three sources of data are used: (A) Simulated three-dimensional microphysical data from the Goddard Cumulus Ensemble model [Tao and Simpson, 1889]. This consists of five frames sampled throughout the lifetime of a convective squall. The prevailing conditions are based on observed data from the Global Atmospheric Research Program's Atlantic Tropical Experiment (GATE). (B) A volume weather radar scan of an isolated multicell system observed during the Cooperative Huntsville Meteorological Experiment (COHMEX, 1986) [Gasiewski, 1989]. (C) Synthetic cloud and raincell data based upon published spatial and temporal statistics of rainfall.

(2) Forward radiative transfer model. Brightness maps for the above data at virtually all microwave channels considered to be useful for tropospheric precipitation sensing have been computed using the iterative

radiative transfer model described by Gasiewski and Staelin [1990]. These maps constitute a set of "full resolution" images from which particular channels subsets can be selected to study the performance of a candidate sensor. The channels under consideration are at microwave window frequencies from 6 to 410 GHz (9 channels), near the 22.235-, 183.31-, and 325.15-GHz water vapor lines (10 channels), within the 5-mm oxygen band (5 channels), and near the 118-GHz oxygen line (6 channels).

(3) Antenna gain pattern convolutions. Spot patterns for diffraction limited circular apertures are generated to provide the multispectral point spread function that would be expected from a candidate sensor. Each channel is assumed to be diffraction limited, so that the multispectral spot pattern exhibits successively decreasing 3-dB spot sizes as frequency increases. Currently, the degree of aperture illumination taper is selectable so that the effects of varying aperture efficiency and taper on the resulting retrieval accuracy can be studied. The candidate systems used in the simulations are the three systems referred to in Appendix B: the EOS-B MIMR LEO system with 1.6- and 4.4-m apertures, and the Large Space Antenna (LSA) nine-channel (6-410 GHz) and eight-channel (18-55 GHz) GEO systems with 15- and 40-m apertures. The submillimeter wave channels in the nine-channel LSA GEO system could potentially provide adequate spatial resolution for raincell mapping using only moderately-sized apertures [Gasiewski, 1992].

The multispectral spot patterns for a candidate sensor are convolved with the full resolution imagery to obtain the antenna temperature imagery. This imagery is subsequently sampled at the Nyquist resolution, effectively simulating the antenna scan process. After convolution, an appropriate pseudorandom instrument error map is added to simulate radiometric noise in the detected signal. The noise level is determined from the spot dwell time, the receiver noise temperature, and the channel bandwidth. Since these quantities can vary considerably among candidate designs, a representative set of receiver characteristics consistent with the proposed EOS MIMR low-Earth orbiting system and the LaRC Large Space Antenna (LSA) geosynchronous system was chosen.

(4) Karhunen-Loeve image SNR analyses. The Karhunen-Loeve (KL) transform was used to estimate the number of observable spectral degrees of freedom in the noisy, convolved (received) imagery. Upon prewhitening the received imagery (so as to intercompare channels on a noise-equivalent basis), the KL transform was computed. The eigenvalues of the KL transform are the signal-to-noise ratios (SNR's) of the uncorrelated spectral modes of the imagery. Compared to the full-resolution case, the MIMR imagery exhibits reductions of 1 to 3 dB in the SNR's of the second- and third-most dominant modes for 4.4-m and 1.6-m diameter apertures. Reductions in SNR for second- and third-most dominant modes in the LSA 40-m and 15-m systems are larger (up to 10 dB or more). The dominant modes in these systems exhibit no significant SNR reductions from the full resolution case to either of the respective smaller apertures.

However, the interpretation of the KL modes and the associated SNR's for various spatial resolutions cannot be considered to be complete until these mode are incorporated into the precipitation parameter retrieval algorithms, discussed in component 6.

(5) Multispectral deconvolution studies. Although not yet implemented, the intermediate step of multispectral deconvolution is expected to simplify the resulting precipitation retrievals by reconstituting the multispectral brightness image to the best degree possible. In the deconvolution, there will inevitably be a tradeoff between the resulting spatial resolution and noise in the deconvolved imagery. It is the manifestation of this tradeoff on area-averaged precipitation retrieval error which is of prime interest. The imagery from components 2-3 will be useful here in determining optimum deconvolution filters based on the spatial and spectral statistics of the underlying full-resolution imagery.

(6) Area-averaged rain rate retrieval error analyses. This final and most important component of the simulation will (upon complete implementation) produce surface rain rate, freezing altitude and water density and phase profile estimates based on the received, deconvolved imagery.

Two nonlinear statistical schemes, both optimal in their use of the

received data, are currently being implemented: (A) the single-step nonlinear-statistical retrieval method, which uses KL rank reduction to reduce the number of input channels prior to estimating surface rain rate and water density, and (B) the iterative statistical method, which uses the forward radiative transfer relationships to determine successive linear statistical corrections to the retrieved parameters. Both of these methods have been previously documented [Gasiewski and Staelin, 1989; Kuo, 1990].

CONCLUSIONS AND PLANS FOR FUTURE WORK

Conclusions from the first four of the six components of the simulation study, including examples of full resolution, convolved, and Karhunen-Loeve imagery are contained primarily in the report, "Simulations of the Effects of Spatial Resolution on Passive Microwave Remote Sensing of Precipitation'', in Appendix B. Although the quantitative effects of aperture size, main beam efficiency, channel selection, and antenna gain perturbations on simulated precipitation retrieval accuracy cannot yet be given[1], several observations concerning effects on the received imagery and associated KL imagery can be made.

An important feature is that the KL eigenvectors are relatively independent of storm type, nor do they depend critically on the stage of the raincell. In addition, the eigenvectors change only marginally as the aperture diameter (i.e., system resolution) changes. These observations suggest that the dominant modes of spectral variation in microwave precipitation imagery are effectively unique for a given set of microwave channels. However, as spatial resolution is lost, the eigenvectors increasingly emphasize the higher frequency channels.

The convolved imagery and KL mode signal-to-noise (SNR) analysis unambiguously show a loss in spectral variance as aperture size is reduced. For the apertures considered, the size reductions usually reduce the SNR in the dominant mode by only one or two dB, but reduce the higher order modes by much more (up to 10 dB). The number of degrees of freedom in the multispectral precipitation imagery varies for the different systems analyzed, but is approximately three to five. Although the effect that the KL modes have on the accuracy of precipitation parameter retrieval is still to be quantified, the loss of information as aperture size is reduced is discernible.

In microwave radiometry, antenna main beam efficiencies of at 90-95% are considered to be required if deconvolution is not used. Note that this

---

[1] Future work on the problem of passive multispectral microwave imaging will continue beyond the end of this grant under NASA Graduate Student Research Program (GSRP) grant NGT-50903.

is the null-to-null efficiency, as 3-dB efficiencies greater than 50-55% cannot practically be achieved. Such main beam efficiencies will require tapered aperture illuminations, as uniform tapers cannot yield main beam efficiencies greater than 86%. However, tapering necessarily reducing the system resolution. If the gain pattern is known precisely enough, some deconvolution can be performed. By modelling the effects of antenna gain uncertainty as additional receiver noise (as shown in Appendix B, section 4), the tradeoffs between the gain uncertainty, calibration uncertainty and illumination taper can be studied.

Some comments must be made about the spatial sampling rate of microwave imagers. While it is commonly thought that sampling in spatial increments equal to the 3-dB footprint of the antenna is adequate for passive microwave imaging, this is, in fact, at least two to four times larger than the Nyquist sampling increment. Thus, there is no guarantee against aliasing in any system that samples at the "3-dB" rate. Of course, Nyquist sampling requires significantly higher data rates and potentially higher mechanical slew rates than 3-dB sampling. One of the tradeoffs to be studied using the PMMRS will be the consequences of aliasing in sub-Nyquist sampled imaging systems.

Future simulation studies will utilize the KL modes in nonlinear precipitation parameter retrieval methods. The first method, currently being developed, will use a nonlinear single-step estimator which correlates the KL modes with rain rate. Subsequently, an iterative scheme using a linear statistical operator at each step will be investigated as a means of improving the performance of the single step nonlinear operator. The retrieval operators will incorporate spectral-domain multispectral deconvolution operators [Rosenkranz, 1978] to improve the resolution of the brightness maps prior to inversion for the following parameters: surface rain rate, water density at five levels, mean ice particle size, and altitude of nucleation. The analyses will attempt to address 1.6-m and 4.4-m GEO systems as well as the three systems addressed in Appendix B. Additional three dimensional raincell microphysical data will be included as available.

REFERENCES

Stutzman, W.L., and G.S. Brown (eds.), "The Science Benefits of and the Antenna Requirements for Microwave Remote Sensing from Geostationary Orbit", NASA Contractor Report 4408, Prepared by the Virginia Polytechnic and State University, Blacksburg, VA for the NASA Langley Research Center, 1991.

Tao, W.K., and J. Simpson, "Modelling Study of a Tropical Squall-Type Convective Line", J. Atm. Sci., vol. 46, no. 2, pp. 177-202, Jan. 15, 1989.

Gasiewski, A.J., and D.H. Staelin, "Statistical Precipitation Cell Parameter Estimation Using Passive 118-GHz O_2 Observations", J. Geophys. Res., vol. 94, no. D15, pp. 18367-18378, December, 1989.

Gasiewski, A.J., and D.H. Staelin, "Numerical Modelling of Passive Microwave O_2 Observations Over Precipitation", Radio Sci., vol. 25, no. 3, pp. 217-235, 1990.

Gasiewski, A.J., "Numerical Sensitivity Analysis of Passive EHF and SMMW Channels to Tropospheric Water Vapor, Clouds and Precipitation", Accepted for publication in IEEE Trans. Geosci. Remote Sensing, May, 1992.

Rosenkranz, P.W., "Inversion of Data from Diffraction-Limited Multiwavelength Remote Sensors, 1, Linear Case," Radio Science, vol. 13, no. 6, pp. 1003-1010, Nov.-Dec., 1978.

Kuo, C.C., "Statistical Iterative Scheme for Estimating Atmospheric Relative Humidity Profiles from Microwave Radiometric Measurements", S.M. thesis, Department of Electrical Engineering and Computer Science, Massachusetts Institute of Technology, Cambridge, MA., Dec., 1988.

PASSIVE MICROWAVE PRECIPITATION MAPPING AND RETRIEVAL SIMULATION

G. M. Skofronick and A.J. Gasiewski

School of Electrical Engineering
Georgia Institute of Technology
Atlanta, GA 30332-0250

Abstract-A numerical simulation of the satellite-based multispectral passive microwave mapping and precipitation retrieval process is described. The simulation contains three major components: (1) the forward radiative transfer calculation, (2) the sensor observation simulation, and (3) the precipitation retrieval algorithm. Secondary components include a Karhunen-Loève transformation module and antenna pattern deconvolution module. The simulation facilitates the investigation of candidate precipitation retrieval algorithms using sub-Nyquist brightness temperature imagery and the comparison of the relative merits of proposed radiometric systems such as the EOS Multispectral Imaging Microwave Radiometer (MIMR), the TRMM Microwave Imager (TRMM TMI), and future geosynchronous satellite sensors. A procedure for retrieving rain rates using a statistical iterative approach is outlined.

1. Introduction

In satellite-based passive remote sensing, both microwave and infrared frequencies are commonly used to observe properties of atmospheric hydrometeors. An important feature of infrared imagery is the available high spatial resolution. However, due to the large extinction at infrared wavelengths, such sensors are unable to probe through most cloud cover. Relative to infrared sensing observations, multifrequency microwave sensing provides a valuable complementary capability in being able to probe through clouds. This is possible to a degree which depends on the particular frequency of observation and the hydrometeor density and size distribution. For example, frequencies below $\sim$ 6 GHz respond significantly to only very strong precipitation, while frequencies above $\sim$ 220 GHz respond to even light non-precipitating clouds such as cirrus.

The relative simplicity of the forward transfer relationship at microwave frequencies along with the wide available range of optical depths suggests that profiling of various precipitation parameters (e.g. rain rate and hydrometeor density, size, and phase) might be possible. However, the non-linear relationship between area-averaged precipitation parameters and the observed brightness temperatures is a major cause of error in retrieving these parameters. Impediments to improving retrieval accuracy include: (1) sub-Nyquist spatial sampling caused by wide antenna beamwidths, (2) radiometric instrument noise, and (3) antenna calibration and gain pattern uncertainty. Since the technological costs for overcoming these impediments are high, it is of vital importance to determine the available performance of candidate spaceborne sensor systems for cost/benefit tradeoff purposes.

To assess the relative merits of various passive microwave precipitation measurement systems, numerical simulations of the observation and retrieval process are being performed. A goal of these simulations is to develop precipitation parameter retrieval algorithms optimized for the channel, noise and gain pattern characteristics of individual sensors. Existing systems being studied include the DMSP Special Sensor Microwave/Imager (SSM/I) and the Special Sensor Microwave/Temperature Sounder (SSM/T-2); proposed sensors being investigated include the MIMR and the TRMM TMI.

The simulation software, called the Passive Microwave Mapping and Retrieval Simulator (PMMRS), provides a flexible end-to-end simulation of a multispectral passive microwave imaging and retrieval system. The PMMRS models three primary processes: the forward radiative transfer process, the observation process, and the precipitation retrieval process. As shown in Figure 1, the forward radiative transfer process converts microphysical cloud data into upwelling brightness imagery, the observation process transforms the upwelling brightness imagery into the brightness temperatures recorded by the antenna sensor, while the retrieval process estimates atmospheric parameters (e.g., rain rate) and compares them to parameters derived from the original microphysical cloud data. The PMMRS permits evaluating retrievals for user-selected combinations of sensor antenna specifications, channel sets, noise levels, observation geometry, and precipitation classes.

2. Forward Radiative Transfer Simulation

Microphysical cloud parameter data used in this investigation is composed primarily of 3-dimensional synthesized data from the Goddard Cumulus Ensemble (GCE) simulation of a developing convective storm system [1]. This data consists of a set of five time samples of a tropical squall developed from initial conditions measured during GATE. Vertical profiles of pressure, temperature, relative humidity, liquid hydrometeor content and frozen hydrometeor content are given for each pixel. Horizontal spatial resolution is 1.5 km. Vertical resolution is typically 1 km. Additional microphysical data based on a volume scan of a convective multicell system made by the CP-2 weather radar during the Cooperative Huntsville Meteorological Experiment (COHMEX, 1986) is used.

The microphysical cloud data were mapped into upwelling brightness images (T_B) using the iterative forward radiative transfer model developed by Gasiewski and Staelin [2]. This is a planar-stratified scattering-based calculation that uses the specified surface reflectivity and atmospheric parameters (temperature, pressure, relative humidity, hydrometeor distributions, etc.) at levels from the surface to $\sim$ 25 km. Brightness temperature imagery over a calm ocean was computed for the following microwave channels: 6, 10.69, 18.7, 23.8, 36.5, 50.3, 52.8, 53.596, 54.4, 54.94, 89, 118.75 $\pm$(0.0, 0.12, 0.22, 0.37, 0.67, 1.27, 2.07), 166, 183.31 $\pm$(0.0, 1.0, 3.0, 7.0), 220, 325.153 $\pm$(0.0, 1.0, 3.0, 7.0, 9.0), 340, and 410 GHz. For example, Fig. 2a shows the full-resolution brightness temperature imagery for three of the six MIMR channels. The bimodal structure seen in the imagery of the 18.7 GHz channel is caused by cold oceanic reflectance outside the storm, a warming caused by thin absorbing clouds near

the periphery of the storm, and a cooling due to ice scattering at the center of the storm system.

3. Sensor Observation Simulation

To simulate the observation process, four operations are performed: (1) an antenna gain pattern is calculated, (2) the upwelling brightness temperatures are convolved with the antenna gain, (3) the convolved imagery is sampled, and (4) pseudo-random instrument noise is added. A Bessel approximation is used in generating gain patterns for circular parabolic aperture antennas. The gain pattern generator requires the following user-supplied parameters: aperture diameter, illumination taper, frequency, and number of sidelobes to include in the gain pattern. The spatial response for each channel follows from the orbital parameters (e.g., satellite altitude). A two-dimensional convolution of the calculated brightness imagery and the spatial response yields the antenna temperature imagery:

$$\overline{T}_A(x,y) = \overline{g}(x,y) ** \overline{T}_B(x,y) + \overline{n}(x,y) \qquad (1)$$

which is a blurred version of the underlying brightness imagery. The computed antenna temperature image for each channel is downsampled according to the instrument's highest effective spatial resolution. Gaussian pseudo-random noise is added to each pixel to simulate instrument observation error. The noise standard deviation is determined for each channel based on the available bandwidth at that frequency, integration interval, and expected system noise temperature. Figure 2b shows three channels of the MIMR imagery convolved with the sensitivity pattern of a circular 1.6-m linearly-tapered aperture at an orbital altitude of 705 km. The 89-GHz channel has a 3-dB spot size of $\sim$ 1.9 km, and reveals most of the storm structure. At 6-GHz, the spot size is $\sim$ 28 km, and nearly all storm structure is lost.

4. Karhunen-Loève Analysis

The original T_B and the convolved T_A imagery is analyzed for loss in observational degrees of freedom using a Karhunen-Loève (KL) transformation (also called principal component analysis). The unitary KL transform is used to rank-order the dominant spectral modes in the T_B and T_A imagery by the mode signal-to-noise ratio (SNR) [3]. The modes are determined by the eigenvectors of the spectral covariance matrix. The eigenvectors provide a measure of the contribution from each channel to the transformed image. Associated with each eigenvector is an eigenvalue which is the variance for the particular KL mode. To account for observational noise variations among the channels, prewhitening the brightness imagery prior to computation of the covariance matrix is performed.

The two most dominant KL images (i.e., those with the two largest SNR's) for the six channel full-resolution MIMR imagery are shown in Fig. 3. The adjoining eigenvector plots reveal that the most dominant mode is essentially the spectral difference between the 23.8- and 89-GHz channels. We interpret this as the strong scattering signature from ice aloft. The second KL mode is a combination of the scattering signature from the high frequency channels and the spectral difference between the 6- and 10.69-GHz channels, and appears to be sensitive to the radiometrically-thin periphery of the storm. The KL-mode SNR's for the full-resolution and convolved MIMR imagery (Fig. 4) can be used to determine the loss in number of observable degrees of freedom caused by the antenna pattern's broadness. If we arbitrarily assume that a KL mode contains useful information only if it has a SNR$\geq$2.0=3dB, the number of observable degrees of freedom decreases from approximately three to two upon convolution of the MIMR antenna pattern.

5. Precipitation Retrieval Simulation

This component of the PMMRS provides an environment for developing and optimizing precipitation retrieval algorithms for multispectral sub-Nyquist sampled microwave imagery. To take advantage of the spatial resolution available from high-frequency channels, multispectral deconvolution of the antenna gain pattern is first performed. Two deconvolution modules are being developed. Both methods use information from the highest resolution (i.e., highest frequency) channels to improve the resolution of the lower frequency channels. The first method uses the well-known Linear Minimum Mean Squared Error (LMMSE) approach in the spatial domain, such that:

$$\hat{\overline{T}}_B = \overline{D}\,\overline{T}_A \qquad (2)$$

where $\overline{T}_A$ is a vector consisting of all pixels from all channels having any significant correlations with the brightness at the location of interest. Such correlations can be due to either rain cell structure, spectral scattering or absorption structure, or antenna pattern filtering. The determination matrix $\overline{D}$ is given by:

$$\overline{D} = \overline{R}_{T_B T_A}(\overline{R}_{T_A T_A} + \overline{R}_{nn})^{-1} \qquad (3)$$

$\overline{R}_{ij}$ is the joint spatial-spectral covariance matrix between the multispectral 2-dimensional signals i and j.

The second deconvolution method, developed by Rosenkranz [4], uses a determination matrix $\overline{D}(u,v)$ in the spatial Fourier domain, and thus assumes stationarity in the statistics of the underlying brightness imagery. In this method $\hat{\overline{T}}_B$ is found from:

$$\mathcal{F}\{\hat{\overline{T}}_B(x,y)\} = \overline{D}(u,v)\mathcal{F}\{\overline{T}_A(x,y)\} \qquad (4)$$

where $\mathcal{F}$ is the 2-dimensional Fourier transform and u, v are spatial frequencies. The expression for $\overline{D}(u,v)$ can be found in [4]. To obtain $\hat{\overline{T}}_B$, the inverse Fourier transform is used.

Subsequent to deconvolution, rain rate retrieval algorithms are to be implemented. Parameter estimation techniques under consideration include LMMSE algorithms, Wiener filtering, and non-linear statistical and iterative estimators. For optimum retrievals, the non-linear relationship between brightness temperatures and cloud and precipitation parameters must be considered. Here, a statistical iterative retrieval technique based on the piecewise-linear relationship between incremental changes in brightness temperature and incremental changes in surface precipitation rate (via the absorption and scattering coefficients) is of interest. This technique is similar to the LMMSE technique except that $\overline{D}$ becomes an incremental predictor matrix, $\overline{\mathcal{D}}$, and ΔT_B and ΔR (where ΔR is the incremental change in rain rate) replace $\overline{T}_A$ and $\hat{\overline{T}}_B$, respectively, in Eqs. 2, 3, and 4. The statistical iterative technique has been proved useful in retrieving relative humidity profiles [5].

6. Discussion

At this time both the forward radiative transfer and the sensor observation components of the PMMRS have been implemented. In addition, a study of the number of observable degrees of freedom for sensors systems with different antenna aperture diameters and observation geometries has been performed. Some results from this study are in Table 1. Although we cannot yet quantify the available retrieval accuracy of candidate systems, the loss in number of observable degrees of freedom as aperture size is reduced is readily seen. Future implementation of the deconvolution and parameter retrieval components of the PMMRS will improve our ability to determine (quantitatively) the available accuracy of existing and future spaceborne passive microwave meteorological systems and to design optimized sensor-specific multispectral retrieval algorithms.

Acknowledgements-This work has been supported by the Georgia Institute of Technology and NASA grant NAS1-18925. The authors also thank N. Prasad of the NASA Goddard Space Flight Center for providing the Tao and Simpson GCE data.

References

[1] W.-K. Tao, and J. Simpson, "Modeling Study of a Tropical Squall-Type Convective Line," *J. Atm. Sci.*, Vol. 46, No. 2, Jan. 15, 1989.

[2] A.J. Gasiewski, and D.H. Staelin, "Numerical Modeling of Passive Microwave O_2 Observations over Precipitation," *Radio Science*, Vol. 25, No. 3, pp. 217-235, May-June 1990.

[3] P.J. Ready and P. A. Wintz, "Information Extraction, SNR Improvement, and Data Compression in Multispectral Imagery," *IEEE Trans. on Comm.*, Vol. COM-21, No. 10, pp. 1123-1130, Oct. 1973.

[4] P.W. Rosenkranz, "Inversion of Data from Diffraction-Limited Multiwavelength Remote Sensors, 1, Linear Case," *Radio Science*, Vol. 13, No. 6, pp. 1003-1010, Nov.-Dec. 1978.

[5] C.C. Kuo, "Statistical Iterative Scheme for Estimating Atmospheric Relative Humidity Profiles from Microwave Radiometric Measurements," M.S. thesis, Department of Electrical Engineering and Computer Science, Massachusetts Institute of Technology, Cambridge, MA., December 1988.

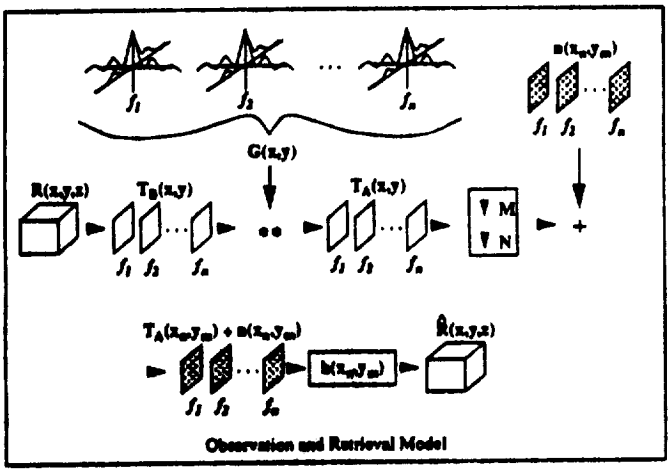

Figure 1: Schematic diagram of the PMMRS.

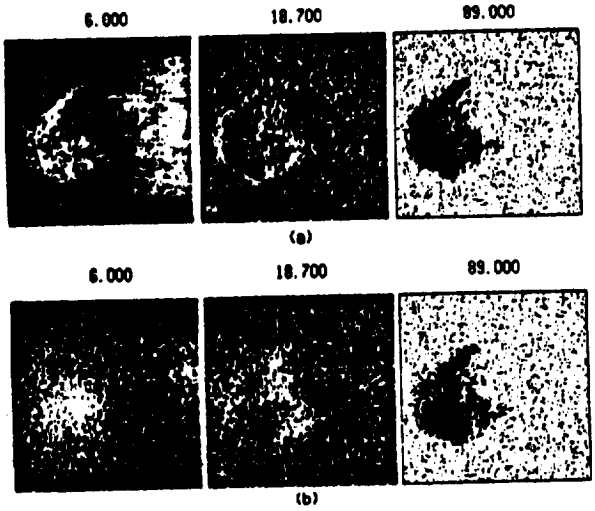

Figure 2: Representative MIMR brightness temperature imagery for 6, 18.7, and 89-GHz: (a) full resolution, and (b) after convolution with the gain pattern of a circular 1.6-m linearly-tapered aperture. The respective 3-dB spot sizes are 28, 9 and 1.9 km.

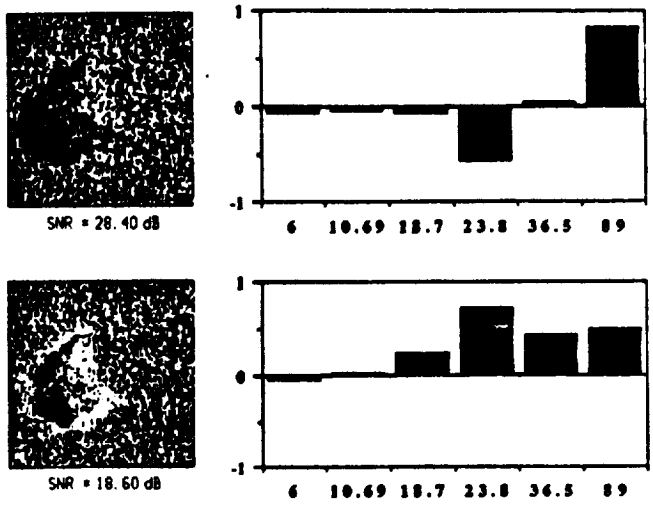

Figure 3: The two most dominant Karhunen-Loève modes for the full-resolution imagery in Fig. 2a, along with the associated eigenvectors.

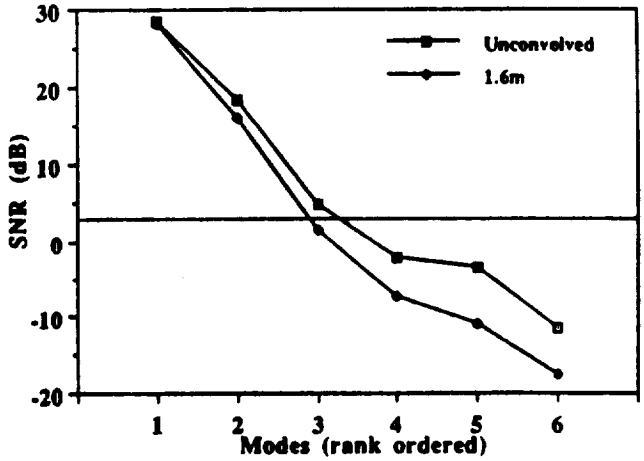

Figure 4: SNR ranking for full-resolution and convolved MIMR imagery.

Table 1: Number of Observable Degrees of Freedom

Sensor	Aperture diameter (m)	# channels	# degrees of freedom
Geosynchronous	∞	9	7
	30	9	4
MIMR	∞	6	3
	1.6	6	2

Notes:
(1) Assumes circular linearly-tapered aperture field.
(2) $D = \infty$ implies full resolution imagery.
(3) Degrees of freedom observable only if SNR≥2.0=3dB.

Proceedings of the 1992 IEEE International Geoscience and
Remote Sensing (IGARSS) Symposium

Simulation of the Effects of Spatial Resolution on Passive Microwave Remote Sensing of Precipitation

A.J. Gasiewski and G.M. Skofronick

School of Electrical Engineering
Georgia Institute of Technology
Atlanta, Georgia 30332-0250

Final Report to the
NASA Langley Research Center
for
NASA contract NAS1-18925
July 15, 1992

Abstract-A numerical simulation of the satellite-based multispectral passive microwave precipitation mapping and retrieval problem is described. The purpose of this simulation is to provide antenna and radiometer systems engineers with quantitative performance predictions for proposed spaceborne passive microwave imaging sensors. The simulation contains six major components: (1) microphysical cloud and raincell data compilation, (2) forward radiative transfer calculations, (3) sensor observation simulations, (4) Karhunen-Loève transformation and degree of freedom calculations, (5) antenna pattern deconvolutions, and (6) precipitation parameter (e.g., rain rate) retrieval algorithm development. The simulations facilitate investigation of precipitation parameter retrieval using low-pass filtered brightness temperature imagery from candidate passive microwave systems. The investigation also facilitates comparison of the relative merits of proposed radiometric systems such as the EOS Multispectral Imaging Microwave Radiometer (MIMR) and geosynchronous satellite sensors. Initial simulation results for components # 1-4 are described herein, and procedures for deconvolution (component # 5) and a statistical iterative approach to rain rate retrieval (component # 6) are outlined.

1. Background

In satellite-based passive remote sensing, both microwave and infrared frequencies are used to observe properties of atmospheric hydrometeors. An important feature of infrared imagery is the high spatial resolution available from instruments of moderate aperture size (< 1 m), even at geosynchronous distances. Due to the large hydrometeor extinction at infrared wavelengths, such sensors are unable to probe through most cloud cover. In contrast, multifrequency microwave remote sensing provides a valuable complementary capability in being able to probe through clouds and even some precipitation while retaining useful sensitivity to hydrometeors [1, 2]. The degree of sensitivity depends on the particular frequency of observation, the hydrometeor phase (liquid or ice) and the hydrometeor density and size distribution [3]. For example, frequencies below ~ 6 GHz respond significantly to only very strong precipitation, while frequencies above ~ 220 GHz respond to even light non-precipitating clouds such as cirrus.

Compared to the infrared, the precipitation probing capability of microwave observations greatly facilitates the measurement of precipitation parameters such as surface rain rate. Precipitation sensing capabilities have been demonstrated by a number of airborne and spaceborne microwave instruments, for example, the Advanced Microwave Precipitation Radiometer (AMPR) [4], the Millimeter-wave Temperature Sounder (MTS) [5], the Nimbus-E Microwave Spectrometer (NEMS) [6], the Scanning Multichannel Microwave Radiometer (SMMR) [7], and the DMSP Special Sensor Microwave/Imager (SSM/I) [8]. Measurements of surface precipitation rate facilitate hydrological studies involving water budget and runoff analyses.In addition, the relative simplicity of the forward radiative transfer relationship at microwave frequencies along with the wide available range of cloud penetration depths suggest that profiling of some precipitation parameters (e.g. rain rate and hydrometeor density, size, and phase) might be possible [9]. Measurements of water density profiles in precipitating systems would be particularly useful for severe storm tracking and estimating atmospheric heating profiles, which are in turn important in understanding global heat transport [10].

For applications in hydrology, severe storm tracking, operational meteorology and global change study, area-averaged estimates of the forementioned precipitation parameters with spatial resolutions of $\sim 1-5$ km and observed at time intervals of $\sim 30-60$ min are generally considered to be ultimately desirable [11, 12]. Further improvements in spatial or temporal resolution would yield only small marginal benefits. Degradations in spatial resolution to $\sim 25-50$ km would still yield useful data for some of the above applications, although the utility falls off quickly beyond this range. However, the accuracy of area-averaged estimates depends strongly on the spatial resolution, radiometric sensitivity and channel set of the observation system. Indeed, the forward transfer relationship is decidedly non-linear with respect to most hydrometeors parameters, especially at frequencies above ~ 23 GHz. In addition, there is often no unambiguous inverse relationship, particularly if observations are made over only a narrow range of frequencies. These

two effects, combined with (1) low-pass spatial sampling caused by large antenna footprints relative to the spatial scales of precipitation, (2) radiometric instrument noise, and (3) antenna calibration and gain pattern uncertainty compromise the accuracies obtainable from passive microwave imagery. Since the costs for overcoming the technological impediments causing these problems are quite high, it is of great importance to be able to predict the performance of candidate spaceborne sensor systems prior to implementation for cost/benefit tradeoff purposes.

During the last decade, several new geosynchronous (GEO) and low-Earth orbitting (LEO) passive microwave precipitation sensors with enhanced spatial resolution capabilities have been either studied, proposed or recently deployed:

1. Microwave Atmospheric Sounding Radiometer (MASR) GEO system: $\sim$ 4.4 aperture [13]
2. Geosynchronous Microwave Precipitation Radiometer (GMPR): $\sim$ 4 aperture [14]
3. LaRC Large Space Antenna (LSA): $\sim$ 15 – 40 meter GEO imaging sensor [12]
4. DMSP Special Sensor Microwave/Temperature Sounder (SSM/T-2)
5. Tropical Rainfall Measurement Mission (TRMM) Microwave Imager (TMI) [15]
6. Multispectral Imaging Microwave Radiometer (MIMR): $\sim$ 1.6-m LEO system for deployment during EOS-B [16]
7. Jet Propulsion Laboratory Synthetic Aperture Imaging Radiometer (SAIR) [17]

This list is not exhaustive, but simply representative. For the first three (GEO) systems, the most important advantage stems from the high temporal resolution available from the geosynchronous vantage point, although large apertures and/or high frequency channels are required to obtain reasonable spatial resolution. For the other systems, the low Earth orbitting configuration considerably simplifies the structural problems (and expenses) associated with large space antennas. However, the advantage of high temporal resolution is lost due to long revisit times. It can only be regained by implementing a small fleet of LEO sensors.

To assess the relative merits of the above listed and other candidate passive microwave sensor systems for precipitation measurement, numerical simulations of the multispectral imaging and retrieval processes as applied to spaceborne passive microwave precipitation measurement systems are being performed. The simulations are being based on realistic three-dimensional geophysical models, accurate sensor models, and optimal precipitation parameter retrieval algorithms. This paper discusses recent progress and the current state of the numerical simulations. A goal of these simulations is to develop precipitation parameter retrieval algorithms optimized for the channel set, noise and gain pattern characteristics, and observation geometry of a particular sensor.

The overall scope of the simulations includes all of the proposed sensors listed above, although the immediate application is being directed to three specific systems: (1) EOS MIMR (#8), using six channels at 6, 10.69, 18.7, 23.8, 36.5 and 89 GHz from low Earth orbit (705 km altitude), (2) LaRC LSA (#3), using nine window channels at 6, 10.69, 18.7, 36.5, 89, 166,

220, 340 and 410 GHz from geosynchronous orbit, and (3) LaRC LSA (#3), using two window channels at 18.7 and 36.5, one water vapor channel at 23.8 GHz, and five oxygen channels at 50.3, 52.8, 53.596, 54.400 and 54.940 GHz (a total of eight channels) from geosynchronous orbit.

Although we have targeted precipitation as the geophysical process of greatest interest, the retrieval of several other geophysical processes might be considered. For example, spaceborne measurements of temperature and water vapor profiles are also viable using passive microwave systems. However, the spatial and/or temporal resolution needs for measurement of these variables are not as demanding as for precipitation or cloud water. When compared with water vapor or temperature, precipitation parameter retrievals are of greater concern for two primary reasons: (1) the relationships between the parameters and the observables are highly nonlinear and even bimodal, and (2) convective precipitation cells and other storm features (e.g., hurricane eyewalls) can be as small as a few kilometers in size, and typically a factor of five smaller than the spatial scale of most temperature or water vapor structure. Thus, if practical precipitation measurement systems can be identified, temperature and water vapor measurements using the same systems will not require significantly more sophisticated hardware or retrieval algorithms.

The same can be said for sea ice detection. Here, spatial resolutions smaller than one kilometer are desirable, but the detection mechanism is relatively straightforward compared to precipitation retrieval algorithms and the time evolution of ice movement is relatively slow. Essentially, the problem requires a set of channels that exhibit a sensitivity difference to ocean water and sea ice, but can still probe through the atmosphere. This must be done at least once a day (or so). Here, high frequency window channels (e.g., at 37, 90, 166 and 220 GHz, including both vertical and horizontal polarizations) can be used since sea ice occurs only in cold latitudes where water vapor screening is small and high cloud opacity is not persistent. The necessary spatial resolution is obtainable by virtue of the narrow antenna beams available at these frequencies using apertures of practical size. In contrast, precipitation measurements are best performed using low frequency channels (e.g., 6, 10, 18 and 37 GHz) for which sub-Nyquist resolution is the overriding technological impediment (and hence, the overriding cost issue). Moreover, a geosynchronous system is not practical for sea ice observation due to the large incidence angle near the polar regions.

Soil moisture can evolve quickly, particularly during precipitation events. For hydrological purposes, spatial scales of several kilometers are ultimately desirable. However, since the soil moisture retrieval problem is predominantly linear [19], sub-Nyquist spatial resolution should cause no significant degradation in the resulting area-averaged soil moisture retrieval error. Moreover, since frequencies for soil moisture measurement are relatively low (near L-band), spaceborne systems with adequate spatial resolution will likely be designed as single-channel thinned-aperture interferometers [18]. Again, the spatial resolution problem as applied to multichannel precipitation sensing is of greater immediate interest.

In contrast to water vapor, temperature, sea ice and soil moisture, the radiative transfer through precipitation results in strong nonlinearities between the underlying hydrometeor parameters (e.g., water density, phase and particle size distribution) and the upwelling brightness temperatures. For sub-Nyquist systems, these nonlinearities can cause ambiguities in area-averaged retrievals of precipitation parameters. For example, using 37-GHz data from Wilheit *et al.* [20], a 50-mm/hr rain cell occupying 10 percent of the area of a sensor's footprint causes approximately the same brightness as a 1-mm/hr drizzle occurring over the entire area of the footprint, even though the area-averaged rain rates differ by a factor of five.

It is for the above reasons that we have focussed our simulation efforts on precipitation parameter measurements, with particular emphasis on maritime precipitation. As a practical matter, maritime precipitation is observable only from space, and moreover occurs over a larger portion of the Earth's surface than continental precipitation. In addition, continental precipitation is more readily amenable to ground-based radar observation, and is currently observed over a significant fraction of the industrialized northern hemisphere. Thus, we have given initial emphasis to simulations over ocean backgrounds. We have also emphasized geosynchronous systems. Precipitation events (particularly the convective type) evolve swiftly, with typical lifetimes of one to three hours. Thus, it is of particular interest to simulate precipitation measurements from geosynchronous orbit where short revisit times (less than one hour) can be achieved [21].

The simulation software, called the Passive Microwave Mapping and Retrieval Simulator (PMMRS), provides a flexible end-to-end simulation of a multispectral passive microwave imaging and retrieval system. The PMMRS models three primary processes: the forward radiative transfer process, the observation process, and the precipitation retrieval process. As shown in Figure 1, the forward radiative transfer process transforms three-dimensional microphysical cloud data into upwelling brightness imagery, the observation process transforms the upwelling brightness imagery into the brightness temperatures recorded by the antenna sensor, while the retrieval process estimates atmospheric parameters (e.g., rain rate) and compares them to parameters derived from the original microphysical cloud data. The PMMRS permits evaluating retrievals for user-selected combinations of sensor antenna specifications, channel sets, noise levels, observation geometry, and precipitation types. The overall goal of these mapping simulations is to quantitatively assess the effects of multispectral blurring on area-averaged errors in retrieved precipitation parameters such as surface rain rate and liquid and ice density profiles. In studying the resolution problem, the authors recognize that some severe mechanical and electrical requirements might be imposed in the implementation of the candidate imaging systems. However, the primary purpose of this study is to define the imaging needs based on the geophysical phenomena of interest, and to secondarily consider the (albeit formidable) hardware issues.

2. Forward Radiative Transfer Simulation

Microphysical raincell parameter data used to date is composed primarily of three-dimensional synthesized data from the Goddard Cumulus Ensemble (GCE) simulation of a developing convective storm system [22]. This data consists of a set of five time samples of a tropical squall computed using a numerical cloud evolution model from initial conditions measured during the Global Atmospheric Research Program Tropical Atlantic Experiment (GATE). Vertical profiles of pressure, temperature, relative humidity, liquid hydrometeor content and frozen hydrometeor content are given for each of 64 x 64 pixels. The horizontal spatial resolution is 1.5 km. The vertical resolution varies, but is typically 1 km, with twenty discrete levels.

Additional raincell microphysical has been obtained from a volume scan of a convective multicell system made using the CP-2 weather radar during the Cooperative Huntsville Meteorological Experiment (COHMEX, 1986) [23]. The reflectivities were converted to hydrometeor densities and mean size parameters using the Marshall-Palmer (MP) and Sekhon-Srivastava (SS) size relationships. Particle phase was assumed to be liquid below the freezing level, solid above the temperature of ice nucleation (assumed to be -30° C), and linearly mixed in between. A 6.5 dB ice reflectivity correction was applied [24].

The microphysical raincell data was mapped into upwelling brightness images (T_B) using the iterative forward radiative transfer model developed by Gasiewski and Staelin [25]. This is a planar-stratified scattering-based model that uses the specified surface reflectivity and atmospheric parameters (temperature, pressure, relative humidity and hydrometeor densities, size distributions and phases) at levels from the surface to $\sim$ 20 km altitude. Brightness temperature imagery over a calm ocean was computed for the following microwave frequencies: 6, 10.69, 18.7, 23.8, 36.5, 50.3, 52.8, 53.596, 54.4, 54.94, 89, 118.75+(0.12, 0.22, 0.37, 0.67, 1.27, 2.07), 166, 183.31+(0.0, 1.0, 3.0, 7.0), 220, 325.153+(0.0, 1.0, 3.0, 7.0, 9.0), 340, and 410 GHz. These frequencies include all significant microwave "window-channels" along with those channels near the water vapor and oxygen absorption lines that are deemed to be the most essential for tropospheric measurement purposes. For the absorption line channels, the offset frequencies from the respective line centers are listed in parentheses. The resulting sets of brightness maps are catalogued in Table 1.

Typical full-resolution brightness imagery for the microwave window channels is shown in Figs. 2a-d. These figures include a representative set of three GCE time samples and the single COHMEX sample. Here, whiter areas correspond to warmer brightnesses. In all imagery, the warming caused by precipitation over the reflective ocean surface is readily seen in many of the channels below $\sim$ 23 GHz. This is expected since precipitation is predominantly absorptive at these low frequencies. Thus, emission from the relatively warm hydrometeors increases the

upwelling brightness above the cold values characteristic of clear-air regions over ocean surfaces. In contrast, scattering of the cold cosmic background radiation by ice over the storm cores is apparent in all higher-frequency window channels ($\sim$ 18 GHz and above). The bimodal brightness structure clearly seen in the imagery of the 18.7- and 36.5-GHz channel is caused by cold oceanic reflectance outside of the storm, a warming caused by thin absorbing clouds near the periphery of the storm, and a cooling due to ice scattering at the center of the storm.

Corresponding full-resolution imagery for the oxygen and water vapor channels for GCE 3 is shown in Figs. 3 and 4. As expected, the storm structure is least visible in the most opaque of these channels, that is, those channels with greatest integrated opacity. In the case of the oxygen channels, the altitude of the raincell top can be estimated by virtue of the multiplicity of channel probing depths obtainable using a series of channels with successively increasing opacities [23]. These high-resolution brightness maps and others for similar precipitation cases are used as the basis for all ensuing statistical calculations and imaging and retrieval studies.

3. Sensor Observation Simulation

Candidate sensors are modelled by aperture size, aperture illumination field distribution, orbital altitude h, and field-of-view (FOV). In addition, each sensor channel $n = 1 \ldots N$ is modeled by the following characteristics: center frequency f_n, bandwidth W_n, and double-sideband receiver noise temperature $T_{\mathrm{rec}\,n}$. A diffraction-limited aperture is assumed for all channels, thus giving rise to spot resolutions that increase with channel center frequency. Collectively, these parameters determine the single-spot brightness sensitivity of each channel:

$$\sigma_{SS\,n} = \frac{T_{\mathrm{sys}\,n}}{\sqrt{W_n \tau}} \tag{1}$$

where $T_{\mathrm{sys}\,n} = T_{\mathrm{rec}\,n} + T_{\mathrm{ant}\,n}$ is the system noise temperature (receiver plus antenna), and τ is the integration (or dwell) time for a single sample. For Earth observation, typical antenna temperatures $T_{\mathrm{ant}\,n}$ are between 100 and 300 K, depending on the center frequency and geophysical state.

For GEO systems, τ is derived from the image FOV, orbital altitude, and the total scene acquisition time T_s, assuming uniform rectilinear sampling of the subsatellite (equatorial) scene at intervals determined by the Nyquist sampling criterion for the highest frequency channel (Fig. 5a). Denoting this sampling angle by θ_S (in radians), we have:

$$\tau_{geo} = T_s \frac{[h\,\theta_S]^2}{\mathrm{FOV}}\,\eta_s \tag{2}$$

where $h = 3.5885 \times 10^4$ km and the FOV is in km^2. The parameter η_s is the scan efficiency, which is the fraction of time spent acquiring radiometric scene data as opposed to performing supporting operations such as calibration and scan turnaround. For the GEO simulation studies, the FOV, total acquisition time and scan efficiency are taken to be 1,000 km $\times$1,000 km, T_s = 30 minutes and 85%, respectively.

For LEO systems, τ is derived from the angular swath width θ_W and altitude h, assuming a cross-track raster scan with the subsatellite raster spacing determined by Nyquist criterion for the highest frequency channel (Fig. 5b):

$$\tau_{leo} = \frac{\theta_N^2\, h}{\theta_W} \sqrt{\frac{h + 6356.8}{3.986 \times 10^5}}\,\eta_s \tag{3}$$

where θ_S, θ_W are in radians and h is in km. For purposes of antenna characterization, we use a cross-track scanning geometry of angular width 90°, η_s =45% and h = 705 km for the MIMR simulations. [1] We also assume that scene mapping takes place using single (non-redundant)

[1] While in view of the fact that MIMR is a conical scanning instrument, an intracomparison of antenna characteristics can be most easily accomplished using the chosen raster scan geometry. Conical scans would produce similar sensitivities and resolutions, hence a meaningful comparison can be made.

receivers for each channel. If redundant receivers are used to provide parallel scene mapping, the effective integration time can be increased by the number of redundant receivers N_{rec}. This reduces each σ_{SS_n} value by $1/\sqrt{N_{\text{rec}}}$. [2]

To simulate the observation process, four operations are performed: (1) an antenna gain pattern (or, spot pattern) is calculated, (2) the upwelling brightness temperatures are convolved with the corresponding spot pattern, (3) the convolved imagery is sampled at the Nyquist rate, and (4) pseudo-random instrument noise is added. Discretized spot patterns are generated from the antenna gain pattern sampled at appropriate locations on the Earth's surface. Gain patterns are based on the specific aperture field distribution and wavelength. Without significant loss of generality, apertures are assumed to be circular of diameter D, and have a linearly polarized aperture field with uniform phase taper and radial amplitude taper:

$$\overline{E}(r,\theta) = E_o \hat{x} \left[1 - \left(\frac{2r}{D}\right)^2\right]^p \tag{4}$$

Here, p is a parameter that describes the degree of illumination taper. The resulting family of gain patterns are described by Bessel functions [26]:

$$g_n(p;\theta) = g_o \left| \frac{J_{p+1}\left(\frac{\pi D f_n}{c} \sin\theta\right)}{\left(\frac{\pi D f_n}{c} \sin\theta\right)^{p+1}} \right|^2 \tag{5}$$

where g_o is a constant, and c is the speed of light. By sampling the continuous gain function, the diagonal elements of the gain matrix $\overline{\overline{g}}$ are obtained:

$$\overline{\overline{g}}_{ij} = \begin{bmatrix} g_1(p;\theta_{ij}) & 0 & & \\ 0 & g_2(p;\theta_{ij}) & & \\ & & \ddots & \\ & & & g_N(p;\theta_{ij}) \end{bmatrix} \tag{6}$$

$$\theta_{ij} = \tan^{-1}\left(\frac{\Delta R}{h}\sqrt{i^2+j^2}\right) \tag{7}$$

where ΔR is the horizontal spatial resolution of the brightness maps (see Table 1).

Since the Fourier transform of the antenna gain is related to the aperture electric field correlation function [27], the Nyquist sampling interval can be determined from the aperture size. This follows from the fact that the aperture field correlation function is zero for spatial displacements greater than D. Accordingly, if no aliasing is to occur, the maximum angular sampling interval θ_S must be:

$$\theta_S = \frac{c}{2Df_N} \tag{8}$$

[2] Redundant receivers may be the only practical means of meeting the slew requirements for some large filled-aperture systems, for example, the MIMR 4.4-m system.

The corresponding spatial sampling interval is:

$$R_S = h\theta_S = \frac{ch}{2f_N D} \tag{9}$$

This is the Nyquist sampling interval. It must be distinguished from the the 3-dB spot size (or, "3-dB resolution") of the highest frequency channel, even though the 3-dB measure is commonly referred to in discussing system resolution. Depending on the aperture illumination taper, R_S is from two to nearly four times smaller than the 3-dB spot size at the highest frequency, which follows:

$$R_{3\mathrm{dB},N} = h\theta_{3dB,N} = \alpha(p)\frac{ch}{f_N D} = 2\alpha(p)R_S \tag{10}$$

where the constant α (Table 2) is a weak function of p, ranging between approximately one to two ([26], pp.195). Note that sampling at R_N does not guarantee that all spatial frequencies in the underlying brightness imagery are measured.

The discretized spot pattern is subsequently truncated so that the convolution in Eq. 14 is over a finite range of indices. To determine the indices at which the pattern is truncated, the beam efficiency functions $\eta_B(p;\theta)$ are used. These functions are the fraction of beam energy in the conical solid angle from the beam axis out to a given angle θ (Fig. 6):

$$\eta_B(p;\theta) = \frac{\displaystyle\int_0^{\frac{\pi D f_n}{c}\sin\theta} \frac{J_{p+1}^2(u)}{u^{2p+1}\sqrt{1-\left(\frac{uc}{\pi D f_n}\right)^2}}\,du}{\displaystyle\int_0^{\frac{\pi D f_n}{c}} \frac{J_{p+1}^2(u)}{u^{2p+1}\sqrt{1-\left(\frac{uc}{\pi D f_n}\right)^2}}\,du} \tag{11}$$

The curves show that 3-dB beam efficiencies greater than $\sim$ 55% cannot be obtained using simple aperture tapers. Note that the illumination taper p affects the main beam efficiency (or, null-to-null efficiency) considerably, particularly for weak tapers ($p = 0$ or 1). Specifically, main beam efficiencies greater than $\sim$ 86% cannot be achieved with a uniform taper ($p = 0$), but require a more gradual taper ($p \geq 1$). However, increasing p also increases the 3-dB spot size by virtue of the factor α in Eq. 9. The aperture efficiency:

$$\eta_A(p) = \frac{2p+1}{(p+1)^2} \tag{12}$$

is a measure of the effective use of aperture area in increasing main beam gain, and is also reduced (Table 2) as p increases.

Using Eq. 11, we find that truncation near the third null for the lowest frequency channel insures that virtually all (> 99.8%) of the beam energy is accounted for in the discretized spot patterns for all channels and for all tapers $p \geq 1$. An minor exception occurs for the uniform taper ($p = 0$) for which only 96% of the beam energy is contained within the third null for

the lowest frequency channel. To account for both (1) radiation from far sidelobes and (2) the undetermined constant g_o the truncated gain matrix is subsequently normalized so that:

$$\sum_{i=-ig}^{i=ig} \sum_{j=-jg}^{j=jg} \overline{\overline{g}}_{ij} = \overline{\overline{I}} \tag{13}$$

where $\overline{\overline{g}}_{ij}$ is zero for $|i| > ig$ and $|j| > jg$, and $\overline{\overline{I}}$ is the identity matrix. This insures that the spatial response is unitary over the $(2ig + 1)(2jg + 1)$ gain values.

To simulate the observation process, discretized gain patterns are subsequently convolved with the brightness temperature imagery then corrupted by additive white noise. Mathematically:

$$\begin{aligned} \overline{T}_{A\,ij} &= \overline{\overline{g}}_{-i,-j} ** \overline{T}_{B\,ij} + \overline{n}_{ij} \\ &= \sum_{i'=-\infty}^{\infty} \sum_{j'=-\infty}^{\infty} \overline{\overline{g}}_{i'-i,j'-j}\, \overline{T}_{B\,i'j'} + \overline{n}_{ij} \end{aligned} \tag{14}$$

where: $\overline{T}_{B\,ij}$ is the multispectral scene brightness at pixel i, j ($i = 1 \ldots imax, j = 1 \ldots jmax$), $\overline{T}_{A\,ij}$ is the associated multispectral antenna temperature at pixel i, j, $\overline{\overline{g}}_{ij}$ is the sensor's multispectral discretized spot pattern (or, gain) matrix, and $\overline{n}_{ij}$ is white Gaussian pseudo-random observation noise with covariance matrix:

$$\overline{\overline{R}}_{nn\,ij} = \langle \overline{n}_{i'j'}\, \overline{n}^{t}_{i'-i,j'-j} \rangle = \begin{bmatrix} \sigma^2_{T1} & 0 & & \\ 0 & \sigma^2_{T2} & & \\ & & \ddots & \\ & & & \sigma^2_{TN} \end{bmatrix} \delta_i \delta_j \tag{15}$$

where ^{t} is the transpose operator and δ is the Kronecker delta function. In Eq. 14, $**$ denotes two-dimensional convolution. In performing the convolution, the brightness images are padded with clear-air spectra at locations outside the range of available data, effectively extending the images beyond $imax jmax$ pixels. Note that since the map resolution ΔR is smaller than the resolution of the sensor's sampling grid R_S, the map noise standard deviation σ_{Tn} must be adjusted relative to the single-spot standard deviation σ_{SSn} by the relative sampling rates:

$$\sigma_{Tn} = \sigma_{SSn} \frac{R_S}{\Delta R} \tag{16}$$

For the LSA eight-channel system, the map resolution ΔR is considerably smaller than the Nyquist sampling interval, although ΔR is comparable to R_S for the MIMR and LSA nine-channel systems. Overall, the above simulation of the observation process is equivalent to sampling the raster at a resolution R_S, then resampling to a standard resolution ΔR. For the MIMR and LSA systems, the assumed system sensitivity parameters, resolutions and associated integration times and single-spot sensitivities are listed in Tables 3 and 4.

Figs. 7a-c show the MIMR six-channel imagery before and after convolution with the sensitivity patterns of circular 4.4-m and 1.6-m quadratically-tapered ($p = 1$) aperture distributions at a 705-km orbital altitude. Here, R_S = 0.27 and 0.74 km (respectively) while the 3-dB resolutions are $R_{3dB,N}$ = 0.68 and 1.89 km. For illustration, the 210-minute GCE frame (GCE 4) has been chosen, and instrument noise has not been added. In practice, the convolved antenna temperature imagery would actually be downsampled at the Nyquist resolution of the highest frequency (89-GHz) channel. To obviate the need for subsequent upsampling to the resolution ΔR of the unconvolved brightness maps, we show the antenna temperature imagery at this same resolution.

With a 4.4-m aperture, the fine storm structure observed in the full resolution imagery is revealed at frequencies as low as 10.69 GHz, and the 6-GHz channel shows some of the overall shape characteristics. However, with the 1.6-m aperture (the size proposed for MIMR during EOS-B [16]), the fine storm structure is visible only at frequencies equal to or higher than 18.7 GHz. At 6-GHz, the spot size for the 1.6-m aperture is $\sim$ 28 km, and even the gross shape seen in the full resolution imagery is lost. In both convolved cases the 89-GHz channel has a small enough 3-dB spot size ($\sim$ 0.7 and 1.9 km for the 4.4- and 1.6-m apertures, respectively) to reveal virtually all of the features seen in the full resolution imagery.

Figs. 8a-c show the nine-channel GEO LSA imagery for GCE 4 both before and after convolution with the sensitivity patterns associated with circular 40-m and 15-m diameter apertures with quadratically-tapered ($p = 1$) field distributions. Even with the 40-m aperture, much of the fine storm structure is lost in the process of imaging. However, some of the bimodal brightness structure near the storm edge remains observable at 36.5 GHz. With a 15-m aperture, very little bimodal structure remains at even 36.5 GHz. Although the blurring at frequencies of 166 GHz and higher is small for both 15- and 40-m apertures (spot sizes are less than $\sim$ 6 km), there is considerably less information on fine storm structure at these frequencies. Similarly, Figs. 9a-c show the eight-channel (low-frequency) GEO LSA imagery for GCE 4 both before and after convolution with the sensitivity patterns associated with circular 40-m and 15-m diameter apertures with quadratically-tapered ($p = 1$) field distributions. Again, much of the fine storm structure is lost even in the highest frequency (5-mm band) channels.

To reduce the complexity of the overall simulation, some potentially interesting aspects of the observation portion are tacitly avoided here. For instance, the polarization properties of the sensor and the upwelling brightness field are not considered. Also not considered are the effects of spot elongation or radiative transfer effects caused by different slant-path distances through the atmosphere and/or surface emisivity changes at off-nadir angles, as would be encountered at the extreme spots of LEO and wide-FOV GEO systems. These features are not considered to be important in the initial analysis of the expected performance of spatial resolution limited sensors. We note, however, that gain patterns for radiometric interferometers (or Synthetic

Aperture Interferometric Radiometers, SAIR's [28]) can be analyzed with the same formalism and software as presented here for filled-aperture imaging radiometers. For the SAIR, the sensitivity pattern of the array would be substituted for the aperture gain pattern. Two minor differences are (1) the SAIR gain function is not positive definite, and (2) the influence of grating lobes cannot be neglected, especially in thinned-aperture SAIR arrays.[3]

Upon integration into the multispectral deconvolution experiments and precipitation retrieval simulations, some issues that will be able to be quantitatively resolved using the above formalism include the tradeoff between beam efficiency and spot size, the effects of antenna gain pattern uncertainties and the effects of 3-dB raster sampling as opposed to Nyquist sampling.

[3]Due to the structural complexities of filled-aperture sensors, SAIR's may be the only practical method of implementing particularly large apertures.

4. Karhunen-Loève Analysis

The convolved $\overline{T}_A$ imagery has been analyzed for loss in observational degrees of freedom using the Karhunen-Loève (KL) transformation (also called principal components analysis, or the method of empirical orthogonal eigenfunctions). The unitary KL transform rank-orders the dominant spectral modes in the $\overline{T}_A$ imagery by the modes' signal-to-noise ratios (SNR's) [29, 30]. The SNR's of the $\overline{T}_A$ KL spectral modes are then compared to those of the $\overline{T}_B$ KL modes to determine the number of observational degrees of freedom in the observed imagery relative to the number of degrees in the full resolution imagery.

The KL transform is determined by the eigenvectors of the spectral covariance matrix $\overline{\overline{R}}_{T_A T_A}$. One way to estimate this matrix is to assume ergodicity, that is, that spatial averaging over the pixels of an image yields statistics identical to those obtained by ensemble averaging over pixels chosen from a large set of independent images. Strictly, this is only true for two-dimensionally ergodic random processes. In the simulated $\overline{T}_B$ and $\overline{T}_A$ imagery, this condition is not quite satisfied. However, the lack of a large ensemble of independent images requires this practice; the consequences of its effects will be discussed later in this section.

Assuming spatial ergodicity, the spectral covariance for $\overline{T}_A$ becomes:

$$\begin{aligned} \overline{\overline{R}}_{T_A T_A} &= \langle (\overline{T}_A - \langle \overline{T}_A \rangle)(\overline{T}_A - \overline{T}_A)^t \rangle \\ &\approx \frac{\sum_{i=1}^{i\max} \sum_{j=1}^{j\max} (\overline{T}_{Aij} - \overline{T}_B^{(ca)})(\overline{T}_{Aij} - \overline{T}_B^{(ca)})^t}{i\max j\max - 1} \end{aligned} \tag{17}$$

where the outer expectation operator $\langle \cdot \rangle$ is computed by space-averaging over the ensemble of all $i\max j\max$ pixels in the image and we have arbitrarily defined $\overline{T}_B^{(ca)}$ to be the expected value of $\overline{T}_B$ in the absence of hydrometeors. The eigenvectors and associated eigenvalues of $\overline{\overline{R}}_{T_A T_A}$ are found by diagonalization:

$$\overline{\overline{R}}_{T_A T_A} = \overline{\overline{E}} \begin{bmatrix} \lambda_1 & 0 & & \\ 0 & \lambda_2 & & \\ & & \ddots & \\ & & & \lambda_N \end{bmatrix} \overline{\overline{E}}^t \tag{18}$$

where the rows of the KL transformation matrix $\overline{\overline{E}}$ are the eigenvectors of $\overline{\overline{R}}_{T_A T_A}$. These eigenvectors provide a measure of the contribution from each channel of the brightness imagery to each KL image:

$$\overline{k}_{Aij} = \overline{\overline{E}} (\overline{T}_{Aij} - \overline{T}_A^{(ca)}) \tag{19}$$

An important property of the KL imagery is that all KL channels are uncorrelated in the sense of Eq. 17. Note this does not imply that they are statistically independent. Rather,

they are independent only in their second order statistics. Indeed, the KL transform (as based on Eq. 17) produces complete statistical independence only in the case where $\overline{T}_A$ is a jointly Gaussian random process. Since $\overline{T}_A$ does not satisfy this condition, the joint moments of $\overline{k}$ for orders higher than two are generally nonzero.

For each KL channel, the associated eigenvalue λ_n is its total expected energy. To determine the fraction of this energy containing geophysical information (versus noise), the eigenvalue must be compared with the observational noise energy in the channel. Provided that the sensitivities σ_{Tn} are identical over all sensor channels, this same noise energy will appear in each KL channel. This is a consequence of the unitary property of the transform matrix $\overline{\overline{E}}$. In this case, the signal-to-noise ratio (SNR) for each KL channel is:

$$\mathrm{SNR}_n = \frac{\lambda_n - \sigma_{Tn}^2}{\sigma_{Tn}^2} \tag{20}$$

In practice, some sensor channels will be more sensitive than others, thus the σ_{Tn}'s will be different. To accommodate observational noise level variations among sensor channels, it is necessary to prewhiten the brightness imagery prior to computation of the covariance matrix:

$$\overline{T}'_{Aij} = \begin{bmatrix} 1/\sqrt{\sigma_{T_1}} & 0 & & \\ 0 & 1/\sqrt{\sigma_{T_2}} & & \\ & & \ddots & \\ & & & 1/\sqrt{\sigma_{T_N}} \end{bmatrix} \overline{T}_{Aij} \tag{21}$$

$$= \begin{bmatrix} 1/\sqrt{\sigma_{T_1}} & 0 & & \\ 0 & 1/\sqrt{\sigma_{T_2}} & & \\ & & \ddots & \\ & & & 1/\sqrt{\sigma_{T_N}} \end{bmatrix} \overline{\overline{g}}_{-i,-j} ** \overline{T}_{Bij}$$

$$+ \begin{bmatrix} 1/\sqrt{\sigma_{T_1}} & 0 & & \\ 0 & 1/\sqrt{\sigma_{T_2}} & & \\ & & \ddots & \\ & & & 1/\sqrt{\sigma_{T_N}} \end{bmatrix} \overline{n} \tag{22}$$

where $\overline{T}'_{Aij}$ is the noise-whitened antenna temperature imagery. The purpose of this step is to force the noise component of the signal $\overline{T}'_A$ to be white. Since $\overline{\overline{E}}$ is unitary this noise remains white under the KL transformation. That is, the noise energy in $\overline{k}_A$ is uncorrelated and distributed equally among all KL channels. This would not follow if the noise component in $\overline{T}'_{Aij}$ was colored. Prewhitening by Eq. 22 also scales the transformed observational noise energies in all KL channels to unity. Thus, the KL-channel SNR's are:

$$\mathrm{SNR}_n = \lambda_n - 1 \tag{23}$$

where the λ_n's are the eigenvalues of $\overline{\overline{R}}_{T'_A T'_A}$. Effectively, prewhitening allows comparison of the information contained in the brightness channels on a "channel-noise equivalent" basis.

By rank ordering the SNR's of the KL channels the relative importance of each combination of sensor channels (also referred to as a "KL mode" or "KL image") can be assessed. For example, for the full-resolution six-channel MIMR imagery, the most dominant KL image (i.e., with the largest SNR, 28.40 dB) shows the overall shape of the GCE 4 cell extremely well (Fig. 10a, leftmost image). The second and third modes (next two from left, 18.60 and 4.80 dB, respectively) respond primarily to the bimodal brightness signature near the partially transparent edges of the cell. The other three modes are primarily noise (rightmost images), as suggested by the their low SNR's. The adjoining eigenvector plots (Fig. 11a) reveal that the most dominant mode is essentially the spectral difference between the 23.8- and 89-GHz channels. We interpret this mode as responding to the strongly-varying scattering signature caused by ice aloft. The second KL mode is a combination of the scattering signature from the high frequency channels and the spectral difference between the 6- and 10.69-GHz channels, and appears to be sensitive to the radiometrically-thin periphery of the storm. The other modes are successively more difficult to interpret. Indeed, there is no guarantee that any KL mode has a meaningful geophysical interpretation.

The KL-mode SNR's for the full-resolution ($\overline{T}_B$) and convolved ($\overline{T}_A$) brightness imagery can be used to estimate the loss in number of observable degrees of freedom caused by the broadness of the antenna pattern. As seen in Figs. 10b and c, the KL modes for the convolved MIMR imagery exhibit monotonically decreasing SNR's, indicative of a progressive loss of spectral variance caused by the spatial filtering of the antenna. A comparison of the SNR's (Figs. 10 and 12) for this imagery shows a reduction of $\sim$ 1.6 dB in the third mode from the full resolution to the 4.4-m case, then additional reductions of $\sim$ 1.3 dB and $\sim$ 1.5 dB in the second and third modes (respectively) from the 4.4-m case to the 1.6-m case. These reductions are attributed to the relatively large dependence of modes 2 and 3 on the lower frequency channels for which spatial resolution is adversely affected by aperture size reductions. In contrast, the dominant mode SNR's show insignificant reductions with aperture size, reflecting the fact that the dominant KL mode depends mostly on the high frequency channels for which spatial resolution is better.

Further insight into the effects of varying spatial resolution can be seen by examining the eigenvectors in Fig. 11a-c. Foremost, there is relatively little difference in the eigenvectors for a given mode as the resolution is changed. This suggests that no gross changes in the spectral characteristics of the brightness imagery occur over the range of spatial resolutions being considered. However, some changes in the relative contributions from the six MIMR channels can be seen. In mode 1, the contribution from the 6- and 10.69-GHz channels decreases by a factor of $\sim$ 2 from full-resolution to the 1.6-m case, thus indicating a reduction in signal variance in the low-frequency channels. However, the high frequency channels remain strong contributors, indicating that spatial resolution is good for all cases. In mode 2, the contribution from the low-frequency channels is relatively small, and changes sign from the full resolution to

the 1.6-m case. This suggests that the contribution to the bimodal structure of KL mode 2 from the lowest frequency channel is reduced by spatial filtering. In mode 3, the contribution from the low frequency channels decreases markedly from full resolution to 1.6-m resolution, again indicating a decreasing variance.

However, caution must be exercised in interpreting the KL mode SNR's in an absolute sense. The first (and most obvious) reason is that the SNR's have been derived from only a single time frame (GCE 4) of a computer-generated brightness field. Ideally, a large ensemble of real images would be used. A more subtle reason arises from the non-ergodicity of the precipitation cell brightness temperatures. Since each cell is finite in extent, an essential question arises as to what fraction of the image area should be padded with noisy clear-air brightness temperatures. The larger this padding, the smaller the resulting eigenvalues λ_n. Thus, the eigenvalues (and hence the SNR's) depend on the size of the cell in relation to the size of the image. To quantify this relation, let the number of pixels used in the space-averaging process of Eq. 17 be $N_p = i_{\max} j_{\max}$, and the resulting eigenvalues and SNR's be λ_n and SNR_n, respectively. Then padding the image with additional noisy, clear-air pixels will yield a larger image with $N_p' = i'_{\max} j'_{\max}$ pixels, where $N_p' > N_p$. The eigenvalues of the padded imagery will be correspondingly smaller, as determined by the number of additional pixels:

$$\lambda_n' = \lambda_n \frac{N_p}{N_p'} + \frac{N_p' - N_p}{N_p'} \tag{24}$$

Then from Eq. 23, it follows that:

$$\mathrm{SNR}_n' = \mathrm{SNR}_n \left(\frac{N_p}{N_p'} \right) \tag{25}$$

or, in decibels:

$$\mathrm{SNR}_n'\,(\mathrm{dB}) = \mathrm{SNR}_n\,(\mathrm{dB}) + 10 \log_{10} \left(\frac{N_p}{N_p'} \right) \tag{26}$$

Thus, the KL mode SNR's for precipitation cell imagery are meaningful only to within an arbitrary additive constant which depends on the size of the clear-air portion outside the cell. However, for identically sized images, the SNR's can be meaningfully intercompared. Visual inspection of the KL imagery can also provide a meaningful qualitative determination of the usefulness of a mode.

For the nine-channel GEO LSA system there are nine KL modes, of which perhaps 4-6 provide significant information (Figs. 13a-c). Again, the KL modes for the convolved imagery exhibit monotonically decreasing SNR's, indicating a progressive loss of spectral variance as the aperture size decreases. A comparison of the SNR's (Fig. 15) shows a reduction of $\sim$ 2 dB in the dominant mode SNR from the full resolution to either the 15-m or 40-m cases, and much larger reductions ($\sim$ 10 dB or more) for the second and higher order modes.

Again, the eigenvectors for a given mode (Figs. 14a-c) exhibit no gross changes as the spatial resolution is varied. As in the MIMR case, mode 1 consists primarily of the difference between the high frequency channels (which cool in response to scattering by ice aloft) and the low frequency channels (which warm in response to rain and cloud water). This effectively produces a map of the cell. Thus, the mode 1 eigenvector is a good indicator of the relative importance of the high-frequency millimeter and submillimeter channels (e.g., 89, 166, 220, 340 and 410 GHz) for precipitation cell mapping. While the variances of the channels above 89 GHz fall off with frequency, the diffraction-limited resolution of these channels increases. From the KL analysis, it appears that this tradeoff results in the the high frequency channels contributing most of the variance to the dominant mode. As aperture size (and hence resolution) decreases, the contribution from the low frequency channels further diminishes, illustrating the loss of variance from these channels caused by spatial filtering.

For the eight channel GEO LSA system, approximately three KL modes provide significant information (Figs. 16a-c). As seen in the eigenvectors for these channels (Figs. 17a-c), the 5-mm band oxygen channels respond in approximately the same manner to precipitation. Of course, the primary purpose for the five oxygen channels would be for temperature sounding. If precipitation were the only concern, only the 50.3 GHz channel would be used. The dominant KL mode is primarily comprised of the difference between those channels that respond to precipitation by primarily increasing their brightness and those that respond by decreasing their brightness. As the aperture size decreases, the SNR of the dominant mode drops by 2 dB for the 40-m case, then another 2 dB for the 15-m case(Fig. 18). The SNR for all higher order modes are more significantly affected.

It is of interest to note that the eigenvectors for a given system (as computed using Eq. 18) are relatively insensitive to the time of sampling, that is, all frames catalogued in Table 1 result in similar sets of eigenvectors. (The SNR's differ, but this is the result of the size and intensity of the precipitating region in relation to the clear air surrounding it.) Thus, the eigenvectors for a given channel set can be considered to be quite "universal" in that they are unique to the system as well as to the class of meteorological event (in this case, convective precipitation). This has also been observed in 118-GHz imagery of storm cells, where it has been found that approximately 2-3 unique observable modes are available from realistic 118-GHz imaging systems observing convective precipitation [23]. This suggests that retrieval algorithms can be constructed using a reduced set of inputs variables, namely, the KL modes. In addition, it suggests that compression of images for coding and archival purposes can be accomplished with a high ratio of compression (typically a factor of five to ten).

5. Multispectral Antenna Pattern Deconvolution

The KL analysis provides a measure of the number of spectral degrees of freedom produced by precipitation in the observed $\overline{T}_A$ imagery. It does not, however, provide a measure of the spatial-frequency information lost by filtering the $\overline{T}_B$ imagery with the multispectral sensitivity pattern. To quantify the loss of spatial-frequency information and at, the same time, to demonstrate the usefulness of the KL spectral modes, a statistically optimal deconvolution of the multispectral spot pattern and the associated error caused in the observation and deconvolution process is being investigated. The multispectral statistical deconvolution (MSD) operator is necessarily linear, and is formulated to minimize the expected error between the full-resolution brightness imagery and the deconvolved imagery.

The basic procedure for MSD, described by Rosenkranz [31], requires convolving the observed $\overline{T}_A$ with an optimal shift-invariant deconvolution operator $\overline{\overline{d}}_{ij}$ to obtain an estimate $\hat{\overline{T}}_B$ of $\overline{T}_B$:

$$\hat{\overline{T}}_{B\,ij} = \overline{\overline{d}}_{ij} \ast\ast \overline{T}_{A\,ij} \tag{27}$$

By requiring that the error between $\hat{\overline{T}}_B$ and $\overline{T}_B$ be uncorrelated with the observations $\overline{T}_A$:

$$\langle (\hat{\overline{T}}_{B\,ij} - \overline{T}_{B\,ij}) \overline{T}^{t}_{A\,i'j'} \rangle = 0 \tag{28}$$

where all possible values of i, j, i', j' are considered, the minimum mean-square-error estimator $\overline{\overline{d}}$ can be shown to follow:

$$\overline{\overline{d}}_{ij} \ast\ast \langle \overline{T}_{A\,ij} \ast\ast \overline{T}^{t}_{A\,-i,-j} \rangle = \langle \overline{T}_{B\,ij} \ast\ast \overline{T}^{t}_{A\,-i,-j} \rangle \tag{29}$$

This is recognized as an application of the orthogonality principle in estimation theory. In contrast to the spatial averaging used in the KL analysis, the ensemble averaging must be performed over a number of statistically independent images. The reason for the difference is that spatial correlations (i.e., correlations between different pixels) are required to be incorporated into the statistics in Eq. 28, whereas the KL analysis required no inter-pixel statistical information.

Using the two-dimensional discrete Fourier transform (denoted by $\mathcal{F}$), $\overline{\overline{d}}$ can be represented in the discrete spatial-frequency domain as:

$$\overline{\overline{D}}_{uv} = \frac{1}{i\text{max} j\text{max}} \sum_{i=0}^{i\text{max}-1} \sum_{j=0}^{j\text{max}-1} \overline{\overline{d}}_{ij}\, e^{-j2\pi(ui/i\text{max} + vj/j\text{max})} \tag{30}$$

where the integer variables u, v denote discrete spatial frequencies separated by increments of $(i\text{max}\Delta R)^{-1}$ and $(j\text{max}\Delta R)^{-1}$, respectively. Using the convolution-multiplication property of Fourier transform pairs and Eq. 14, we can write $\overline{\overline{D}}$ as:

$$\overline{\overline{D}}_{uv} = \mathcal{F}[\overline{\overline{d}}_{ij}] = \mathcal{F}[\langle \overline{T}_{B\,ij} \ast\ast \overline{T}^{t}_{A\,-i,-j} \rangle] (\mathcal{F}[\langle \overline{T}_{A\,ij} \ast\ast \overline{T}^{t}_{A\,-i,-j} \rangle])^{-1}$$

$$
\begin{aligned}
&= \mathcal{F}\left[\left\langle \overline{T}_{B\,ij} \ast\ast (\overline{g}_{ij} \ast\ast \overline{T}_{B\,-i,-j} + \overline{n}_{-i,-j})^{t} \right\rangle\right] \\
&\quad \left(\mathcal{F}\left[\left\langle (\overline{g}_{-i,-j} \ast\ast \overline{T}_{B\,ij} + \overline{n}_{ij}) \ast\ast (\overline{g}_{ij} \ast\ast \overline{T}_{B\,-i,-j} + \overline{n}_{-i,-j})^{t} \right\rangle\right]\right)^{-1} \\
&= \mathcal{F}\left[\left\langle \overline{T}_{B\,ij} \ast\ast (\overline{g}_{ij} \ast\ast \overline{T}_{B\,-i,-j})^{t} \right\rangle\right] \\
&\quad \left(\mathcal{F}\left[\left\langle (\overline{g}_{-i,-j} \ast\ast \overline{T}_{B\,ij}) \ast\ast (\overline{g}_{ij} \ast\ast \overline{T}_{B\,-i,-j})^{t} \right\rangle + \left\langle \overline{n}_{ij} \ast\ast \overline{n}^{t}_{-i,-j} \right\rangle\right]\right)^{-1} \\
&= \left(\mathcal{F}[\overline{T}_{B\,ij}]\,\mathcal{F}[\overline{T}_{B\,ij}]^{\dagger}\right) \mathcal{F}[\overline{g}_{ij}] \left(\mathcal{F}[\overline{g}_{ij}]^{\dagger} \left\langle \mathcal{F}[\overline{T}_{B\,ij}]\,\mathcal{F}[\overline{T}_{B\,ij}]^{\dagger} \right\rangle \mathcal{F}[\overline{g}_{ij}] + \left\langle \mathcal{F}[\overline{n}_{ij}]\,\mathcal{F}[\overline{n}_{ij}]^{\dagger} \right\rangle\right)^{-1} \\
&= \overline{\overline{S}}_{T_B T_B\,uv}\, \overline{\overline{G}}_{uv} \left(\overline{\overline{G}}^{\dagger}_{uv}\, \overline{\overline{S}}_{T_B T_B\,uv}\, \overline{\overline{G}}_{uv} + \overline{\overline{S}}_{nn\,uv}\right)^{-1} \qquad (31)
\end{aligned}
$$

where $\overline{\overline{G}}_{uv}$ is the transform of the gain matrix $\overline{g}_{ij}$, $\overline{\overline{S}}_{T_B T_B\,uv}$ is the multidimensional power spectral density matrix for the brightness temperature vector $\overline{T}_B$, $\overline{\overline{S}}_{nn\,uv}$ is the multidimensional power spectral density matrix for the observation noise vector $\overline{n}$, and † is the Hermitian transpose. Since $\overline{n}$ is white, we have:

$$
\overline{\overline{S}}_{nn\,uv} = \mathcal{F}[\overline{\overline{R}}_{nn\,ij}] = \frac{1}{i_{\max} j_{\max}} \begin{bmatrix} \sigma^2_{T1} & 0 & & \\ 0 & \sigma^2_{T2} & & \\ & & \ddots & \\ & & & \sigma^2_{TN} \end{bmatrix} \qquad (32)
$$

which is identical for all spatial frequencies u, v. The second-to-last step in Eq. 31 uses the statistical independence of the brightness process $\overline{T}_B$ and observation noise $\overline{n}$. Note that $\overline{\overline{S}}_{T_B T_B\,uv}$ contains all information on both the spatial and intrachannel spectral statistics of the random brightness process. Here, the use of the multidimensional power spectral density matrix implicitly assumes that the brightness random process is wide-sense stationary. This is a slightly less restrictive assumption than the ergodic assumption used in the KL analysis.

Thus, the optimal linear deconvolution becomes:

$$
\hat{\overline{T}}_{B\,uv} = \overline{\overline{D}}_{uv}\, \mathcal{F}[\overline{T}_{A\,ij}] \qquad (33)
$$

with

$$
\hat{\overline{T}}_{B\,ij} = \mathcal{F}^{-1}[\hat{\overline{T}}_{B\,uv}] \qquad (34)
$$

where $\mathcal{F}^{-1}$is the two-dimensional discrete inverse Fourier transform. This is equivalent to Eq. 27, except written in the spectral domain. Defining the MSD error to be:

$$
\overline{e}_{ij} = \hat{\overline{T}}_{B\,ij} - \overline{T}_{B\,ij} \qquad (35)
$$

The associated MSD spectral error covariance is [31]:

$$
\overline{\overline{S}}_{EE\,uv} = \mathcal{F}[\overline{\overline{R}}_{ee\,ij}] = \overline{\overline{S}}_{T_B T_B\,uv} - \overline{\overline{S}}_{T_B T_B\,uv}\, \overline{\overline{G}}_{uv} \left(\overline{\overline{G}}^{\dagger}_{uv}\, \overline{\overline{S}}_{T_B T_B\,uv}\, \overline{\overline{G}}_{uv} + \overline{\overline{S}}_{nn\,uv}\right)^{-1} \overline{\overline{G}}^{\dagger}_{uv}\, \overline{\overline{S}}_{T_B T_B\,uv} \qquad (36)
$$

Note that this error is always less than the *a-priori* power spectral density for $\overline{T}_B$, illustrating that the optimal deconvolution operator can only reduce the error spectral density. The spectral

domain MSD operator uses spatial information from the highest resolution channels to improve the deconvolution of the lower resolution channels. Such improvements are possible to the extent that the brightnesses between the low frequency and high frequency channels exhibit known correlations [32, 33, 34]. These correlations can be due to either horizontal rain cell structure or spectral scattering or absorption similarities.

The effects of antenna gain uncertainties are manifested as additional non-white observation noise. To see this, consider the gain matrix to be randomly perturbed by a random gain error $\overline{\overline{\delta g}}$:

$$\overline{\overline{g}}_{ij} = \overline{\overline{g}}^{o}_{ij} + \overline{\overline{\delta g}}_{ij} \tag{37}$$

where $\overline{\overline{g}}^{o}$ is the assumed gain matrix from (for example, from Eq. 7). The observed antenna temperature imagery now becomes:

$$\begin{aligned} \overline{T}_{A\,ij} &= \overline{\overline{g}}^{o}_{-i,-j} \ast\ast \overline{T}_{B\,ij} + \overline{\overline{\delta g}}_{-i,-j} \ast\ast \overline{T}_{B\,ij} + \overline{n}_{ij} \\ &= \overline{\overline{g}}^{o}_{-i,-j} \ast\ast \overline{T}_{B\,ij} + \overline{n}'_{ij} \end{aligned} \tag{38}$$

where $\overline{n}'$ includes contributions from both radiometric integration noise and gain pattern uncertainties. The noise covariance matrix for $\overline{n}'$ becomes:

$$\overline{\overline{R}}_{n'n'\,ij} = \langle \overline{n}'_{i'j'}\, \overline{n}'^{\,i'-i,\,j'-j'} \rangle = \overline{\overline{R}}_{nn\,ij} + \langle (\overline{\overline{\delta g}}_{-i',-j'} \ast\ast \overline{T}_{B\,i'j'})(\overline{T}^{\dagger}_{B\,i'-i,j'-j} \ast\ast \overline{\overline{\delta g}}^{\dagger}_{i-i',j-j'}) \rangle \tag{39}$$

$$= \begin{bmatrix} \sigma^2_{T1} & 0 & & \\ 0 & \sigma^2_{T2} & & \\ & & \ddots & \\ & & & \sigma^2_{TN} \end{bmatrix} \delta_i \delta_j + \langle \overline{\overline{\delta g}}_{-i,-j} \ast\ast (\overline{\overline{R}}_{T_B T_B\,ij} + \overline{T}^{(ca)}_{B}\, \overline{T}^{(ca)\,t}_{B}) \ast\ast \overline{\overline{\delta g}}^{\dagger}_{ij} \rangle \tag{40}$$

where the integration noise is assumed to be uncorrelated with the gain uncertainty and the averaging in the second line of Eq. 40 is taken over an ensemble of antenna gain perturbations. In the spectral domain, the corresponding noise power spectral density matrix is:

$$\begin{aligned} \overline{\overline{S}}_{n'n'\,uv} &= \overline{\overline{S}}_{nn\,uv} + \langle \overline{\overline{\delta G}}^{\dagger}_{uv}\, \overline{\overline{S}}_{T_B T_B\,uv}\, \overline{\overline{\delta G}}_{uv} \rangle + \langle \overline{\overline{\delta G}}^{\dagger}_{00}\, \overline{T}^{(ca)}_{B}\, \overline{T}^{(ca)\,t}_{B}\, \overline{\overline{\delta G}}_{00} \rangle\, \delta_u\, \delta_v \\ &= \overline{\overline{S}}_{nn\,uv} + \langle (\overline{\overline{\delta G}}^{\dagger}_{uv}\, \overline{\overline{S}}^{1/2}_{T_B T_B\,uv})(\overline{\overline{\delta G}}_{uv}\, \overline{\overline{S}}^{1/2}_{T_B T_B\,uv}) \rangle + \langle (\overline{\overline{\delta G}}^{\dagger}_{00}\, \overline{T}^{(ca)}_{B})(\overline{T}^{(ca)\,t}_{B}\, \overline{\overline{\delta G}}_{00}) \rangle\, \delta_u\, \delta_v \\ &\triangleq \overline{\overline{S}}_{nn\,uv} + \overline{\overline{S}}_{\overline{\overline{\delta G}}_{uv}\, \overline{\overline{S}}^{1/2}_{T_B T_B\,uv}} + \overline{\overline{S}}_{\overline{\overline{\delta G}}_{00}\, \overline{T}^{(ca)}_{B}} \end{aligned} \tag{41}$$

where the matrix $\overline{\overline{S}}^{1/2}_{T_B T_B\,uv}$ is Hermitian square root of the brightness power spectral density $\overline{\overline{S}}_{T_B T_B\,uv}$:

$$\overline{\overline{S}}_{T_B T_B\,uv} = \overline{\overline{S}}^{1/2\,\dagger}_{T_B T_B\,uv}\, \overline{\overline{S}}^{1/2}_{T_B T_B\,uv} \tag{42}$$

The first term in Eq. 41 is the flat receiver noise power density spectrum (Eq. 32). The second term describes additional noise caused by brightness fluctuations due to clouds and raincells as well as surface features such as shorelines, small islands and ice floes. This portion of the noise spectrum is a low pass process, but is assumed to be zero mean so that it provides virtually no contribution at zero spatial frequency ($u = 0, v = 0$). The third term describes uncertainty in the offsets of the multispectral imagery caused by uncalibrated spillover of the antenna beam into cold space. This is a zero-frequency or DC contribution to the noise power spectrum.

Presumably, most gain perturbations would be caused by deformations in the reflector and/or supporting structure, and hence would affect all channels in a correlated manner. Moreover, the gain perturbations within any given channel are not expected to be independent over all pixel values i and j. Rather, whole sidelobes encompassing many pixels might increase and decrease simultaneously. Thus, the matrices developed in Eqs. 40 and 41 cannot be considered to be diagonal, nor can $\overline{n}'$ be considered to be uncorrelated among pixels.

Using Eqs. 36 and 41, the effects of antenna gain errors caused by both structural perturbations and uncalibrated spillover can be analyzed for their effects on the optimum deconvolved brightness maps. However, to examine their effects on the retrieved precipitation parameters, the end-to-end retrieval problem simulation outlined in the next section must be considered.

The MSD operator can also be developed as an optimal linear estimator in the spatial domain:

$$\hat{\overline{T}}_B = \overline{\overline{D}}' \overline{T}_A \tag{43}$$

where $\overline{T}_A$ is a vector consisting of all pixels from all channels having any significant correlations with the brightness at the location of interest. The determination matrix $\overline{\overline{D}}'$ is given by:

$$\overline{\overline{D}}' = \overline{\overline{R}}_{T_B T_A} (\overline{\overline{R}}_{T_A T_A} + \overline{\overline{R}}_{nn})^{-1} \tag{44}$$

$\overline{\overline{R}}_{\alpha\beta}$ is the joint spatial-spectral covariance matrix between the multispectral vector signals α and β. It is noted, however, that this method results in particularly large determination matrices. An advantage is that the brightness imagery need not considered to be stationary, that is, the statistics can be allowed to vary from point to point within the image. This would be useful for analysis of imagery observed near boundaries such as coastlines, fronts or image edges.

Currently, demonstrations of the spectral and spatial domain MSD operators using the GCE data are being constructed. Of particular interest will be the effect of the noise-resolution tradeoff first described by Backus and Gilbert [35]. Indeed, as the resolution ΔR of the deconvolved map is reduced, the noise at each deconvolved pixel increases. Note that this tradeoff will be inconsequential for area-averaged linear parameter retrievals since the noise is averaged out over the image again in the end. However, for non-linear retrievals, there may be some optimal

deconvolution grid spacing for a given system. The high resolution brightness maps and the intermediate MSD step will allow this search to be performed.

6. Precipitation Retrieval Simulation

This component of the PMMRS will demonstrate simulated precipitation retrieval algorithms for multispectral low-pass filtered microwave imagery. Initial retrievals of precipitation will use the single-step nonlinear statistical technique demonstrated in [23]. This technique is based on a non-linear mapping of the Karhunen-Loève image data $\overline{k}_{A\,ij}$ to various meteorological parameters, for example, surface rain rate, integrated water content, integrated ice content and mean ice particle size. The non-linear mapping is used to estimate a value for each of these parameters at each pixel.

It is expected that more accurate retrieval methods will employ a statistical iterative technique. This scheme has proved to be useful in retrieving relative humidity profiles [36, 37]. A statistical iterative retrieval technique based on the incrementally linear relationship between small changes in brightness temperature and small changes in surface precipitation rate (via the forward raditive transfer process) is planned for implementation in the PMMRS [38]. This technique is similar to the linear spectral domain MSD technique except that $\overline{\overline{D}}_{uv}$ becomes an incremental predictor matrix, $\mathcal{D}\overline{\overline{D}}_{uv}$, and $\delta\overline{T}_{B\,uv}$ and δR_{uv} (where $\delta R = \mathcal{F}[\delta r]$ is the incremental change in the rain rate field r_{ij}) replace $\overline{T}_{A\,uv}$ and $\hat{\overline{T}}_{B\,uv}$, respectively, in an iterated linear statistical operator. This relationship, similar to (Eq. 43) is given by

$$\delta R_{uv} = \mathcal{D}\overline{\overline{D}}\,\delta\overline{T}_{A\,uv} \tag{45}$$

where $\delta\overline{T}_{A\,uv}$ is the error between the observed antenna temperature and the computed antenna temperature:

$$\delta\overline{T}_{A\,uv} = \overline{T}_{A\,uv} - \overline{\overline{G}}_{uv}\,\mathcal{F}[\overline{T}_{B\,ij}(r)] \tag{46}$$

In the above, we assume that $\overline{T}_{B\,ij}$ is a known (nonlinear) function of r_{ij}. A requirement is that a quick and accurate method of computing the forward transfer problem be available. This may be based on a piecewise-linear approximation to the forward radiative transfer relationship.

To take full advantage of the spatial resolution available from high-frequency channels, it may seem that multispectral deconvolution of the antenna gain pattern must be first performed. However, the deconvolution aspect of the problem can be integrated into the nonlinear precipitation parameter retrieval using a spectral-domain nonlinear estimator. In these schemes, the effects of antenna pattern errors will be examined by their effect on the modified instrument noise covariance (Eq. 41). Iteration ceases when the $\delta\overline{T}_{A\,uv}$ is zero to within the noise of the sensor, as determined by $\overline{\overline{R}}_{n'n'}$. To reduce the complexity of the calculation, the KL modes can be used.

7. Discussion

At this time, the microphysical cloud and raincell data compilation, forward radiative transfer calculations, sensor observation simulations, and Karhunen-Loève transformation and degree of freedom calculations have been implemented. Although we cannot yet quantify the available retrieval accuracy of candidate systems, the loss in number of observable degrees of freedom as aperture size is reduced is readily seen. The effect of this information loss will be more fully understood upon completion of the end-to-end retrieval simulation. Future implementation of the deconvolution and parameter retrieval components of the PMMRS will improve the ability to determine (quantitatively) the available accuracy of existing and future spaceborne passive microwave meteorological systems and to design optimized sensor-specific multispectral retrieval algorithms.

Acknowledgements-This work has been supported by the Georgia Institute of Technology and NASA grant NAS1-18925. The authors also thank N. Prasad, J. Simpson, and W.K. Tao of the NASA Goddard Space Flight Center for providing the GCE data.

References

[1] Staelin, D.H., "Passive Microwave Techniques for Geophysical Sensing of the Earth from Satellites", *IEEE Trans. Ant. Prop.*, vol. AP-29, no. 4, pp. 683-687, 1981.

[2] Njoku, E.G., "Passive Microwave Remote Sensing of the Earth from Space - A Review", *Proc. IEEE*, vol. 70, pp. 728-749, July 1982.

[3] Gasiewski, A.J., "Microwave Radiative Transfer in Hydrometeors", in Atmospheric Remote Sensing by Microwave Radiometry, M.A. Janssen, (ed.), under contract for publication by John Wiley and Sons, 1992.

[4] Galliano, J.A., and R.H. Platt, "An Imaging Passive Radiometer for Precipitation Retrieval and Mesoscale Storm System Studies", Proceedings of the 1989 International Geoscience and Remote Sensing Symposium (IGARSS), vol. 1, pp. 286-289, presented at the University of British Columbia, Vancouver, B.C., July 10-14, 1989.

[5] Gasiewski, A.J., J.W. Barrett, P.G. Bonanni, and D.H. Staelin, "Aircraft-Based Radiometric Imaging of Tropospheric Temperature Profiles and Precipitation Using the 118.75-GHz Oxygen Resonance", *J. Appl. Meteor.*, vol. 29, no. 7, pp. 620-632, July, 1990.

[6] Staelin, D.H., A.H. Barrett, J.W. Waters, F.T. Barath, E.J. Johnston, P.W. Rosenkranz, N.E. Gaut and W.B. Lenoir, "Microwave Spectrometer on the Nimbus 5 Satellite : Meteorological and Geophysical Data", *Science*, vol. 182, pp. 1339-1341, Dec. 28, 1973.

[7] Njoku, E.G., J.M. Stacey, and F.T. Barath, "The Seasat Multichannel Microwave Radiometer (SMMR): Instrument Description and Performance", *IEEE J. Oceanic Eng.*, vol. OE-5, no. 2., pp. 100-115, April, 1980.

[8] Hollinger, J.P., J.L. Pierce, and G.A. Poe, "SSM/I Instrument Evaluation", *IEEE Trans. Geosci. Remote Sensing*, vol. 28, No. 5, pp. 781-790, Sept., 1990.

[9] Kummerow, C., R.A. Mack, and I.M. Hakkarinen, "A Self-Consistency Approach to Improve Rainfall Rate Estimation from Space", *J. Appl. Meteor.*, vol. 28, no. 9, pp. 869-884, September, 1989.

[10] Tao, W.K., J. Simpson, S. Lang, M. McCumber, R.F. Adler and R. Penc, "An Algorithm to Estimate the Heating Budget from Vertical Hydrometeor Profiles", *J. Appl. Meteor.*, vol. 29, no. 12, pp. 1232-1244, December, 1990.

[11] D.H. Staelin and P.W. Rosenkranz (eds.), "Applications Review Panel: High Resolution Passive Microwave Satellites Final Report", Research Laboratory of Electronics, Massachusetts Institute of Technology, April, 1978.

[12] Stutzman, W.L., and G.S. Brown (eds.), "The Science Benefits of and the Antenna Requirements for Microwave Remote Sensing from Geostationary Orbit", NASA Contractor Report 4408, Prepared by the Virginia Polytechnic and State University, Blacksburg, VA for the NASA Langley Research Center, 1991.

[13] "Geosynchronous Microwave Atmospheric Sounding Radiometer (MASR) Feasibility Studies", Hughes Aircraft Co. final report for contracts NAS 5-24082 and NAS 5-24087, vol. 1 (Management Summary), Hughes ref. no. D8647/D9236, January, 1978.

[14] "Geosynchronous Microwave Precipitation Radiometer - Phase A Study Report", JPL report JPL D-8136, Jan. 1991.

[15] Simpson, J., R.F. Adler, and G.R. North, "A Proposed Tropical Rainfall Measuring Mission (TRMM) Satellite", *Bull. Amer. Meteor. Soc.*, vol 69, no. 3, pp. 278-295, 1988.

[16] EOS Reference Handbook, D.Dokken (ed.), NASA Goddard Space Flight Center, Publication NP-144, May 1991.

[17] Wilson, W.J., personal communication.

[18] Le Vine, D.M., M. Kao, A.B. Tanner, C.T. Swift, and A. Griffis, "Initial Results in the Development of a Synthetic Aperture Radiometer", *IEEE Trans. Geosci. Remote Sensing*, vol. 28, no. 4, pp. 614-619, July 1990.

[19] Jackson, T.J. and T.J. Schmugge, "Passive Microwave Remote Sensing System for Soil Moisture Research: Some supporting Research", *IEEE Trans. Geosci. Remote Sensing*, vol. 27, no. 2, pp. 225-235, March 1989.

[20] Wilheit, T.T., A.T.C. Chang, M.S.V. Rao, E.B. Rodgers, and J.S. Theon, "A Satellite Technique for Quantitatively Mapping Rainfall Rates over the Oceans", *J. Appl. Meteor.*, vol. 16, no. 5, pp. 551-560, 1977.

[21] Gasiewski, A.J. and Staelin, D.H., "Science Requirements for Passive Microwave Sensors on Earth Science Geostationary Platforms", Proceedings of the NASA Technology Workshop for Earth Science Geostationary Platforms, NASA Conference Publication 3040, presented at the NASA Langley Research Center, Hampton, VA., September 21-22, 1988. pp. 37-53, 1988.

[22] Tao, W.K., and J. Simpson, "Modelling Study of a Tropical Squall-Type Convective Line", *J. Atm. Sci.*, vol. 46, no. 2, pp. 177-202, Jan. 15, 1989.

[23] Gasiewski, A.J., and D.H. Staelin, "Statistical Precipitation Cell Parameter Estimation Using Passive 118-GHz O_2 Observations", *J. Geophys. Res.*, vol. 94, no. D15, pp. 18367-18378, December, 1989.

[24] Smith, P.L., Equivalent Radar Reflectivity Factors for Snow and Ice Particles, *J. Cli. Appl. Met.*, *23*, 1258, 1984.

[25] Gasiewski, A.J., and D.H. Staelin, "Numerical Modelling of Passive Microwave O_2 Observations Over Precipitation", *Radio Sci.*, vol. 25, no. 3, pp. 217-235, 1990.

[26] Silver, S. (ed.), Microwave Antenna Theory and Design, London: Peter Perigrinus, Ltd., 1984.

[27] Kraus, J.D., Radioastronomy, 2nd ed., Cygnus-Quasar Books: Powell OH, 1986.

[28] Ruf, C.S., C.T. Swift, A.B. Tanner and D.M. Le Vine, "Interferometric Synthetic Aperture Microwave Radiometry for the Remote Sensing of the Earth", *IEEE Trans. Geosci. Remote Sensing*, vol. 26, no. 5, pp. 598-612, Sept., 1988.

[29] Gonzalez, R.C., and P.A. Wintz, Digital Image Processing, 2nd ed., Addison-Wesley Publishing Co., Reading MA, 1987.

[30] Ready, P.J., and P.A. Wintz, "Information Extraction, SNR Improvement, and Data Compression in Multispectral Imagery", *IEEE Trans. Comm.*, vol. COM-21, no. 10, pp. 1123-1130, 1973.

[31] Rosenkranz, P.W., "Inversion of Data from Diffraction-Limited Multiwavelength Remote Sensors, 1, Linear Case," *Radio Science*, vol. 13, no. 6, pp. 1003-1010, Nov.-Dec., 1978.

[32] Poe, G.A., "Optimum Interpolation of Imaging Microwave Radiometer Data", *IEEE Trans. Geosci. Remote Sensing*, vol. 28, no. 5, pp. 800-810, Sept., 1990.

[33] Farar, M.R., and E.A. Smith, "Spatial Resolution Enhancement of Terrestrial Features Using Deconvolved SSM/I Microwave Brightness Temperatures", *IEEE Trans. Geosci. Remote Sensing*, vol. 30, no. 2, pp. 349-355, March 1992.

[34] Robinson, W.D., C. Kummerow, and W.S. Olson, "A Technique for Enhancing and Matching the Resolution of Microwave Measurements from the SSM/I Instrument", *IEEE Trans. Geosci. Remote Sensing*, vol. 30, no. 3, pp. 419-429, May 1992.

[35] Backus, G., and F. Gilbert, "Uniqueness in the Inversion of Inaccurate Gross Earth Data", *Phil. Trans. Roy. Soc. London*, vol. A266, pp. 123-192, 1970.

[36] Kuo, C.C., "Statistical Iterative Scheme for Estimating Atmospheric Relative Humidity Profiles from Microwave Radiometric Measurements" S.M. thesis, Department of Electrical Engineering and Computer Science, Massachusetts Institute of Technology, Cambridge, MA., Dec., 1988.

[37] Kuo, C.C., and D.H. Staelin, "Statistical Iterative Scheme for Estimating Atmospheric Relative Humidity Profiles", submitted to *IEEE Trans. Geosci. Remote Sensing*, Sept., 1990.

[38] Schaerer, G. and T.T. Wilheit, "A Passive Microwave Technique for Profiling of Atmospheric Water Vapor", *Radio Science*, vol. 14, no. 3, pp. 371-375, May-June 1979.

Table 1: Catalogue of synthesized brightness imagery used in the numerical simulations.

Brightness Map Set	# Channels	Horizontal Resolution ΔR (km)	Image Size (km)	Comments
GCE 1	30	1.5	96x96	Tao & Simpson GCE data, t = 126 min
GCE 2	30	1.5	96x96	Tao & Simpson GCE data, t = 138 min
GCE 3	30	1.5	96x96	Tao & Simpson GCE data, t = 174 min
GCE 4	30	1.5	96x96	Tao & Simpson GCE data, t = 210 min
GCE 5	30	1.5	96x96	Tao & Simpson GCE data, t = 234 min
CP-2	9	1.0	41x41	COHMEX CP-2 data, July 11, 1986 (window channels only)

Table 2: Scaling factor $\alpha(p)$ and aperture efficiencies for various aperture taper parameters p.

p	α	Aperture Efficiency η_A (%)
0	1.02	100
1	1.27	75
2	1.47	56
3	1.65	44
4	1.81	36

Table 3: System sensitivity parameters for the MIMR simulations. The integration time is based on the single-spot integration time for sampling at the Nyquist resolution of the highest frequency channel.

Channel #	Frequency (GHz)	Bandwidth (MHz)	T_{sys} (K)	Integration Time (msec)	σ_{SSn} (K)	σ_{Tn} (K)
MIMR: six channels, D = 1.6 m, R_S = 0.74 km, $R_{3\text{-dB,N}}$ = 1.89 km						
1	6.00	20	250	0.030	0.32	0.16
2	10.69	20	350		0.45	0.22
3	18.70	200	400		0.16	0.079
4	23.80	400	400		0.12	0.059
5	36.50	1000	500		0.10	0.049
6	89.00	6000	650		0.05	0.024
MIMR: six channels, D = 4.4 m, R_S = 0.27 km, $R_{3\text{-dB,N}}$ = 0.69 km						
1	6.00	20	250	0.0039	0.88	0.16
2	10.69	20	350		1.23	0.22
3	18.70	200	400		0.44	0.079
4	23.80	400	400		0.33	0.059
5	36.50	1000	500		0.27	0.049
6	89.00	6000	650		0.14	0.024

Table 4: System sensitivity parameters for the LSA simulations. The integration time is based on the single-spot integration time for sampling at the Nyquist resolution of the highest frequency channel.

Channel #	Frequency (GHz)	Bandwidth (MHz)	T_{sys} (K)	Integration Time (msec)	σ_{SS_n} (K)	σ_{T_n} (K)
LSA: nine channels, D = 15 m, R_S = 0.88 km, $R_{3\text{-dB,N}}$ = 2.22 km						
1	6.00	20	250	1.2	1.63	0.95
2	10.69	20	350		2.29	1.33
3	18.70	200	400		0.83	0.48
4	36.50	1000	500		0.46	0.27
5	89.00	6000	650		0.24	0.14
6	166.00	4000	1000		0.46	0.27
7	220.00	3000	2000		1.07	0.62
8	340.00	3000	3000		1.60	0.93
9	410.00	3000	5000		2.67	1.56
LSA: nine channels, D = 40 m, R_S = 0.33 km, $R_{3\text{-dB,N}}$ = 0.83 km						
1	6.00	20	250	0.16	4.34	0.95
2	10.69	20	350		6.10	1.33
3	18.70	200	400		2.21	0.48
4	36.50	1000	500		1.22	0.27
5	89.00	6000	650		0.64	0.14
6	166.00	4000	1000		1.22	0.27
7	220.00	3000	2000		2.85	0.62
8	340.00	3000	3000		4.26	0.93
9	410.00	3000	5000		7.11	1.56
LSA: eight channels, D = 15 m, R_S = 6.53 km, $R_{3\text{-dB,N}}$ = 16.6 km						
1	18.700	200	400	65.3	0.11	0.48
2	23.800	400	400		0.078	0.34
3	36.500	1000	500		0.062	0.27
4	50.300	180	550		0.16	0.70
5	52.800	400	550		0.11	0.48
6	53.596	170	550		0.16	0.70
7	54.400	400	550		0.11	0.48
8	54.940	400	550		0.11	0.48
LSA: eight channels, D = 40 m, R_S = 2.45 km, $R_{3\text{-dB,N}}$ = 6.22 km						
1	18.700	200	400	9.18	0.29	0.48
2	23.800	400	400		0.21	0.34
3	36.500	1000	500		0.16	0.27
4	50.300	180	550		0.43	0.70
5	52.800	400	550		0.29	0.48
6	53.596	170	550		0.43	0.70
7	54.400	400	550		0.29	0.48
8	54.940	400	550		0.29	0.48

Figure 1: Schematic diagram of the PMMRS.

Figure 2: Computed window-channel brightness maps for three GCE simulations: (a) GCE 2, (b) GCE 3, (c) GCE 4, and for the COHMEX CP-2 data (d). The channel frequencies (in GHz) are indicated.

Figure 3: Computed brightness maps for channels near the microwave oxygen lines for GCE 3. The channel frequencies (in GHz) are indicated.

Figure 4: Computed brightness maps for channels near the microwave water vapor lines for GCE 3. The channel frequencies (in GHz) are indicated.

Figure 5: Scan patterns of canonical (a) geosynchronous and (b) low-Earth orbit imaging systems.

Figure 6: Energy distribution functions for linearly-polarized circular apertures of varying amplitude tapers p, indicating efficiencies at the 3-dB beamwidth (□) and first null (•).

Figure 7: MIMR brightness temperature imagery, as would be observed from low Earth orbit: (a) full resolution, (b,c) after convolution with the gain pattern of a circular 4.4-m and 1.6-m quadratically-tapered aperture distribution, respectively. The 3-dB spot sizes (in km, FWHM) are indicated for each frequency in (b) and (c).

Figure 8: Representative LSA brightness temperature imagery for nine window channels, as would be observed from geosynchronous orbit: (a) full resolution, and (b,c) after convolution with the gain patterns of circular 40-m and 15-m quadratically-tapered aperture field distributions, respectively. The 3-dB spot sizes (in km, FWHM) are indicated for each frequency in (b) and (c).

Figure 9: Representative LSA brightness temperature imagery for eight low-frequency channels, as would be observed from geosynchronous orbit: (a) full resolution, and (b,c) after convolution with the gain patterns of circular 40-m and 15-m quadratically-tapered aperture field distributions, respectively. The 3-dB spot sizes (in km, FWHM) are indicated for each frequency in (b) and (c).

Figure 10: Rank-ordered KL mode imagery for the six-channel MIMR system: (a) full resolution, (b,c) after convolution with the gain pattern of a circular 4.4-m and 1.6-m quadratically-tapered aperture distribution, respectively. The five most dominant modes are shown with the respective SNR's indicated above each image.

Figure 11: Three most dominant rank-ordered eigenvectors for the six-channel MIMR system: (a) full resolution, (b,c) after convolution with the gain pattern of a circular 4.4-m and 1.6-m quadratically-tapered aperture distribution, respectively.

Figure 12: SNR ranking for the full-resolution and convolved MIMR imagery.

Figure 13: Rank-ordered KL mode imagery for the LSA nine-channel GEO system: (a) full resolution, (b,c) after convolution with the gain pattern of a circular 40-m and 15-m quadratically-tapered aperture distribution, respectively. The five most dominant modes are shown with the respective SNR's indicated above each image.

Figure 14: Three most dominant rank-ordered eigenvectors for the nine-channel LSA system: (a) full resolution, (b,c) after convolution with the gain pattern of a circular 40-m and 15-m quadratically-tapered aperture distribution, respectively.

Figure 15: SNR ranking for the full-resolution and convolved nine-channel LSA imagery.

Figure 16: Rank-ordered KL mode imagery for the LSA eight-channel GEO system: (a) full resolution, (b,c) after convolution with the gain pattern of a circular 40-m and 15-m quadratically-tapered aperture distribution, respectively. The five most dominant modes are shown with the respective SNR's indicated above each image.

Figure 17: Three most dominant rank-ordered eigenvectors for the eight-channel LSA system: (a) full resolution, (b,c) after convolution with the gain pattern of a circular 40-m and 15-m quadratically-tapered aperture distribution, respectively.

Figure 18: SNR ranking for the full-resolution and convolved eight-channel LSA imagery.

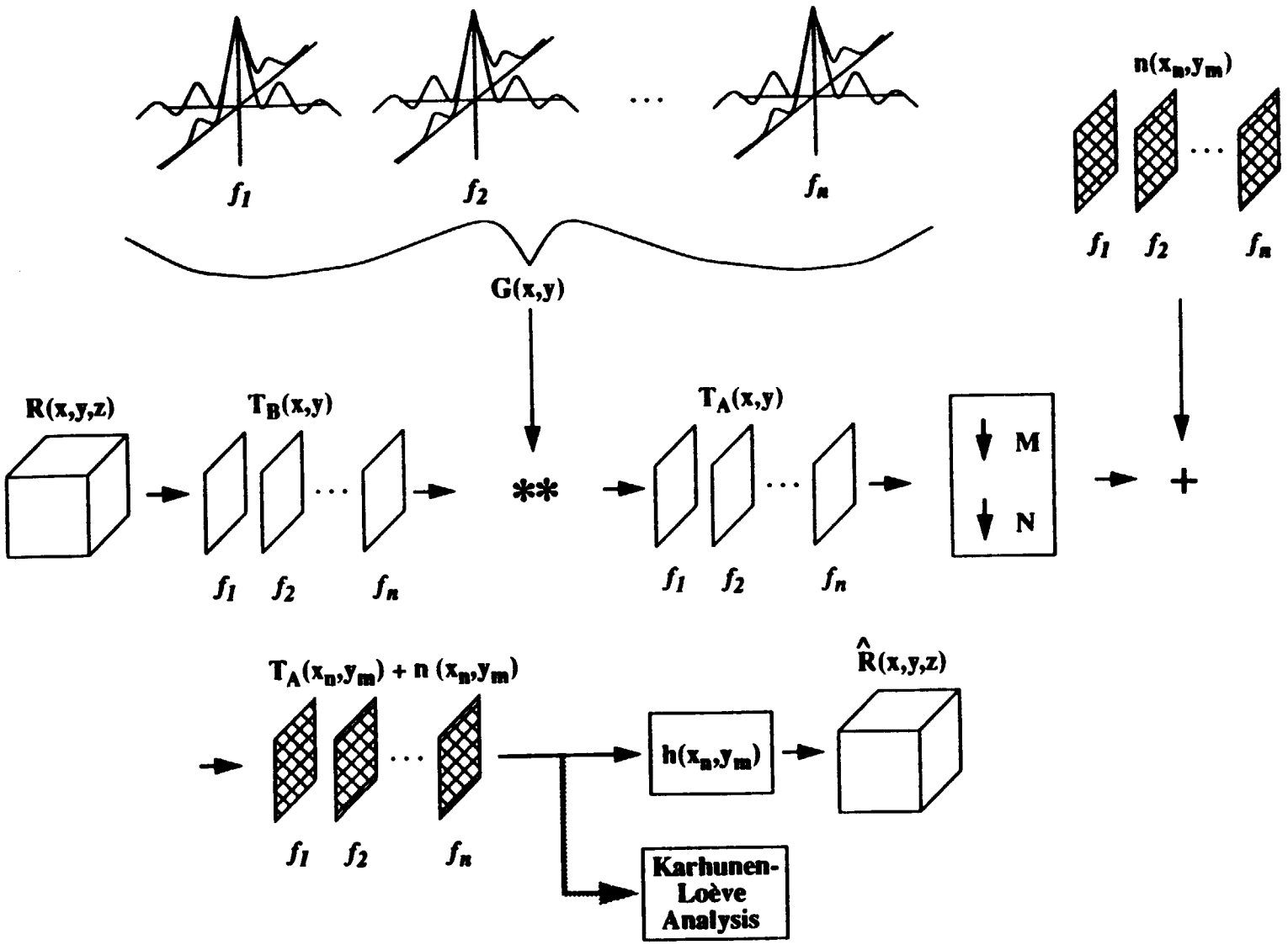

Figure 1: Schematic diagram of the PMMRS.

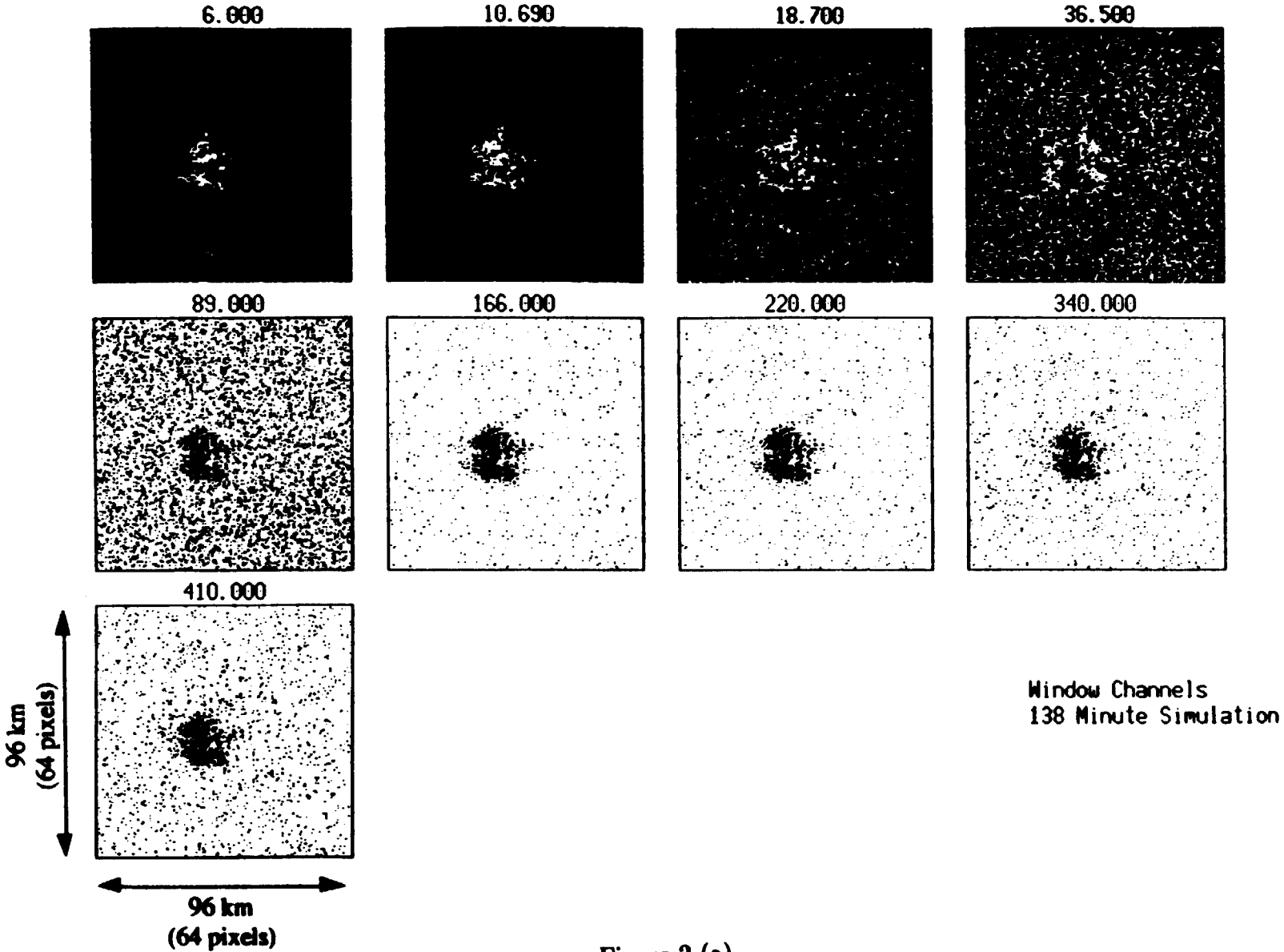

Figure 2 (a)

Figure 2: Computed window-channel brightness maps for three GCE simulations: (a) GCE 2, (b) GCE 3, (c) GCE 4, and for the COHMEX CP-2 data (d). The channel frequencies (in GHz) are indicated.

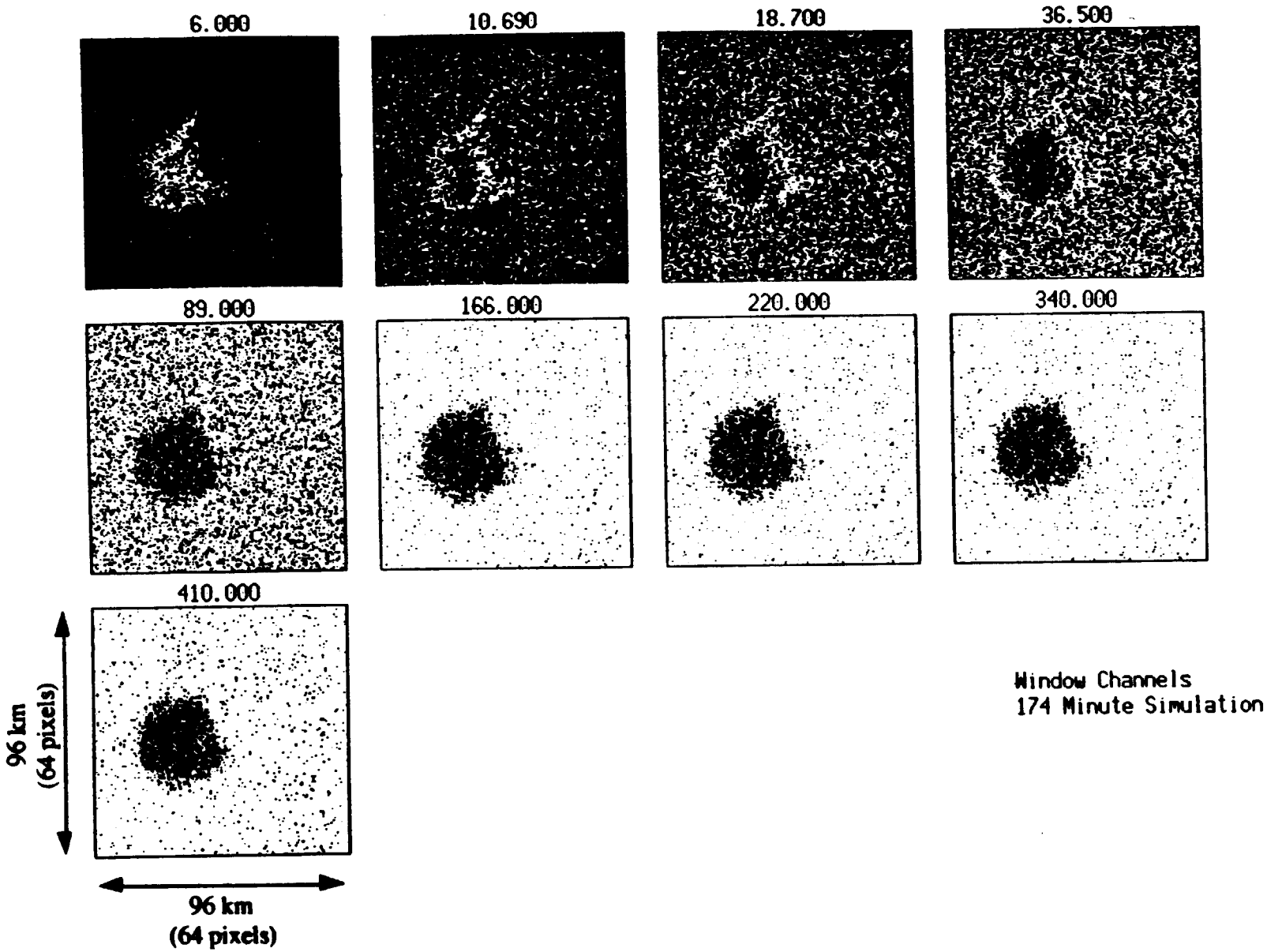
6.000
10.690
18.700
36.500
89.000
166.000
220.000
340.000
410.000
96 km
(64 pixels)
96 km
(64 pixels)
Window Channels
174 Minute Simulation

Figure 2 (b)

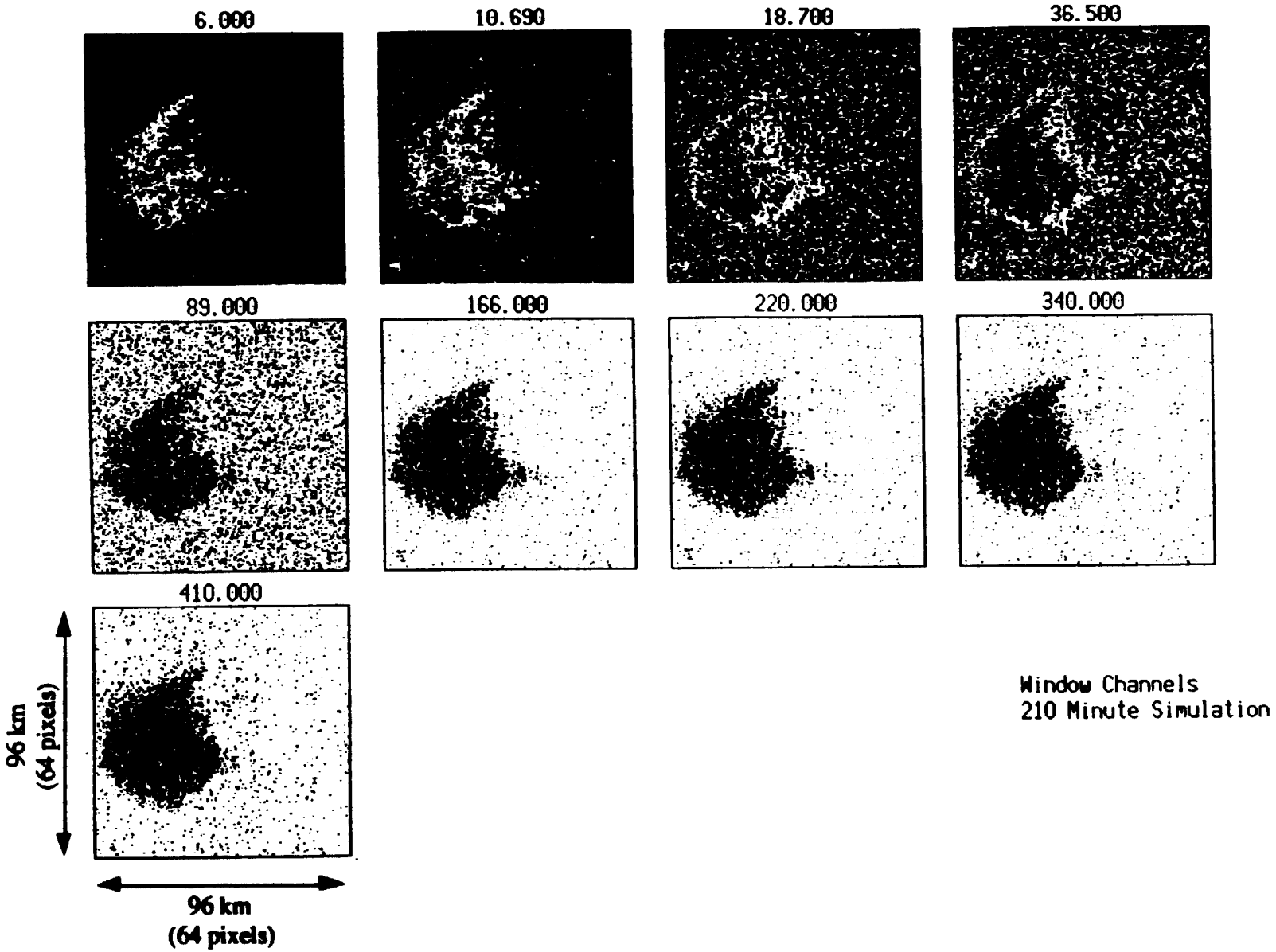
6.000
10.690
18.700
36.500
89.000
166.000
220.000
340.000
410.000
96 km
(64 pixels)
96 km
(64 pixels)
Window Channels
210 Minute Simulation

Figure 2 (c)

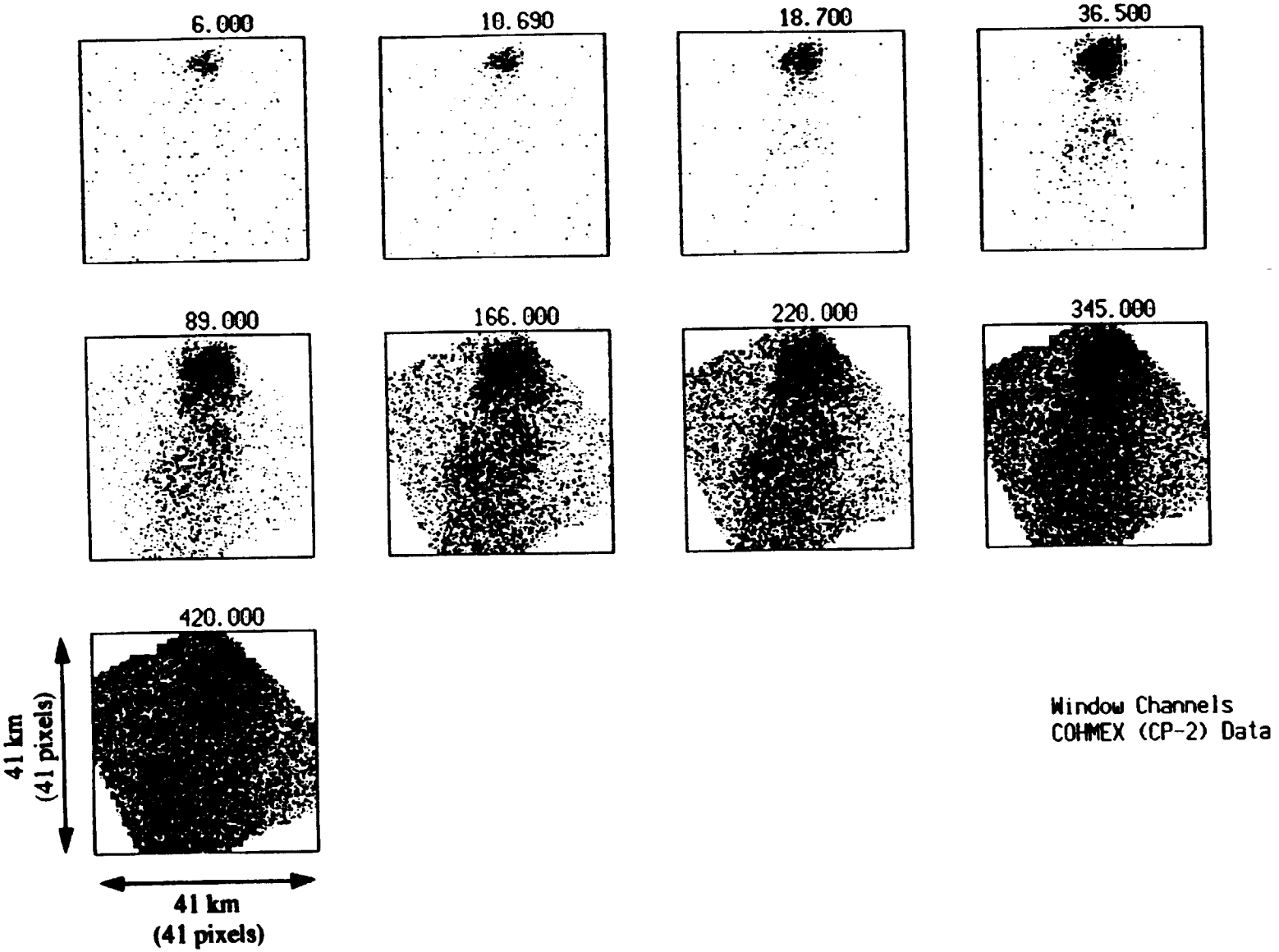
6.000
10.690
18.700
36.500
89.000
166.000
220.000
345.000
420.000
41 km
(41 pixels)
41 km
(41 pixels)
Window Channels
COHMEX (CP-2) Data

Figure 2 (d)

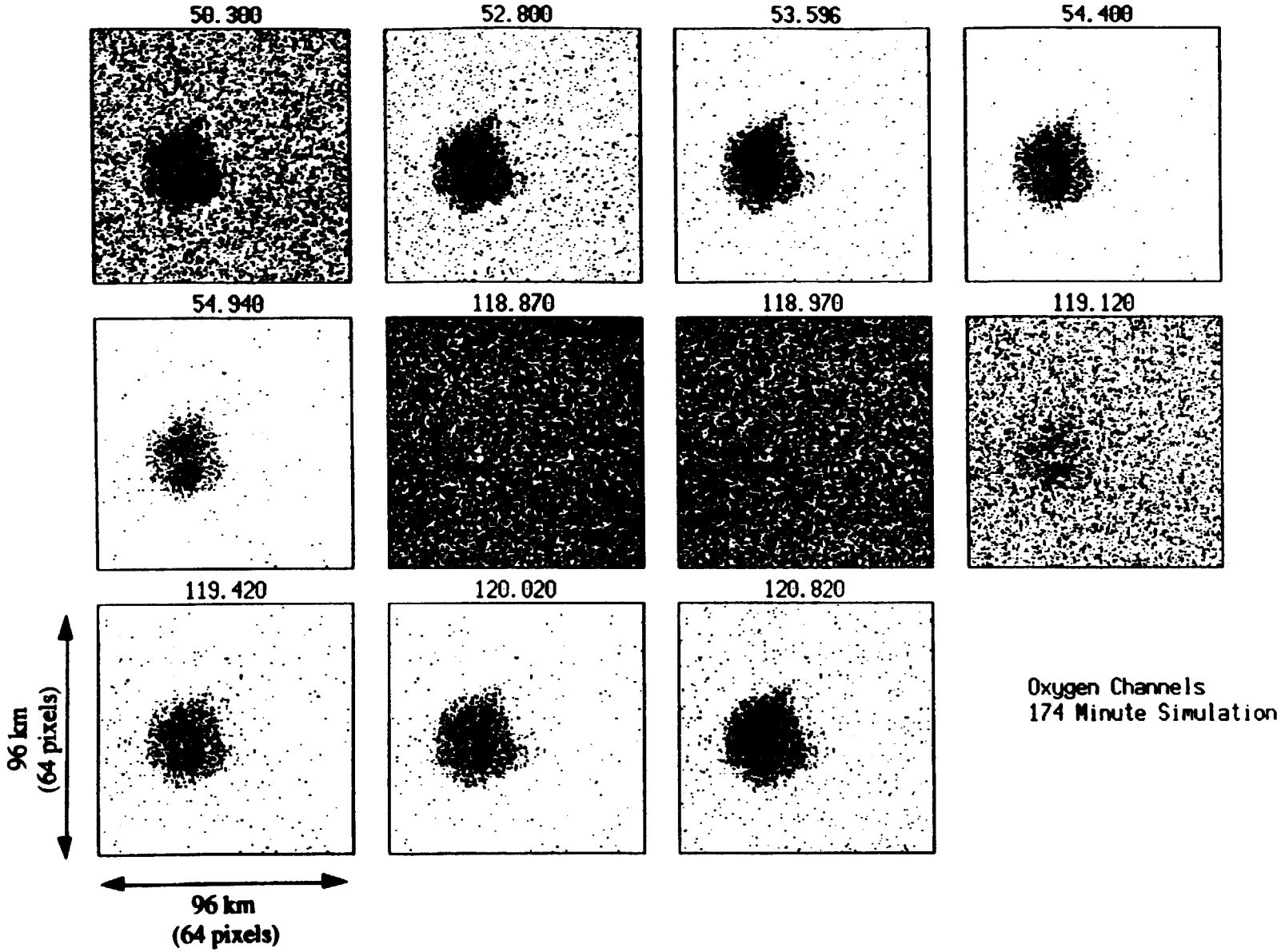

Figure 3: Computed brightness maps for channels near the microwave oxygen lines for GCE 3. The channel frequencies (in GHz) are indicated.

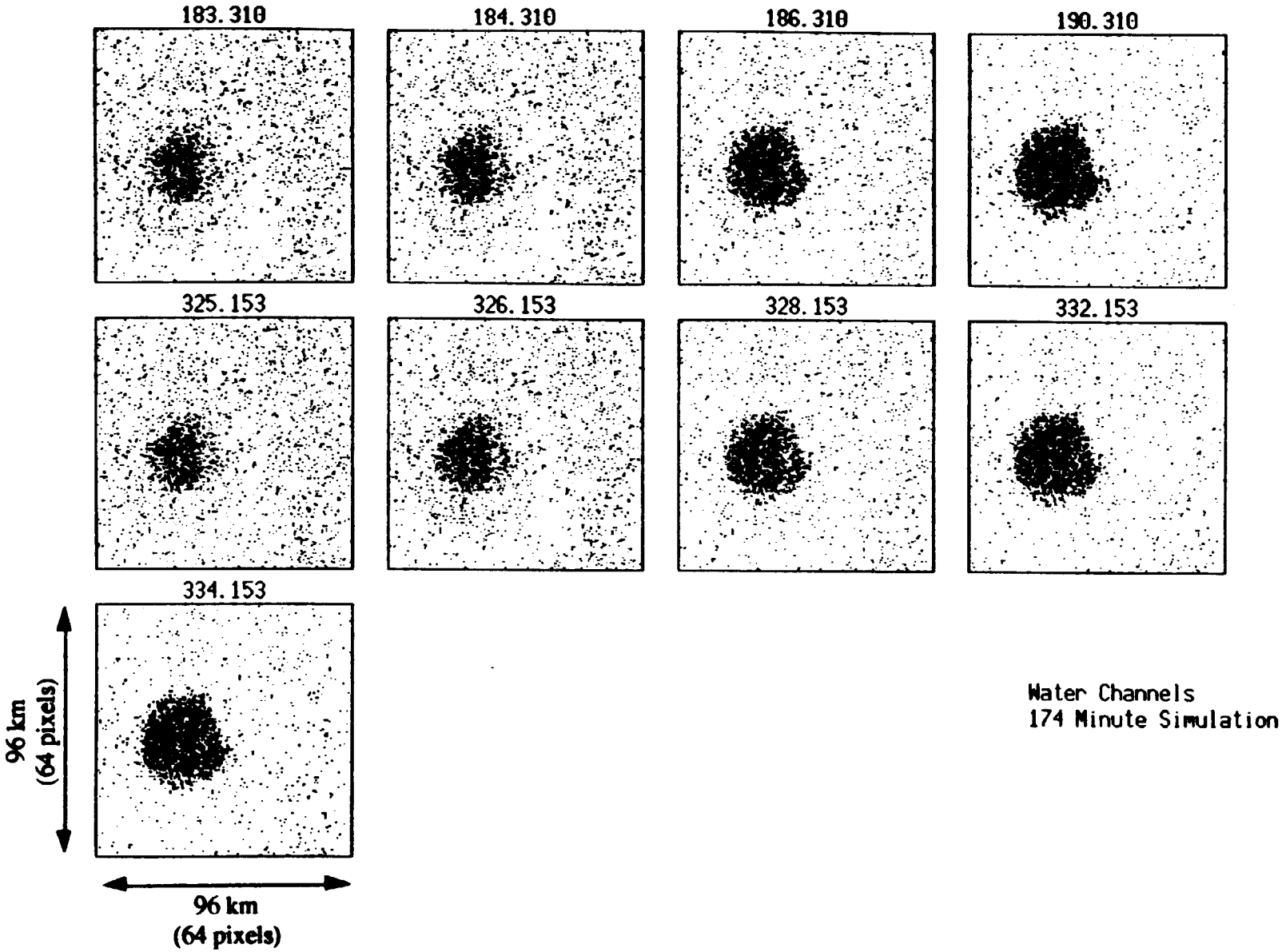

Figure 4: Computed brightness maps for channels near the microwave water vapor lines for GCE 3. The channel frequencies (in GHz) are indicated.

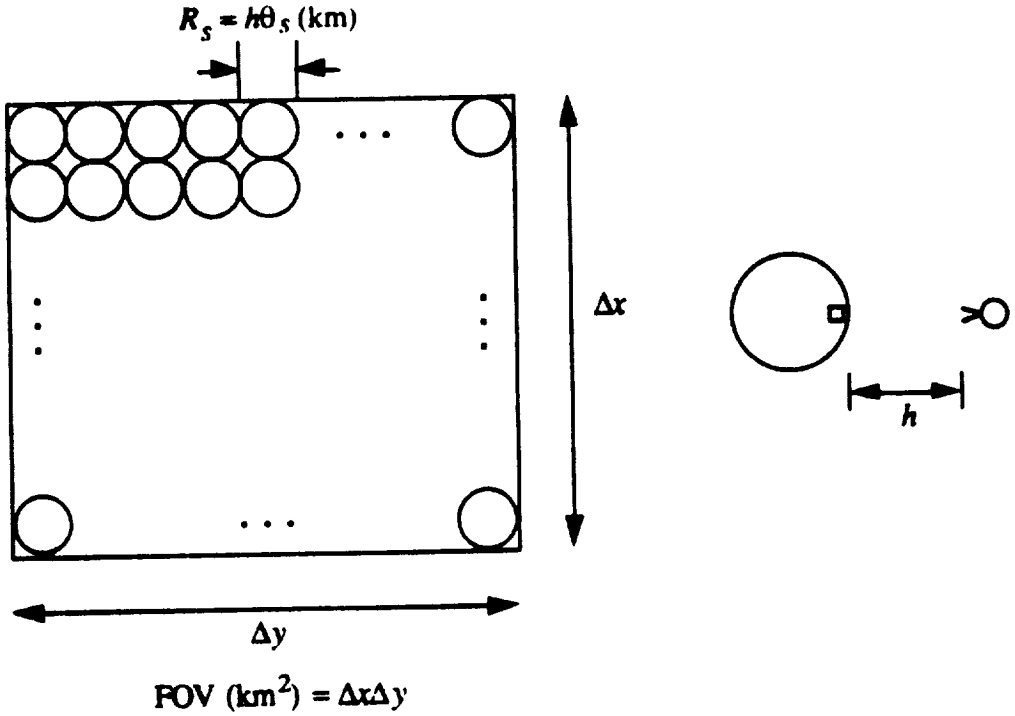

(a)

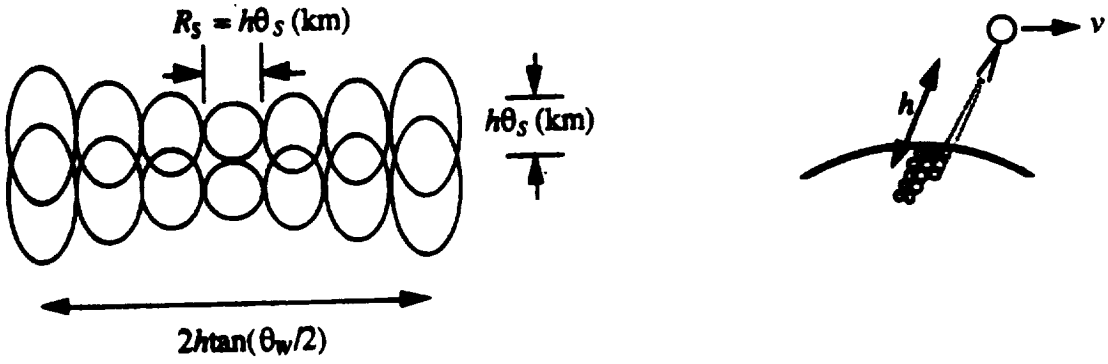

(b)

Figure 5: Scan patterns of canonical (a) geosynchronous and (b) low-Earth orbit imaging systems.

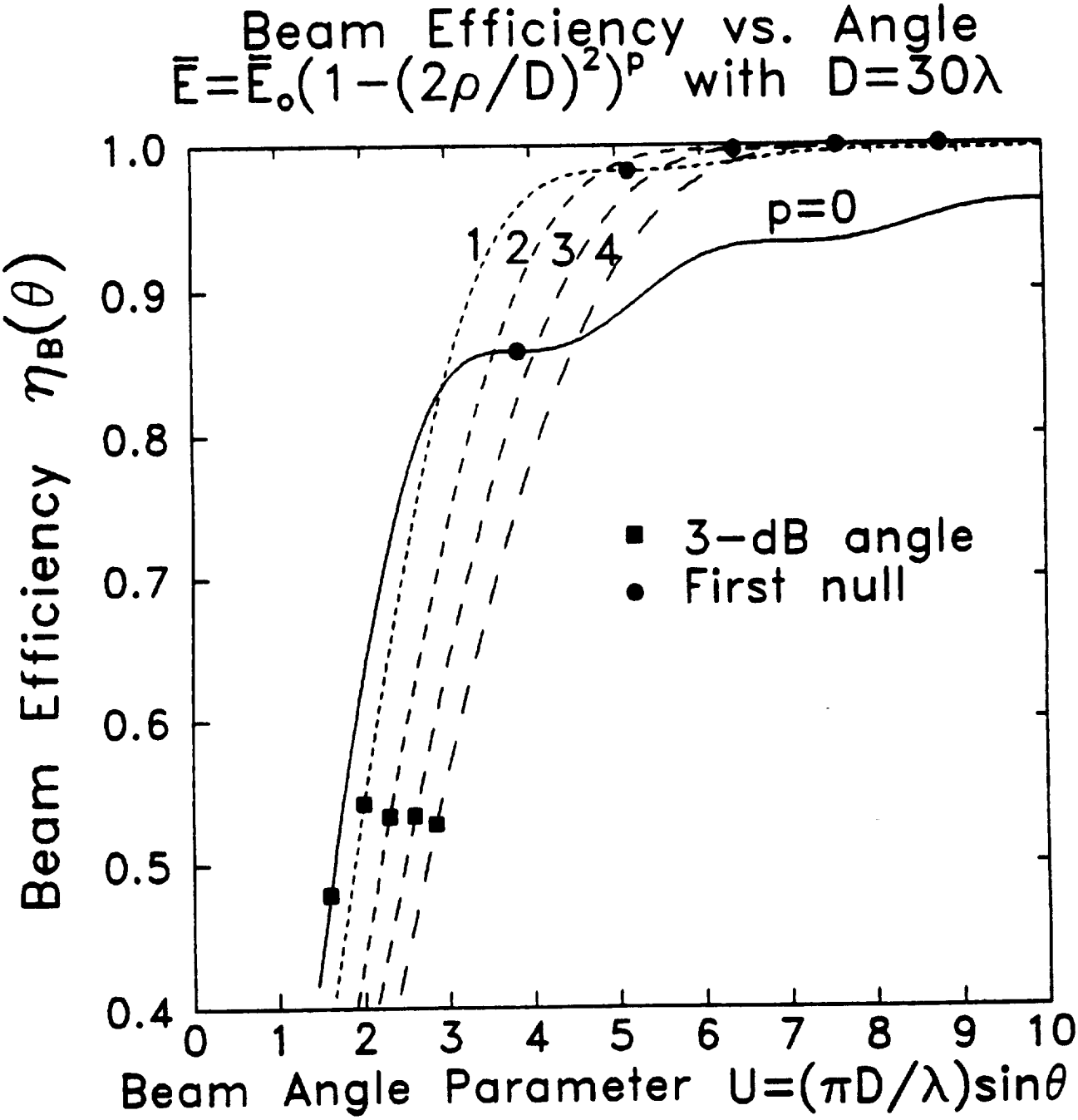

Figure 6: Energy distribution functions for linearly-polarized circular apertures of varying amplitude tapers p, indicating efficiencies at the 3-dB beamwidth (■) and first null (•).

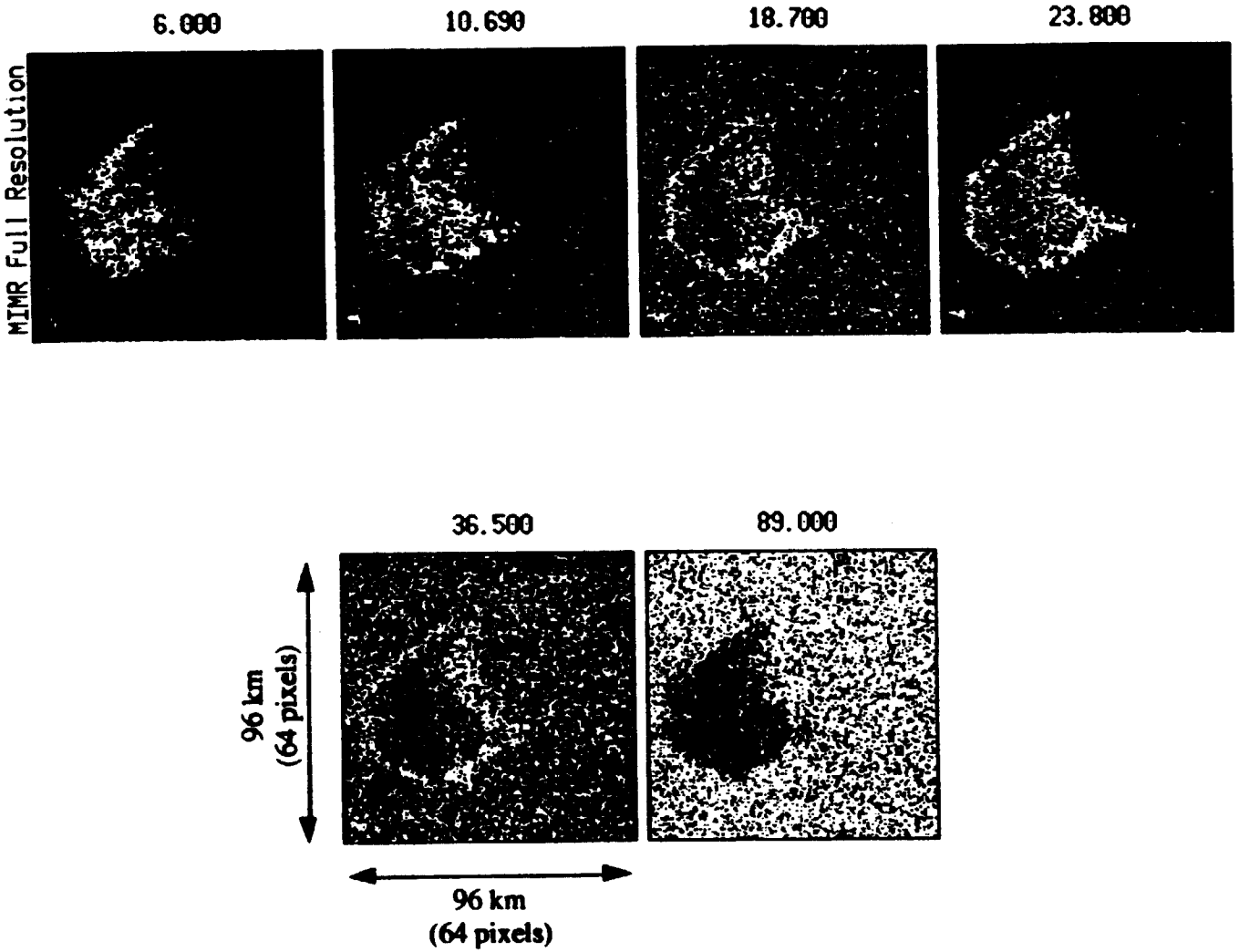

Figure 7 (a)

Figure 7: MIMR brightness temperature imagery, as would be observed from low Earth orbit: (a) full resolution, (b,c) after convolution with the gain pattern of a circular 4.4-m and 1.6-m quadratically-tapered aperture distribution, respectively. The 3-dB spot sizes (in km, FWHM) are indicated for each frequency in (b) and (c).

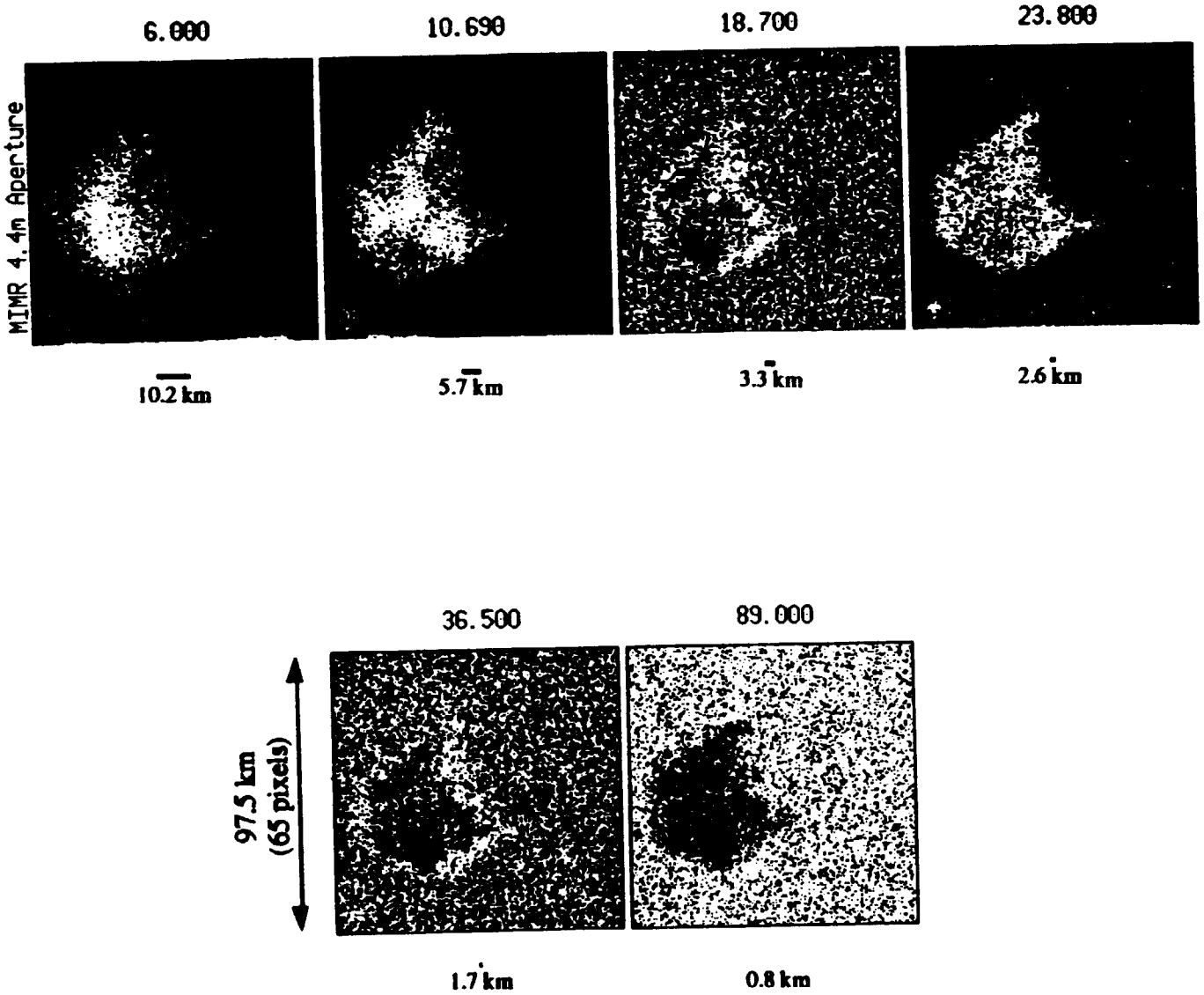
6.000
10.690
18.700
23.800
MIMR 4.4m Aperture
10.2 km
5.7 km
3.3 km
2.6 km
36.500
89.000
97.5 km
(65 pixels)
1.7 km
0.8 km

Figure 7 (b)

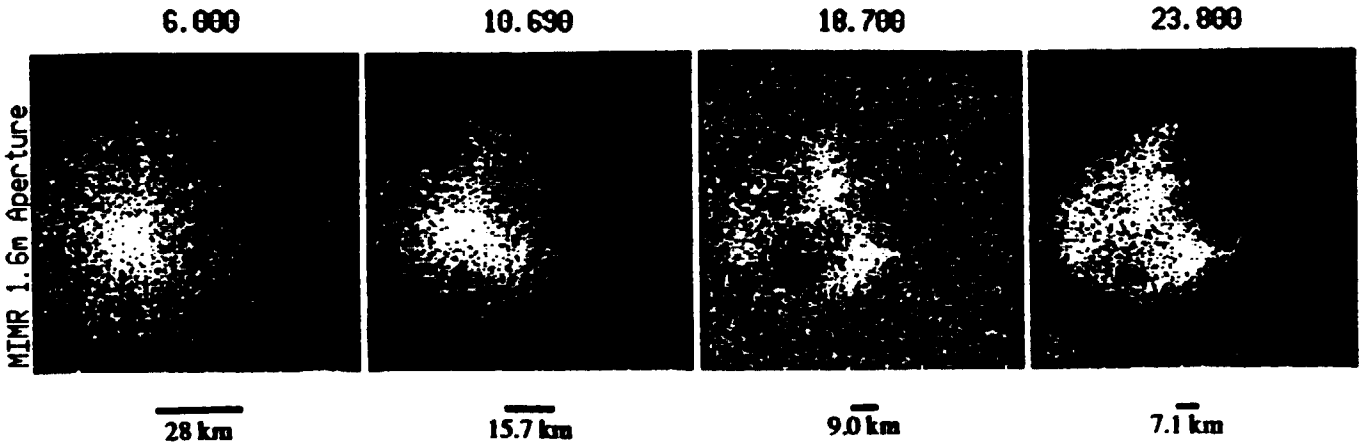
6.000
10.690
18.700
23.800
MIMR 1.6m Aperture
28 km
15.7 km
9.0 km
7.1 km

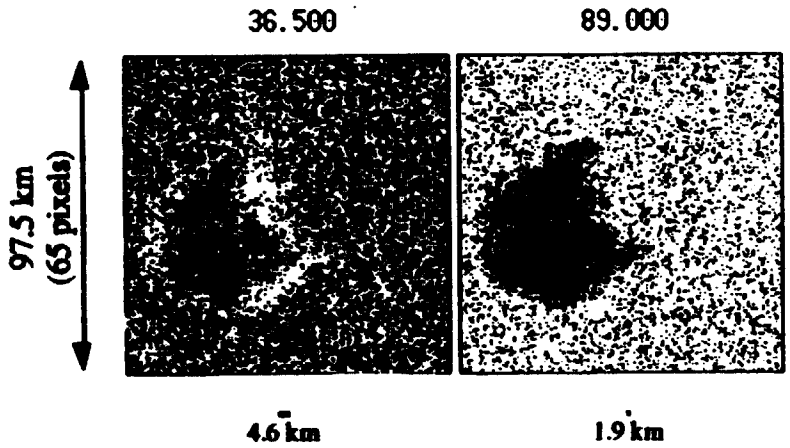
36.500
89.000
97.5 km
(65 pixels)
4.6 km
1.9 km

Figure 7 (c)

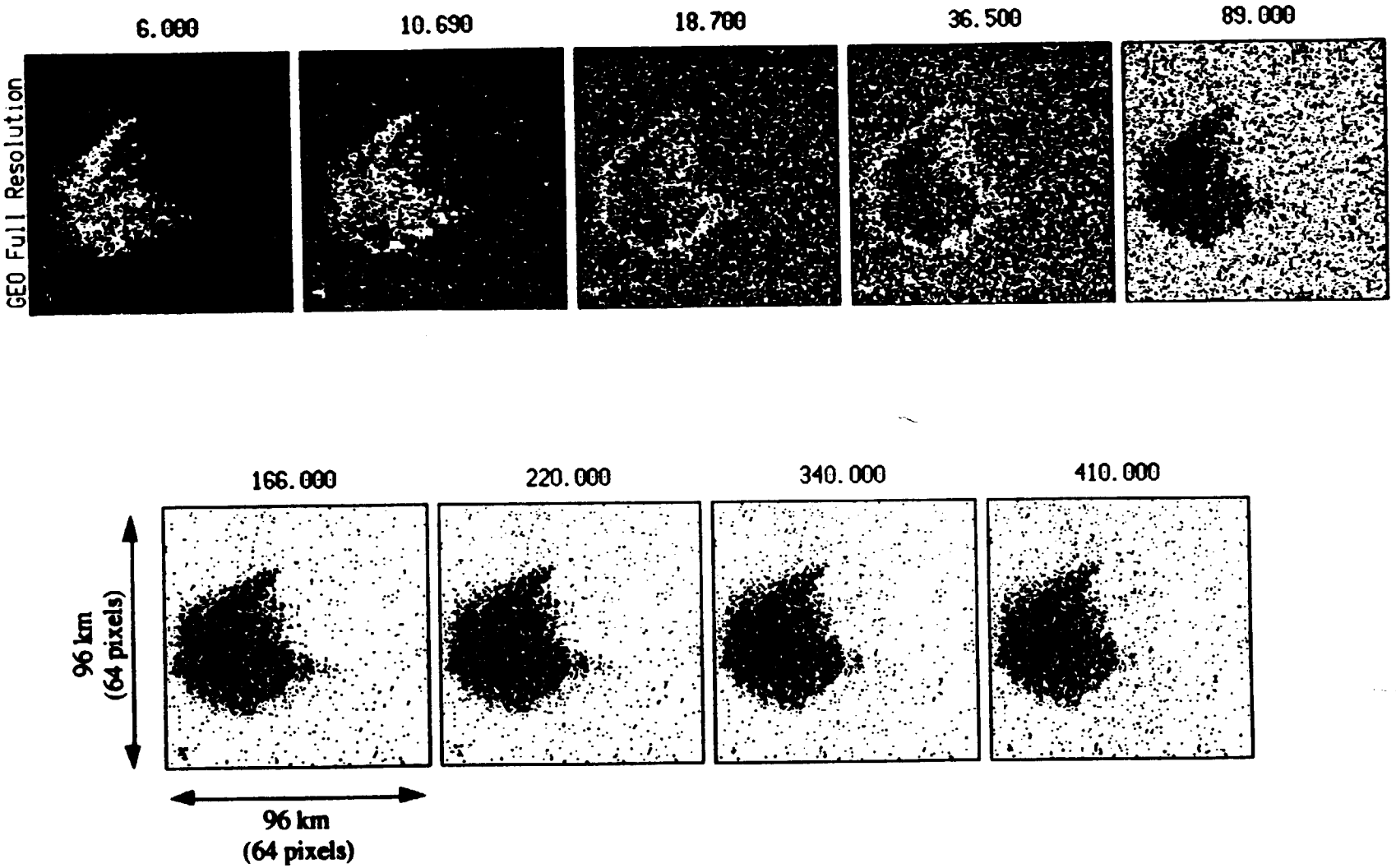

Figure 8 (a)

Figure 8: Representative LSA brightness temperature imagery for nine window channels, as would be observed from geosynchronous orbit: (a) full resolution, and (b,c) after convolution with the gain patterns of circular 40-m and 15-m quadratically-tapered aperture field distributions, respectively. The 3-dB spot sizes (in km, FWHM) are indicated for each frequency in (b) and (c).

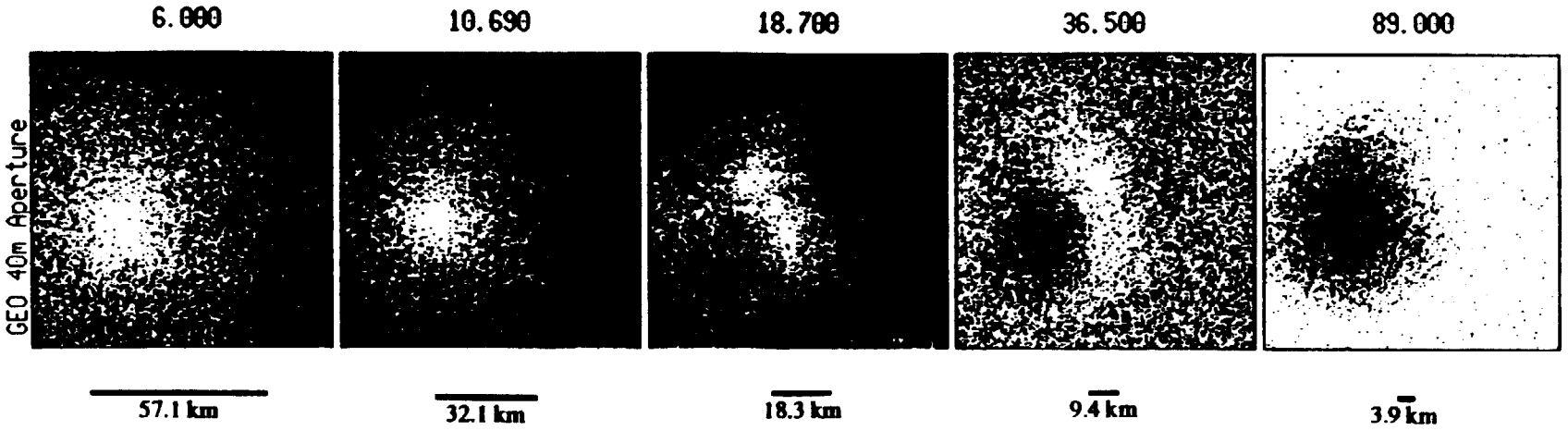
6.000
10.690
18.700
36.500
89.000
GEO 40m Aperture
57.1 km
32.1 km
18.3 km
9.4 km
3.9 km

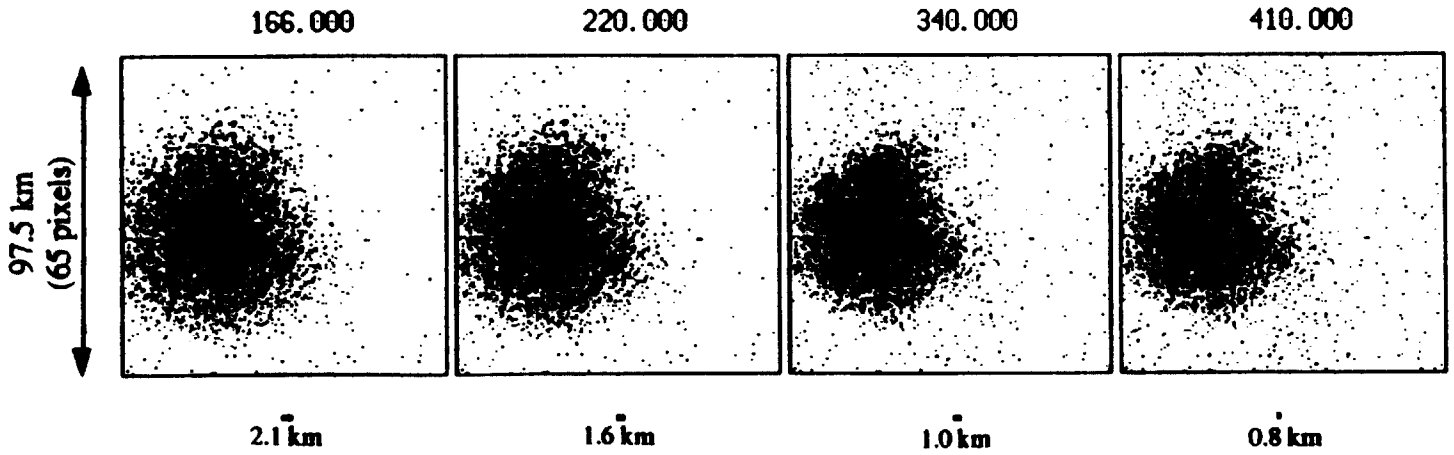
166.000
220.000
340.000
410.000
97.5 km
(65 pixels)
2.1 km
1.6 km
1.0 km
0.8 km

Figure 8 (b)

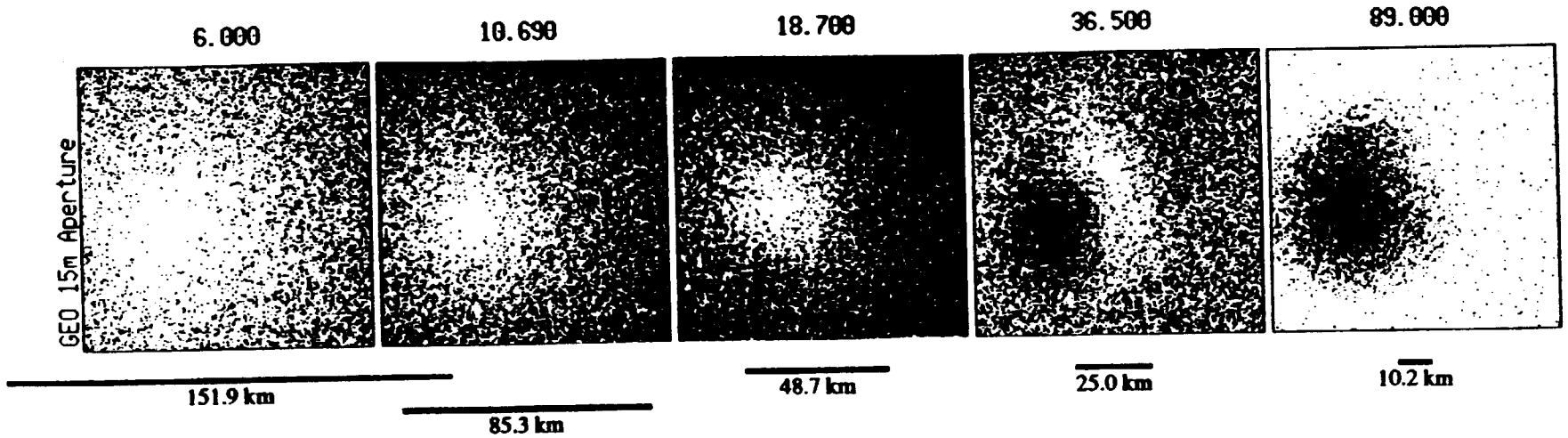
6.000
10.690
18.700
36.500
89.000
GEO 15m Aperture
151.9 km
85.3 km
48.7 km
25.0 km
10.2 km

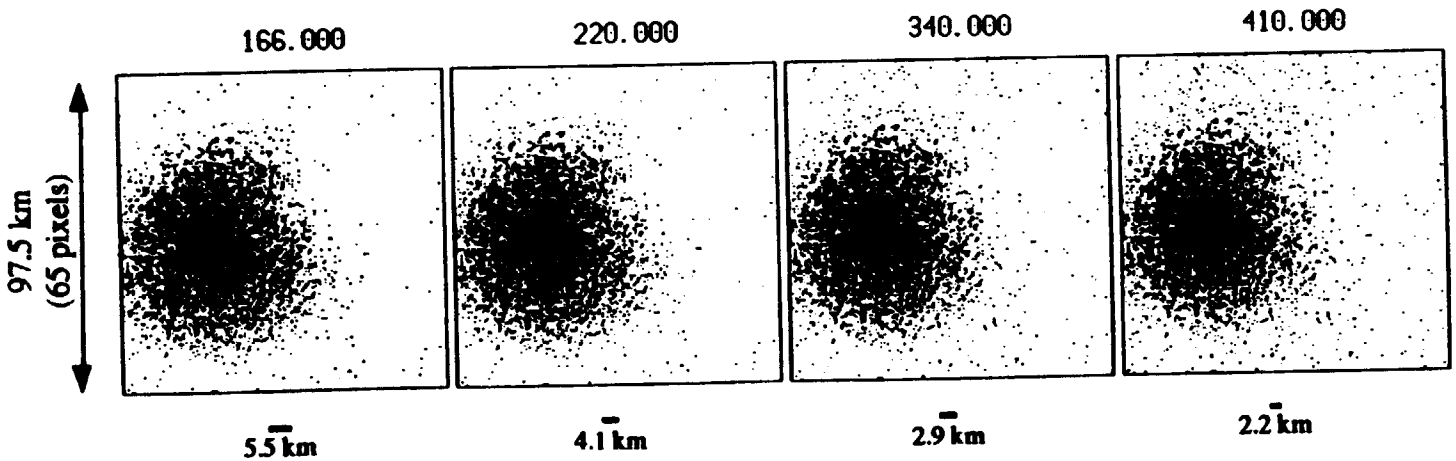
166.000
220.000
340.000
410.000
97.5 km
(65 pixels)
5.5 km
4.1 km
2.9 km
2.2 km

Figure 8 (c)

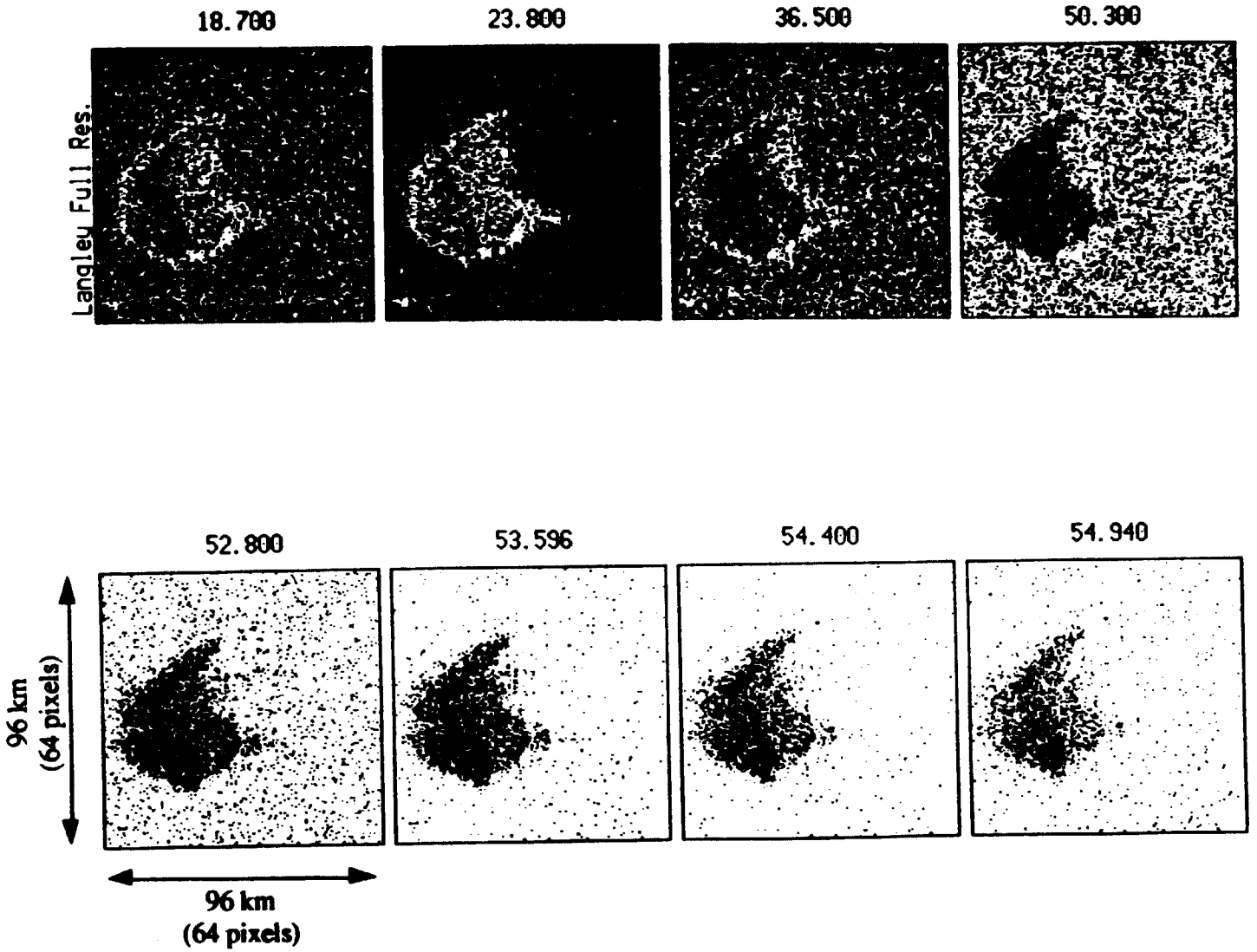

Figure 9 (a)

Figure 9: Representative LSA brightness temperature imagery for eight low-frequency channels, as would be observed from geosynchronous orbit: (a) full resolution, and (b,c) after convolution with the gain patterns of circular 40-m and 15-m quadratically-tapered aperture field distributions, respectively. The 3-dB spot sizes (in km, FWHM) are indicated for each frequency in (b) and (c).

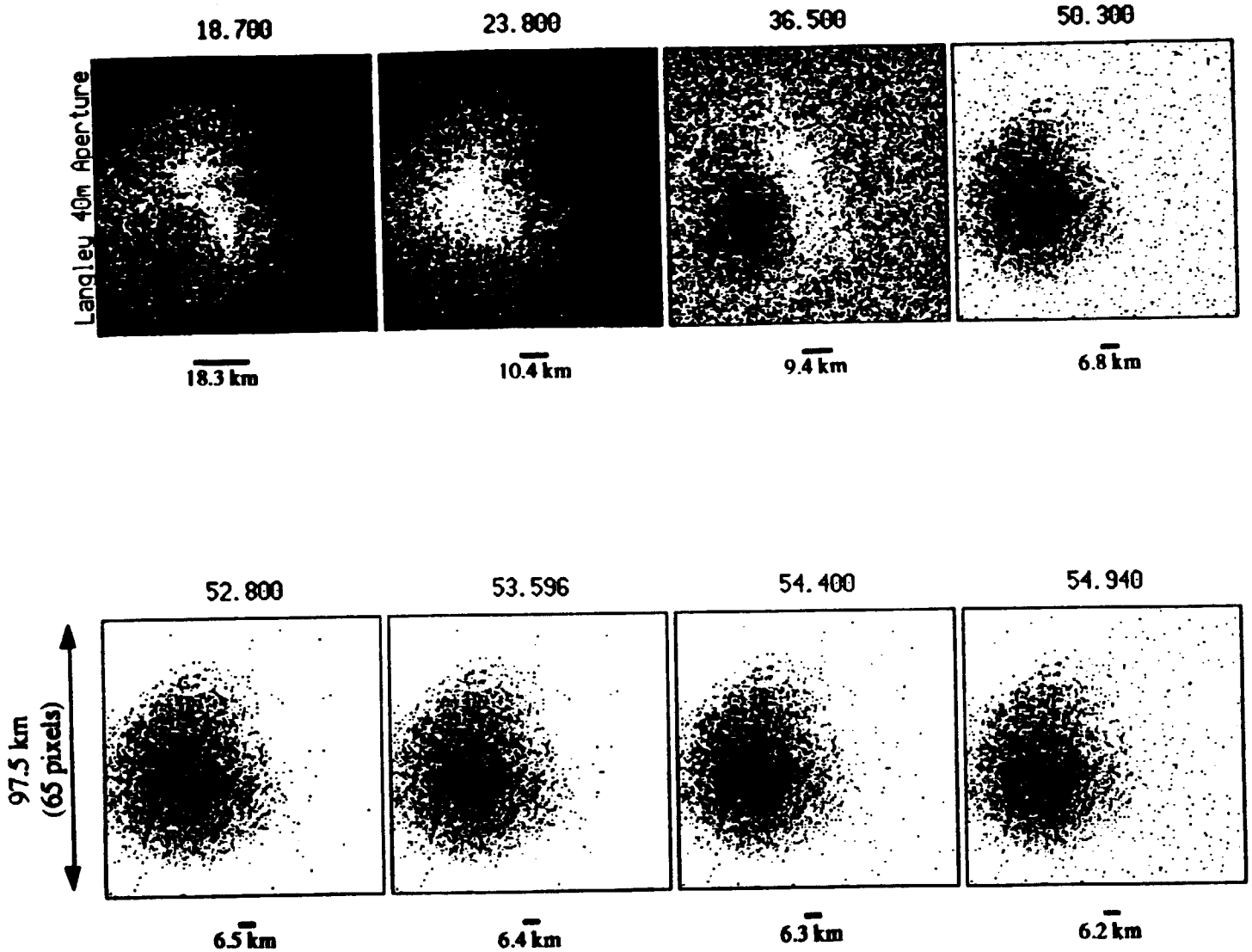
18.700
23.800
36.500
50.300
Langley 40m Aperture
18.3 km
10.4 km
9.4 km
6.8 km
52.800
53.596
54.400
54.940
97.5 km
(65 pixels)
6.5 km
6.4 km
6.3 km
6.2 km

Figure 9 (b)

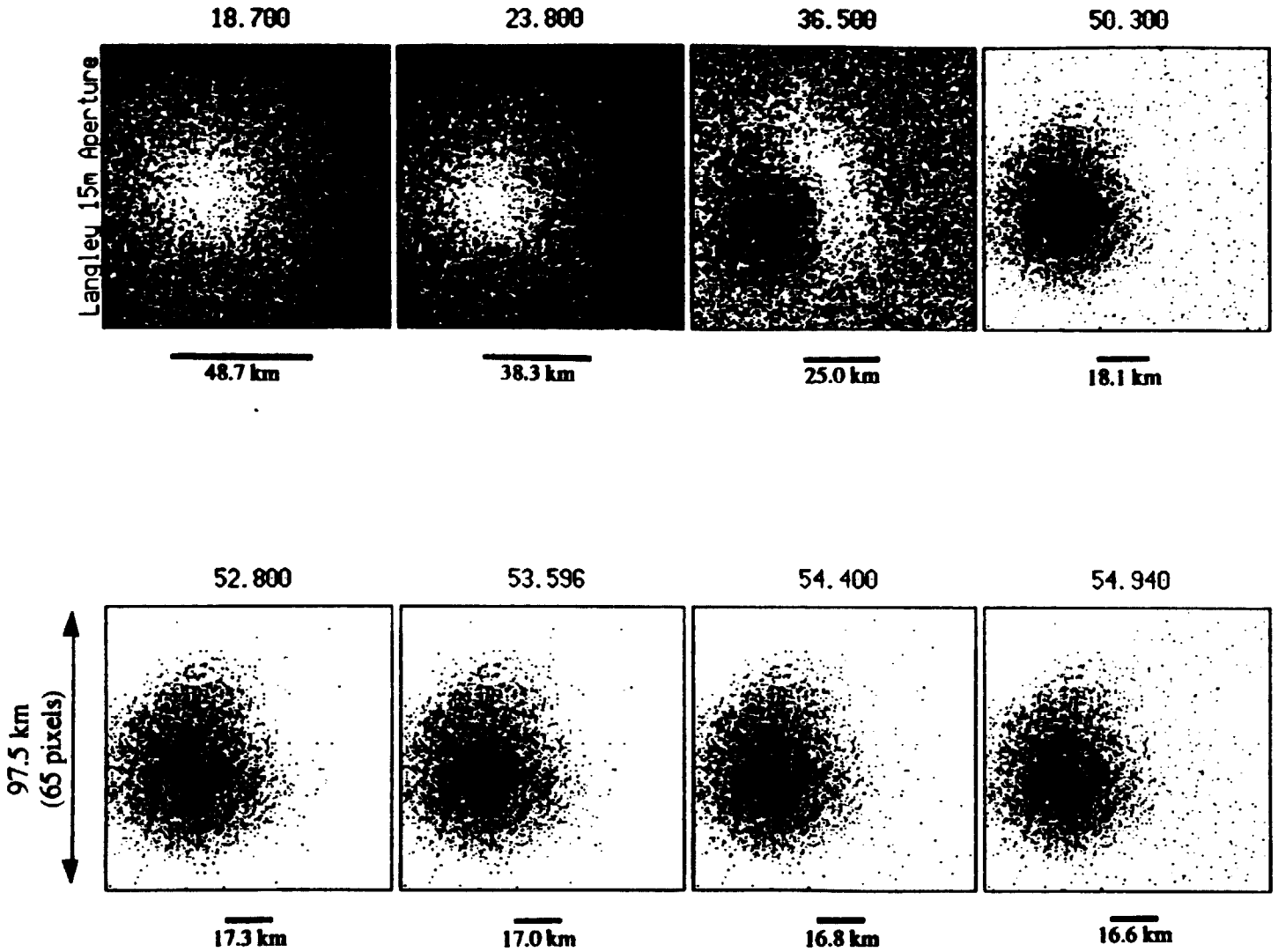
18.700
23.800
36.500
50.300
Langley 15m Aperture
48.7 km
38.3 km
25.0 km
18.1 km
52.800
53.596
54.400
54.940
97.5 km
(65 pixels)
17.3 km
17.0 km
16.8 km
16.6 km

Figure 9 (c)

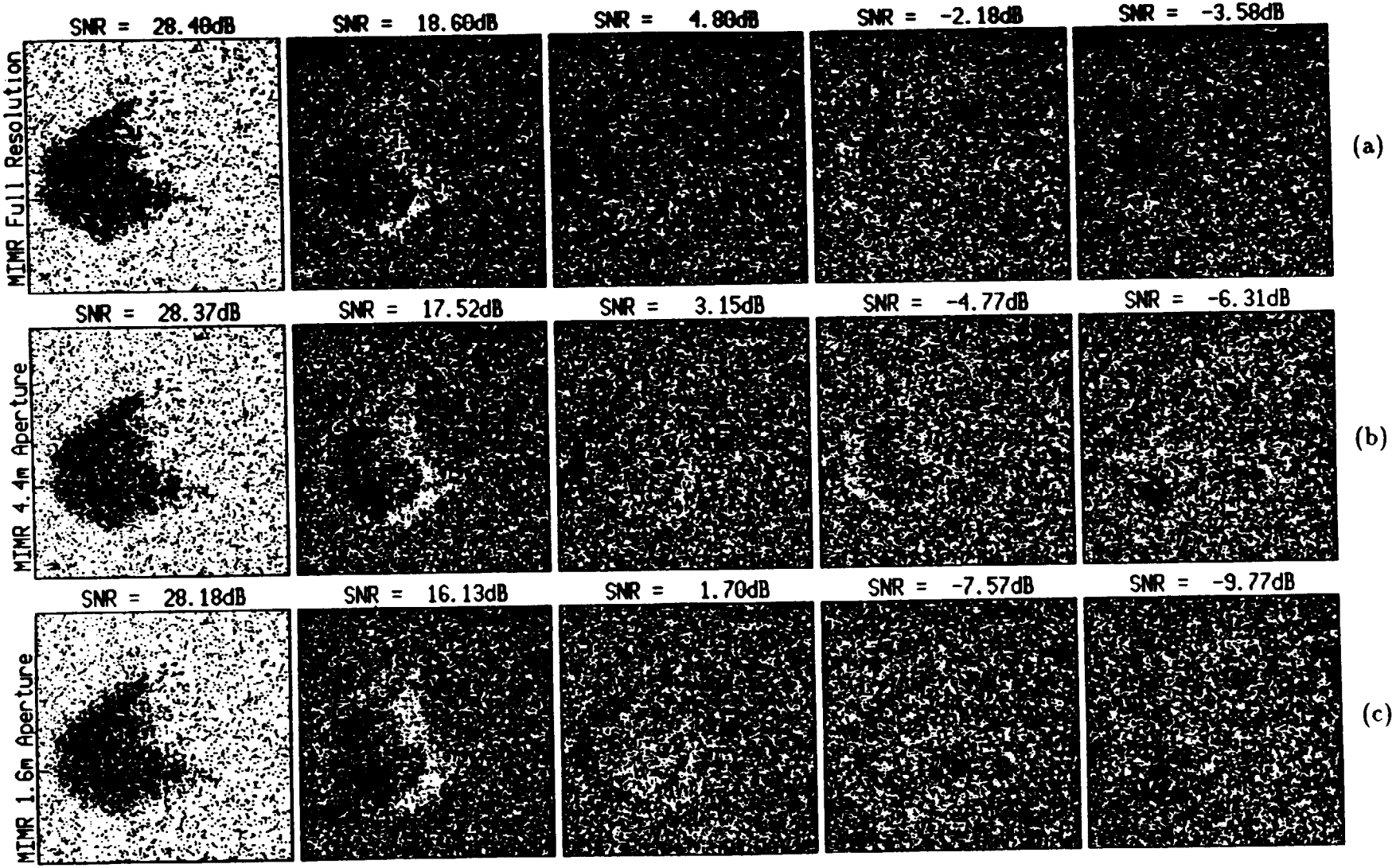

Figure 10: Rank-ordered KL mode imagery for the six-channel MIMR system: (a) full resolution, (b,c) after convolution with the gain pattern of a circular 4.4-m and 1.6-m quadratically-tapered aperture distribution, respectively. The five most dominant modes are shown with the respective SNR's indicated above each image.

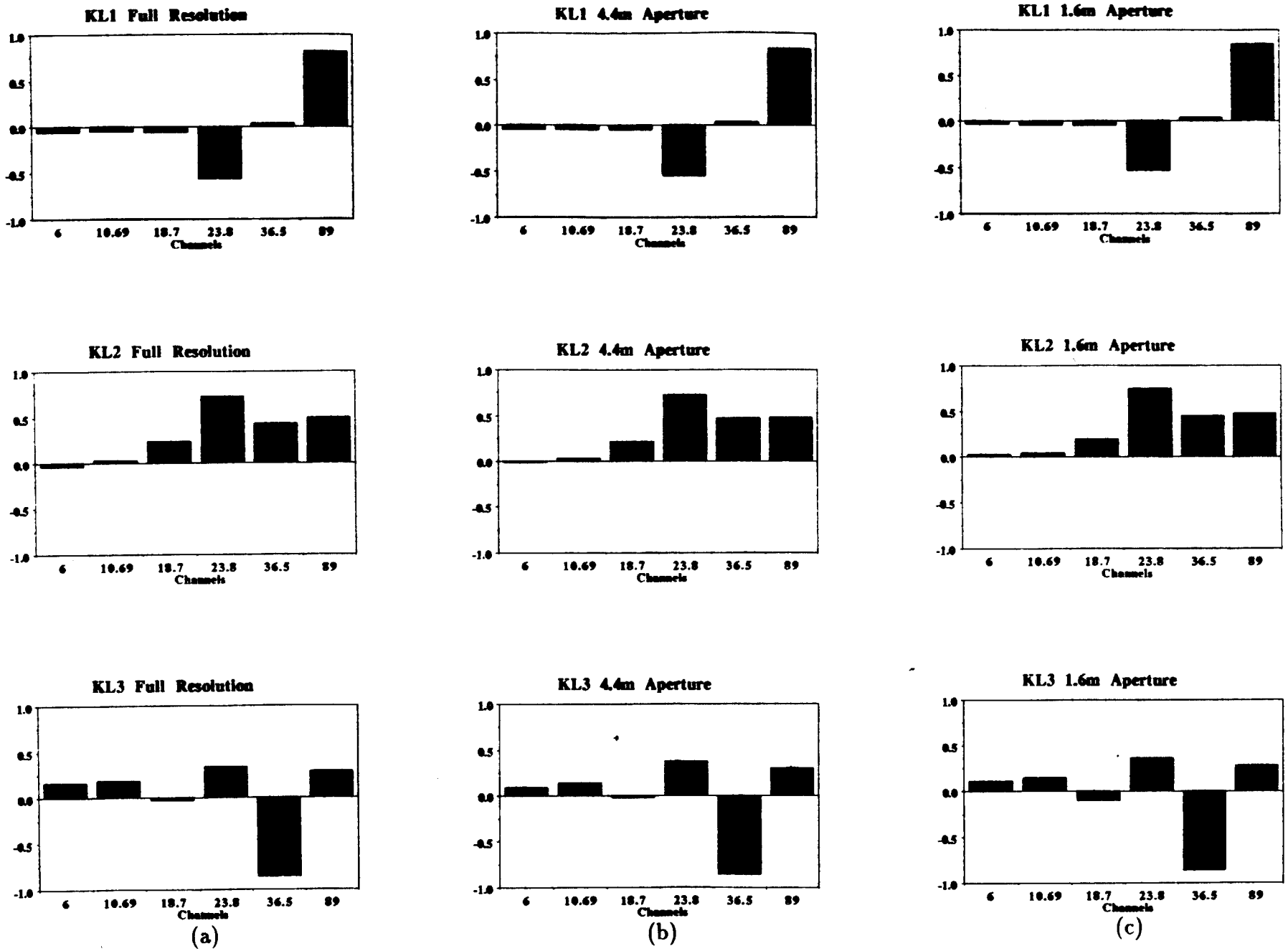

Figure 11: Three most dominant rank-ordered eigenvectors for the six-channel MIMR system: (a) full resolution, (b,c) after convolution with the gain pattern of a circular 4.4-m and 1.6-m quadratically-tapered aperture distribution, respectively.

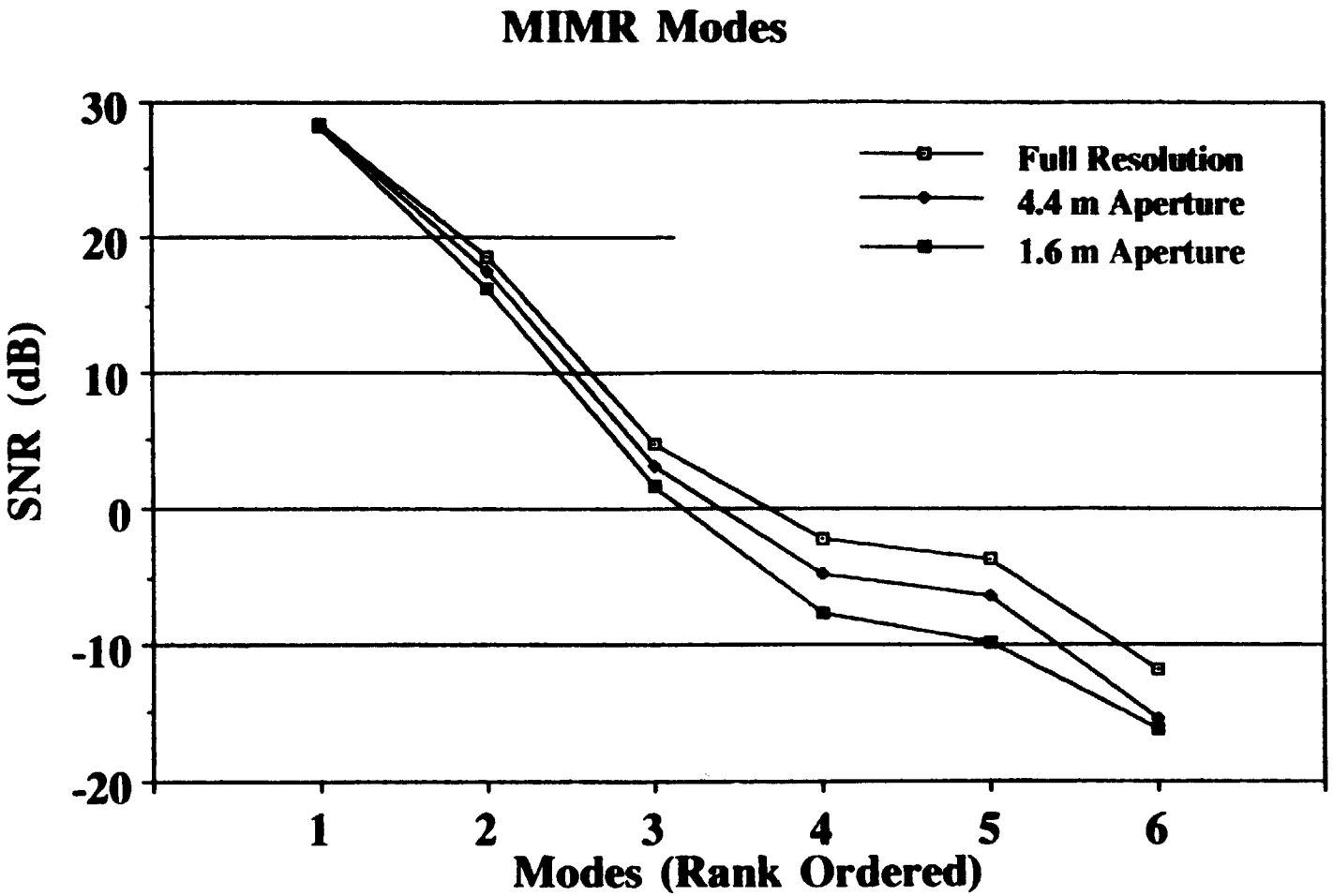

Figure 12: SNR ranking for the full-resolution and convolved MIMR imagery.

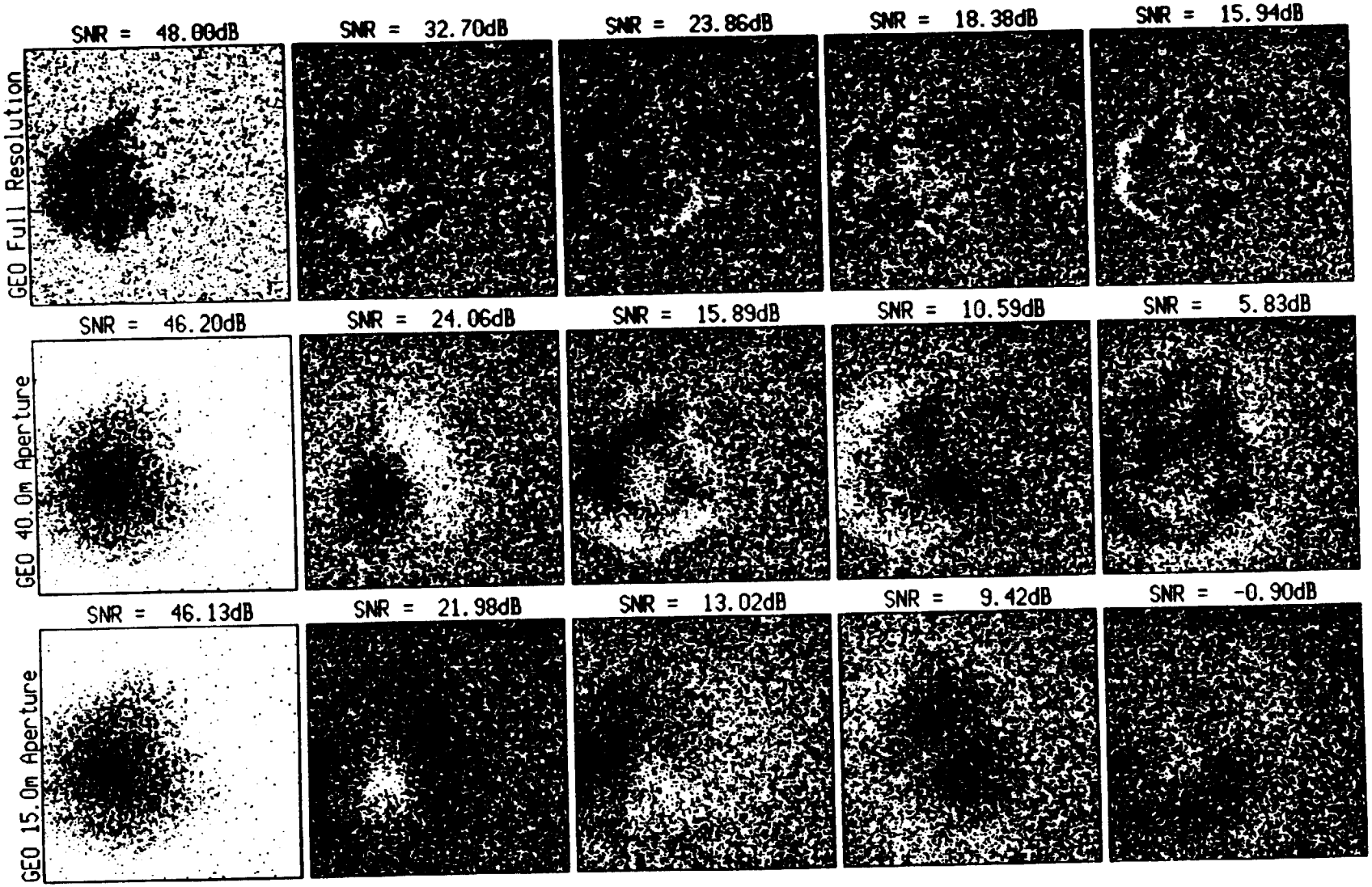

Figure 13: Rank-ordered KL mode imagery for the LSA nine-channel GEO system: (a) full resolution, (b,c) after convolution with the gain pattern of a circular 40-m and 15-m quadratically-tapered aperture distribution, respectively. The five most dominant modes are shown with the respective SNR's indicated above each image.

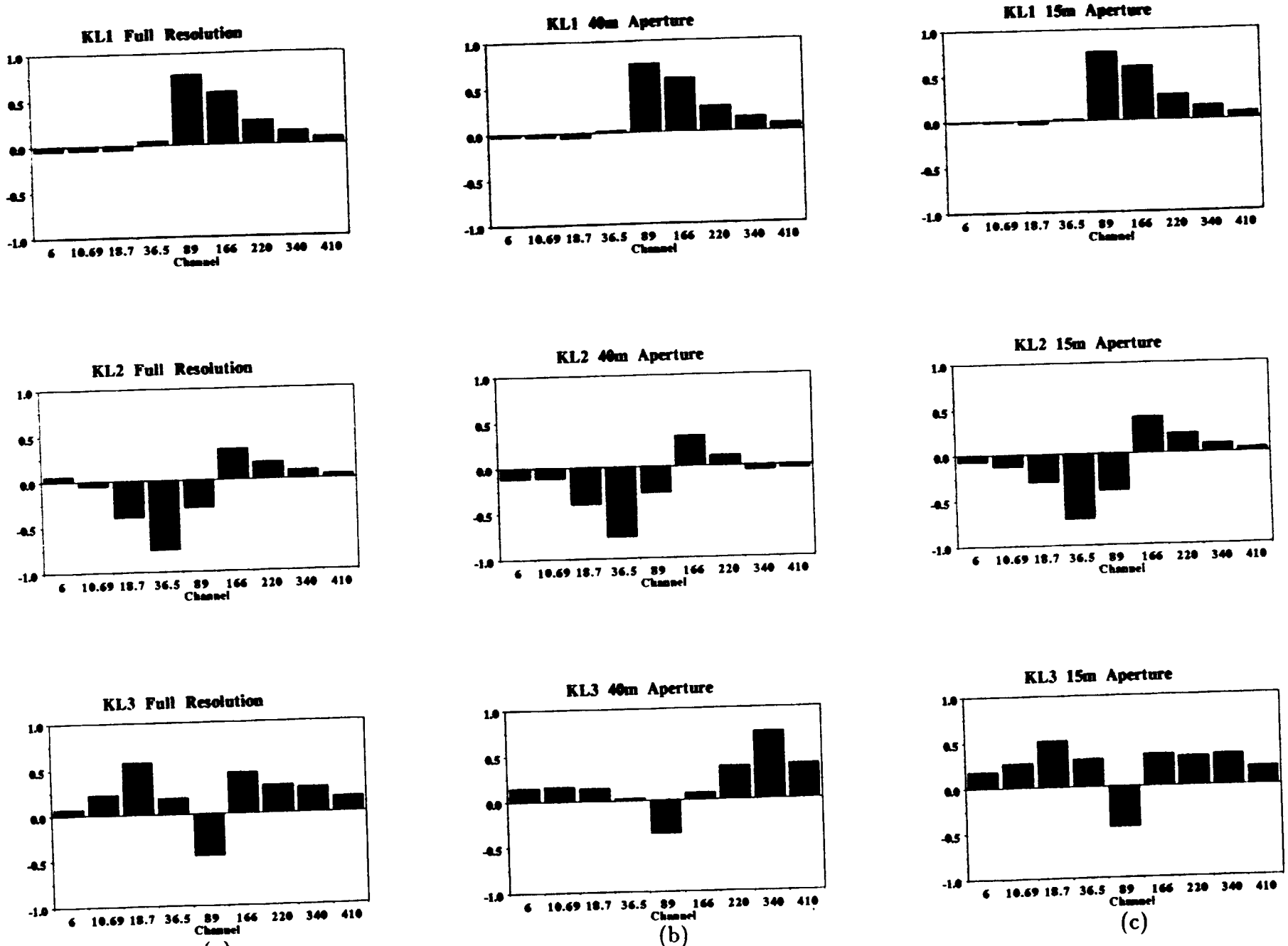

Figure 14: Three most dominant rank-ordered eigenvectors for the nine-channel LSA system: (a) full resolution, (b,c) after convolution with the gain pattern of a circular 40-m and 15-m quadratically-tapered aperture distribution, respectively.

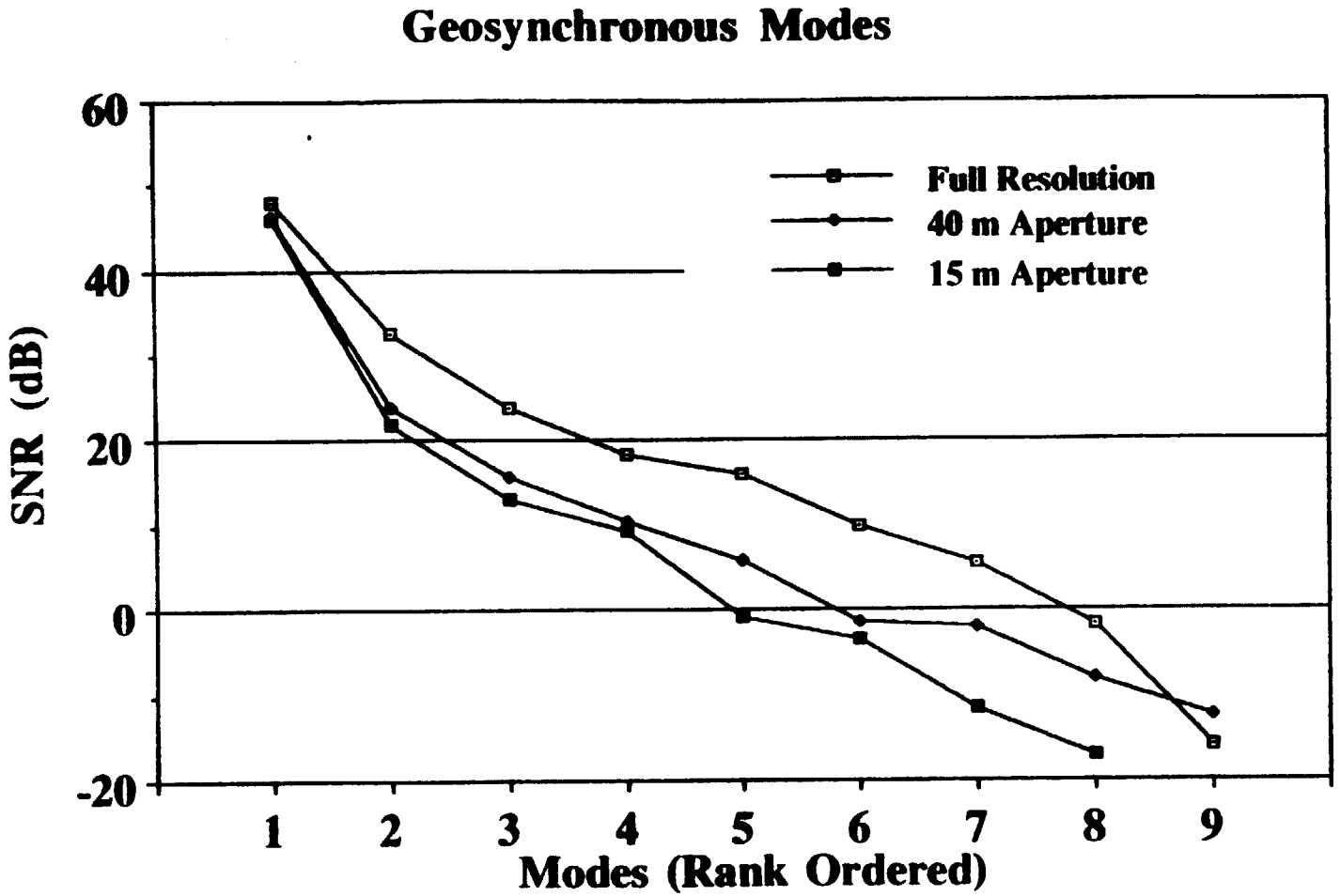

Figure 15: SNR ranking for the full-resolution and convolved nine-channel LSA imagery.

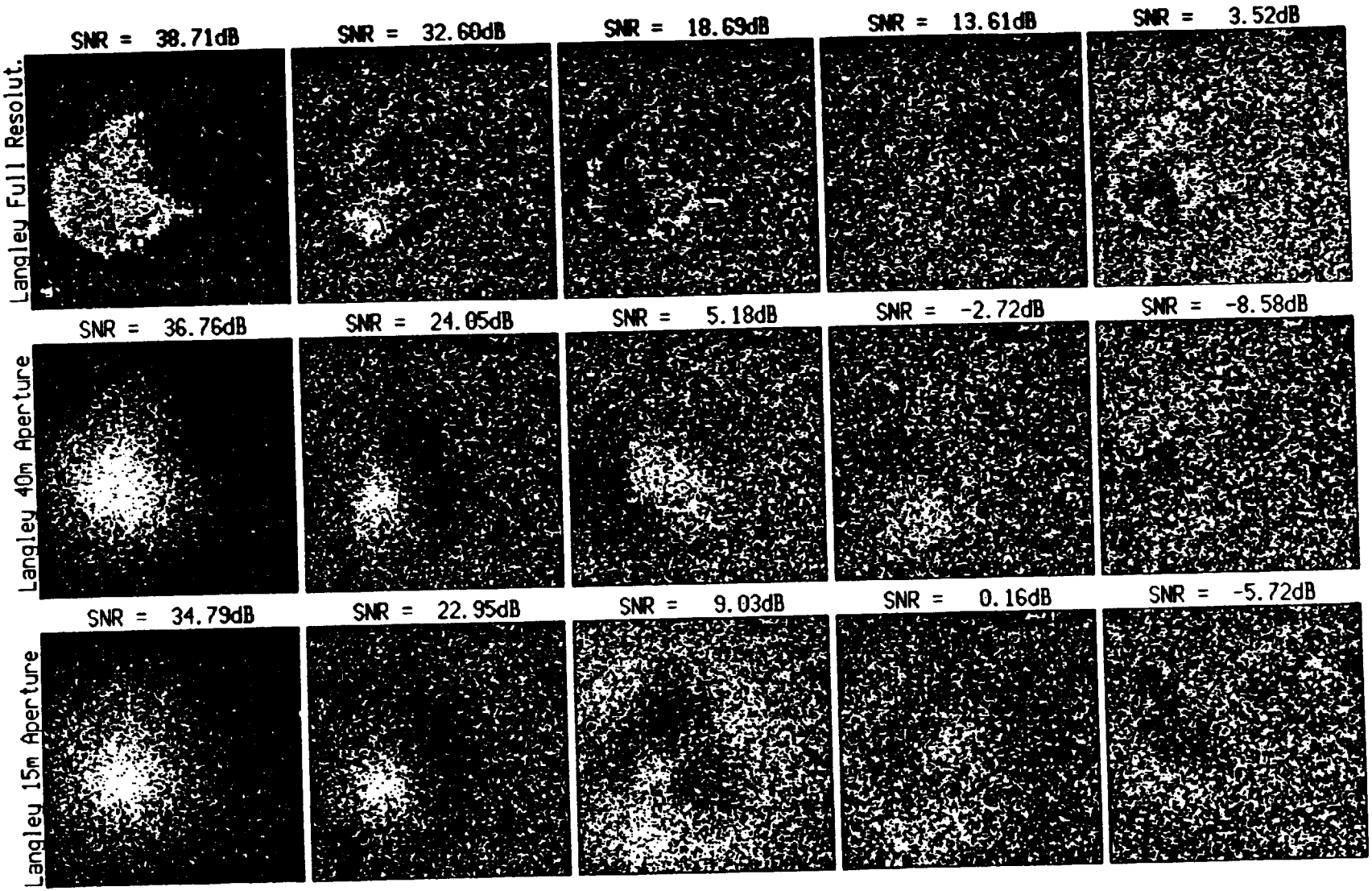

Figure 16: Rank-ordered KL mode imagery for the LSA eight-channel GEO system: (a) full resolution, (b,c) after convolution with the gain pattern of a circular 40-m and 15-m quadratically-tapered aperture distribution, respectively. The five most dominant modes are shown with the respective SNR's indicated above each image.

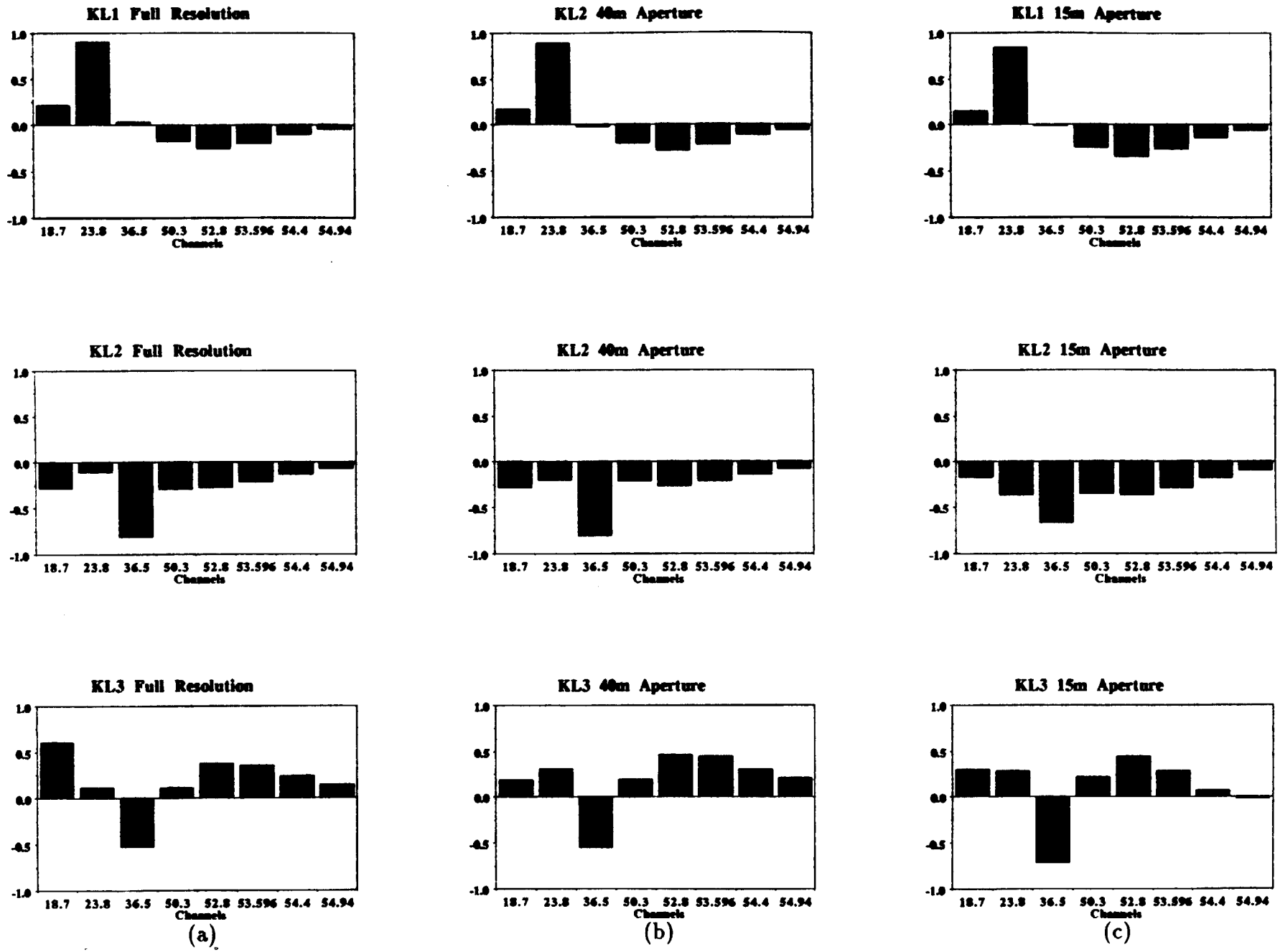

Figure 17: Three most dominant rank-ordered eigenvectors for the eight-channel LSA system: (a) full resolution, (b,c) after convolution with the gain pattern of a circular 40-m and 15-m quadratically-tapered aperture distribution, respectively.

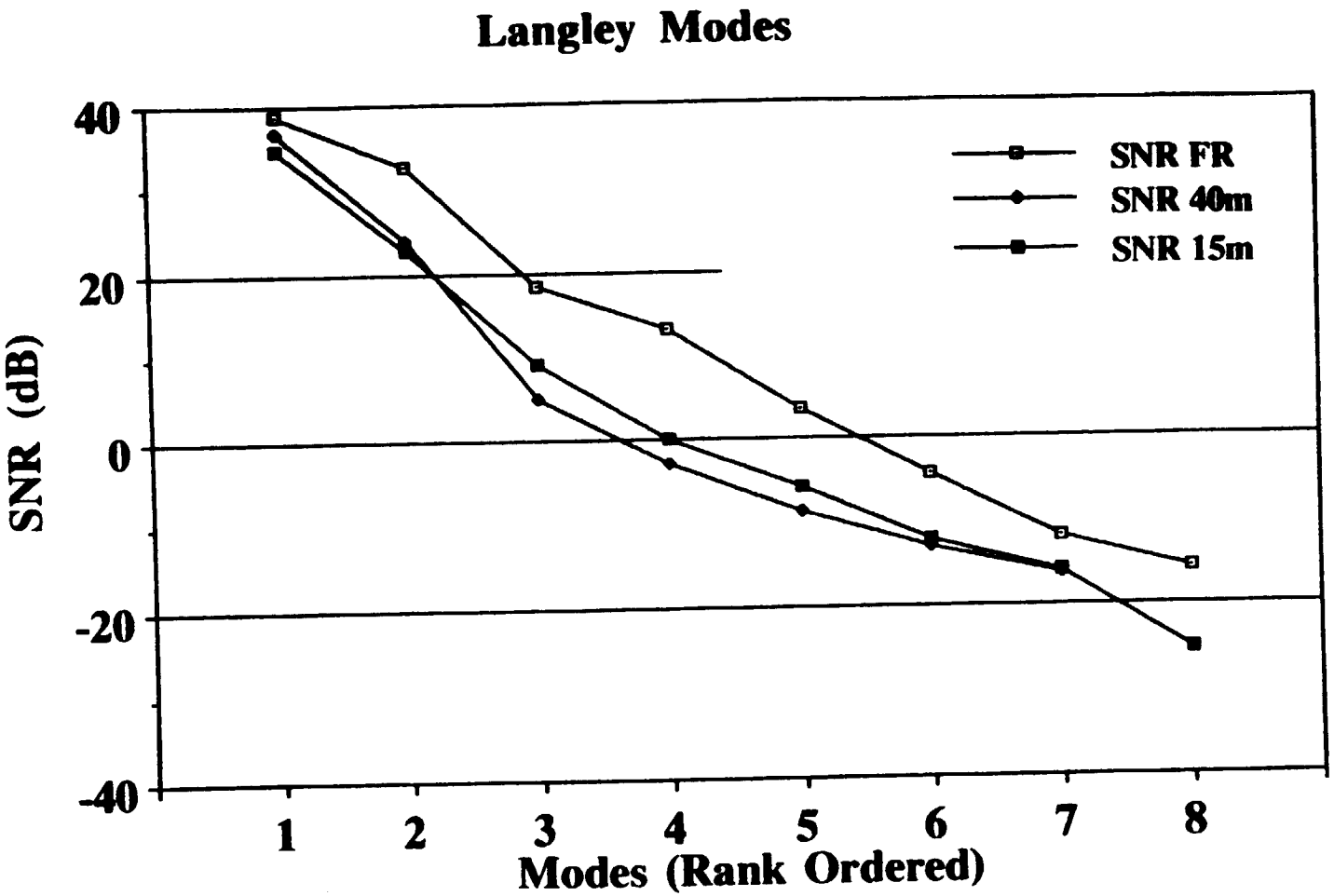

Figure 18: SNR ranking for the full-resolution and convolved eight-channel LSA imagery.

REPORT DOCUMENTATION PAGE

Form Approved
OMB No. 0704-0188

1. AGENCY USE ONLY (Leave blank)	2. REPORT DATE	3. REPORT TYPE AND DATES COVERED
	December 1992	Contractor Report

4. TITLE AND SUBTITLE
Investigation of Antenna Pattern Constraints for Passive Geosynchronous Microwave Imaging Radiometers

5. FUNDING NUMBERS
C NAS1-18925
WU 506-49-64-01

6. AUTHOR(S)
A. J. Gasiewski and G. M. Skofronick

7. PERFORMING ORGANIZATION NAME(S) AND ADDRESS(ES)
Research Triangle Institute (Subcontractor)
Post Office Box 12194
Research Triangle Park
NC 27709-2194

Georgia Institute of Technology
School of Electrical Engrg.
Atlanta, GA 30332-0250

8. PERFORMING ORGANIZATION REPORT NUMBER
RTI/4500/017-02F

9. SPONSORING/MONITORING AGENCY NAME(S) AND ADDRESS(ES)
National Aeronautics and Space Administration
Langley Research Center
Hampton, VA 23681-0001

10. SPONSORING/MONITORING AGENCY REPORT NUMBER
NASA CR-189728

11. SUPPLEMENTARY NOTES
Langley Technical Monitor: L. C. Schroeder
Final Report - Task 17
Gasiewski and Skofronick: Georgia Institute of Technology, Atlanta, GA

12a. DISTRIBUTION/AVAILABILITY STATEMENT
Unclassified - Unlimited

Subject Category 43

12b. DISTRIBUTION CODE

13. ABSTRACT *(Maximum 200 words)*

Progress by investigators at Georgia Tech in defining the requirements for large space antennas for passive microwave Earth imaging systems is reviewed. In order to determine antenna constraints (e.g., the aperture size, illumination taper, gain uncertainty limits) necessary for the retrieval of geophysical parameters (e.g., rain rate) with adequate spatial resolution and accuracy, a numerical simulation of the passive microwave observation and retrieval process is being developed. Due to the small spatial scale of precipitation and the nonlinear relationships between precipitation parameters (e.g., rain rate, water density profile) and observed brightness temperatures, the retrieval of precipitation parameters are of primary interest in the simulation studies. Major components of the simulation are described as well as progress and plans for completion. The overall goal of providing quantitative assessments of the accuracy of candidate geosynchronous and low-Earth orbiting imaging systems will continue under a separate grant.

14. SUBJECT TERMS	15. NUMBER OF PAGES
large space antenna, microwave radiometry, precipitation retrieval, resolution	75
	16. PRICE CODE: A04

17. SECURITY CLASSIFICATION OF REPORT	18. SECURITY CLASSIFICATION OF THIS PAGE	19. SECURITY CLASSIFICATION OF ABSTRACT	20. LIMITATION OF ABSTRACT
unlcassified	unclassified		